Kinematics and Chemical Properties of the Old Disk

by James Robert Lewis

A thesis submitted for the degree of Doctor of Philosophy
of the Australian National University

October, 1986

Mt Stromlo and Siding Spring Observatories
Australian National University
Canberra

The work described in this thesis is that of the candidate alone, except where acknowledged otherwise in the text.

James R. Lewis

To my family and Carolien

with love.

Acknowledgements

First and foremost I wish to thank Dr. K.C. Freeman for being the best supervisor I could have possibly asked for. Over the past four years his advice, encouragement, infectious enthusiasm and friendship have been crucial to me not only on the professional but also on the personal level. I must admit that there were times when I was overwhelmed by the total amount of work which lay before me. But Ken never gave up on me and was always able to help keep things in perspective. For this he has my most heartfelt gratitude.

Over the course of my studies I have received valuable advice from many other of the staff and students at Mount Stromlo and other institutions. I benefitted greatly from many discussions with Drs. John Norris, Mike Bessell, Agris Kalnajs, Nigel Sharp, Professor Alex Rodgers, Heather Morrison, Gregg Rowley, Andrew Kulessa, and Chris Flynn. Greg Wilson kindly let me use some of his results in advance of publication. Gregg Rowley, Chris Flynn and Greg Wilson all deserve my thanks for helping with some of the observations that are presented in this thesis. Kavan Ratnatunga led me by the hand through the wild and wonderful world of photographic photometry. A special thank you goes to Professor Don Mathewson for initially providing me with the impetus to return to Mount Stromlo as a student and for magically coming up with the travel funds I needed for the Kitt Peak observing run. Another special mention must go to Dr. Phil Ianna of the University of Virginia. It is thanks to his southern trigonometric parallax program that I was first sent to Mount Stromlo where I have now spent nearly five happy years. Finally a special mention goes to the memory of Dr. V. Osvalds of the University of Virginia, whose friendship, enthusiasm and courage during my undergraduate days has never failed to provide me with inspiration when I have needed it.

On a somewhat different note, I wish to thank the entire Canberra musical community, in particular Mr. Leonard Dommett and Mrs Maeva Galloway of the Canberra Symphony Orchestra and Mr. Richard McIntyre of the Canberra Youth Orchestra for providing me with an interesting and rewarding diversion when it was sorely needed. A mention also goes to Gabi Robin for being a conscientious student and to her family for being so kind and friendly during the three years I have known them. Finally a special word of thanks goes to Philippa Pang, Melissa Macourt, Liz Freeman, Netty Merrillees and Eva Schroeder, my fellow violists in the Canberra Youth Orchestra, for always greeting me with a smile at those early Saturday morning rehearsals.

In a similar vein I wish I could personally thank Sir Georg Solti and all the instrumentalists, vocalists and engineers who participated in his recording of the Symphony #8 by Gustav Mahler, to which I listened incessantly during the course of writing up this thesis and which has never failed to inspire and astonish.

The time allocation committees at Mount Stromlo, the Anglo-Australian Observatory and National Optical Astronomy Observatories deserve a word of thanks for the generous amounts of observing time allocated for this project. I particular I wish to thank all of the innumerable night assistants for putting up with what must have seemed like incessant requests and for gently waking me up when fatigue finally got the best of me.

Finally I wish to apologize to all those whom I haven't explicitly mentioned here; it is not that your help was not appreciated, but rather that my memory is somewhat porous. To everyone at Mount Stromlo and Siding Spring Observatories, in particular all of the students, both past and present, I want to say thank you for the level of friendship, comradery and the strong sense of community I have felt here at Mount Stromlo and which has helped to make my stay in Australia a very happy one.

Financial assistance was provided for this work in the form of an Australian National University Scholarship for which I am naturally very grateful.

Abstract

We have observed about 600 old disk K giants with both broadband photometry and medium resolution spectroscopy. These giants are located in strategically chosen galactic low absorption windows in the plane of the disk. The spectroscopic observations gave accurate radial velocities, and together with the photometric observations gave an estimate of each star's chemical abundance and photometric parallax. As a result we have measured the radial variation of $\langle V_R \rangle$, $\langle V_\varphi \rangle$, σ_R, σ_φ (the mean motions and velocity dispersions in the plane of the old disk), as well as the radial variation of $[Fe/H]$, over a long baseline in galactocentric radius.

The observed exponential decrease with radius of the radial component of the velocity dispersion gives an estimate of the disk's radial scale-length which is consistent with other recent structural determinations. This agreement between the structural and kinematic scale-lengths indicates that the velocity dispersion of the old disk is uniformly anisotropic in the R, z plane, throughout. The inner parts of the old disk of the Milky Way are quite hot ($\sigma_R \approx 100$ km sec^{-1}). This is important, as it may be these random motions which stabilize the disk against global bi-symmetric modes. Possible mechanisms to produce these large random motions are discussed.

The run of the tangential component of velocity dispersion gives another kinematic scale-length. The fact that the radial and tangential kinematic scale-lengths are not equal indicates that the rotation curve is not flat over the entire galaxy. A rough calculation of the rotation curve from these measured runs of velocity dispersion is in good agreement with the CO rotation curve.

Finally, the radial metallicity gradient seen in young and intermediate age objects does not appear in the old disk. This may indicate that star formation has progressed radially outward from the galactic center, with the star formation rate and metallicity depending on the local gas fraction.

Table of Contents

Tables

Figures

Knut Lundmark's map of the Milky Way. The circles on the overlay mark the approximate location of the regions observed in this thesis. Note that the coordinates are on the old system.

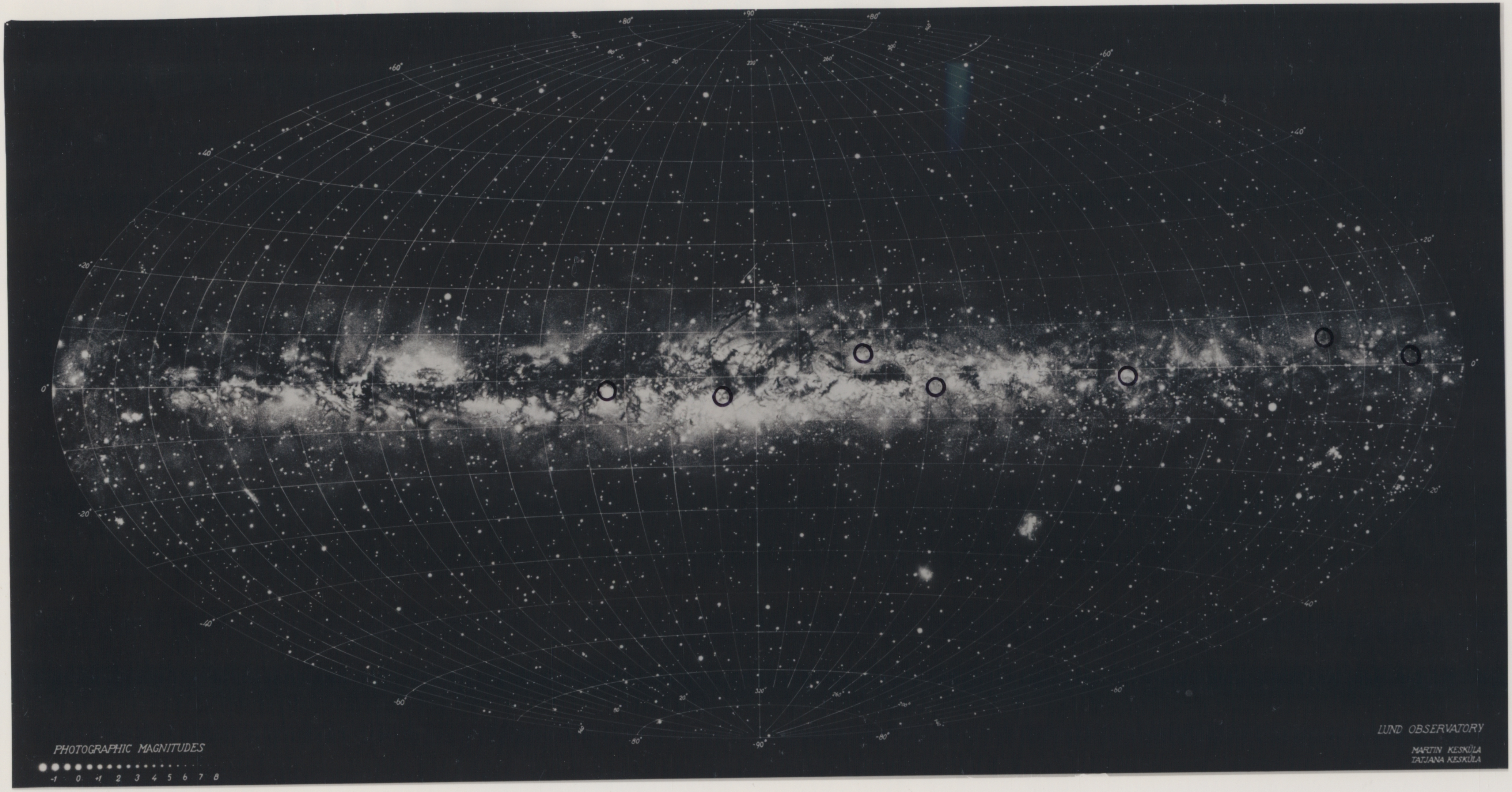
PHOTOGRAPHIC MAGNITUDES
-1 0 +1 2 3 4 5 6 7 8
LUND OBSERVATORY
MARTIN KESKÜLA
TATJANA KESKÜLA

CHAPTER ONE

Introduction

Late type spiral galaxies like the Milky Way have two major components, a disk and a bulge. The Milky Way also has some interesting minor components, which include the metal weak nonrotating halo and probably an intermediate metallicity 'thick disk.' Disk stars make up most of a sample of stars in the solar neighborhood. The oldest of these stars have a total velocity dispersion in the plane of about 50 km sec^{-1} and about 20 km sec^{-1} perpendicular to the plane (Woolley 1965). These dispersions are small compared to the circular velocity at the sun, 220 km sec^{-1}, which indicates that locally the disk is cold and rotationally supported. Quite the opposite is true of the bulge and halo populations near the sun. These stars make up between 0.2 to 0.5 of one percent of the stars in the solar neighborhood (Bahcall & Soneira 1980, 1984): their velocity dispersion is about 120 km sec^{-1} and their rotation is low, so this population is pressure supported.

The existence of a third component, the 'thick disk' is currently the subject of some controversy. Estimated local normalizations range from 0.5% to 10.0% of the local density of disk stars (see for example Sandage 1986, Gilmore & Reid 1983). Although the kinematics of the thick disk are not yet well understood, it appears to be approximately in rotational equilibrium with an asymmetric drift of 30 to 40 km sec^{-1} near the sun (Ratnatunga & Freeman 1985). In the vertical direction, the scale-height of the thick disk is between 1 and 1.5 kpc, compared to the old disk scale-height of 325 pc (Gilmore & Reid 1983).

In this thesis we will study the kinematics and chemical properties of the old disk of the Milky Way. As the Milky Way is probably a fairly normal Sb to Sc galaxy, our results should hold more generally, for other similar disk galaxies.

1.1 Structure of Galactic Disks

One of the primary results of galactic studies has been the discovery of the light distributions in the radial and vertical directions in galactic disks. De Vaucouleurs (1959) and Freeman (1970) noted that almost every disk galaxy for which photometry had been obtained showed a radial decline in surface brightness which was exponential with galactocentric distance R, i.e.

$$\mu(R) = \mu_o e^{-R/h} \tag{1.1}$$

where h is the disk's radial scale-length. If the mass-to-light ratio is constant over the entire disk, then the mass surface density follows the same exponential decline.

The origin of the exponential distribution is not yet understood. The exponential disk has a fairly well defined internal angular momentum distribution, so whatever process leads to the exponential disk presumably involves redistribution of angular momentum. Lynden-Bell & Kalnajs (1972) suggested that non-axisymmetric perturbations could cause redistribution of mass and angular momentum. They pointed out that, in a galaxy in a quasi-steady state which obeys the viral theorem, the total kinetic energy is fixed and hence any increase in the random motions must signal a decrease in the rotational kinetic energy. An outward flow of mass would accomplish this as the length scale of the system would increase but the angular momentum would remain constant, and therefore the rotational kinetic energy would decrease. However it is also necessary to conserve potential energy.

A more centrally concentrated inner mass would accomplish this balance. They showed that non-axisymmetric perturbations were capable of causing this angular momentum transfer.

Hohl's (1971) N-body experiments showed that locally marginally stable disks in equilibrium were globally unstable to non-axisymmetric modes. These bars caused the remaining axisymmetric disk to heat up. He found that his final surface density distribution could be fitted by the sum of two exponentials, the outer exponential representing the axisymmetric distribution and the inner exponential component being the bar.

Carlberg & Sellwood (1985) suggested that this redistribution of angular momentum could be caused by spiral density waves. They gave an estimate for the expected change in angular momentum in the solar neighborhood, but stopped short of giving a full description of the evolution of the surface density of the entire disk.

In the vertical direction, Spitzer (1942) and Camm (1950) found that, for highly flattened spheroidal systems which were self-gravitating and locally isothermal, the vertical density distribution function behaved like:

$$\rho = \rho_o \mathrm{sech}^2\left(\frac{z}{z_o}\right) \tag{1.2}$$

This function tends to an exponential for $z/z_o >> 1$. Tsikoudi (1977) did deep surface photometry of three edge-on S0 galaxies and found that, far from the plane, the vertical light distribution decreased exponentially. This led Freeman (1978) to suggest that disks could be represented as an isothermal sheet. Van der Kruit and Searle (1981) then fitted isothermal disk models to surface photometry of a number of edge-on galaxies. They not only found that the sech^2 solution fitted the photometry well, but also that the scale-height, z_o, was independent of radius, i.e. disks have a constant 'thickness'. This important result implies directly, from hydrostatic equilibrium, that the vertical velocity dispersion is described simply by the function:

$$\sigma_z^2 \propto e^{-R/h} \tag{1.3}$$

where h is again the disk's radial scale-length. Recently van der Kruit & Freeman (1984, 1986) have measured the run of vertical velocity dispersion in several face-on systems. Their results confirm the predictions of the radial decline of σ_z for a locally isothermal disk of constant thickness and mass-to-light ratio.

More recently, Wainscoat (1986) has done infrared photometry on a number of edge-on spiral galaxies. He has found that an exponential:

$$\rho = \rho_o e^{-z/z_o} \tag{1.4}$$

is a better fit to the data than the sech^2 solution associated with the locally isothermal sheet model. The only place that this really makes much of a difference, though, is near the galactic plane where $z/z_o < 1$. Pritchet (1983) also found, from star counts, that an exponential appears to fit the vertical structure of the Milky Way.

1.2 Equilibrium

Galactic disks are close to rotational equilibrium in the radial direction i.e.

$$\frac{V^2(R)}{R} = \frac{\partial \Phi}{\partial R} \tag{1.5}$$

where $V(R)$ is the rotational or circular velocity at radius R and Φ is the galactic potential. However, the old disk has some support from its velocity dispersion. Hence the mean rotational velocity is in fact less than that which is predicted from equation (1.5). The difference is known as the 'asymmetric drift'.

In the z direction, the disk is in equilibrium by the pressure gradient associated with random motions vertical to the plane balancing the gravitational field. It has long been known, however, that stars of different ages have different characteristic scale-heights and velocity dispersions. This prompted Spitzer & Schwarzschild (1951, 1953) to suggest that the vertical dispersion grows through many stellar encounters with cold dark clouds. This mechanism naturally produces a gradient of velocity dispersion with age. Whether this is enough to produce the observed age-velocity dispersion relation is still the subject of debate (Wielen 1974, Carlberg et al 1985, Lacey & Fall 1983).

1.3 Local Stability

The question of the local stability of a uniform cold disk was discussed by Toomre (1964). He found that unless a certain amount of random motions were present, the disk would be unstable to local axisymmetric disturbances. His famous parameter:

$$Q = \frac{\sigma_R \kappa}{3.36 G \Sigma} \tag{1.6}$$

where σ_R is the radial component of velocity dispersion, κ is the local epicyclic frequency, Σ is the surface density and G is the gravitational constant, must exceed 1 for a disk to be stable against these local instabilities. Measurements of σ_R in the solar neighborhood indicate that the disk of the Milky Way is locally stable. It would be interesting to confirm observationally that the entire disk is indeed hot enough to be stable against these axisymmetric modes, as one would expect.

1.4 Global Stability

The question of global stability of disks against bar modes should now be considered. Obviously not all galaxies are stabilized against these modes; at least 37% of bright spirals have bars in their disks. But at least another 30% have no hint of such a bar. In his paper on local stability, Toomre (1964) remarked that disks may preferentially develop global bar-like structures. These were in fact observed in numerical experiments by Miller et al (1970), Hohl (1971) and Ostriker & Peebles (1973) as well as many others. The theoretical studies of Kalnajs (1972), who solved the collisionless Boltzmann equation and Poisson's equation, and Hunter, who solved a system of stellar hydrodynamical equations for a rotating Maclaurin disk, have also pointed to these global bi-symmetric modes.

So the question remains as to what stabilizes those disks which do not have bars. Ostriker & Peebles (1973) introduced a parameter

$$t = T/|W| \tag{1.7}$$

where T is the rotational kinetic energy and W is the gravitational potential energy. They found that if $t \leq 0.14 \pm 0.02$ then the disk would be stable. In their N-body simulations they ran many different models, varying the velocity dispersion in the disk and adding varying amounts of unseen matter (a dark massive halo) to the models. They found that in those models for which the halo mass was less than about one disk mass, the disk went through a period of non-axisymmetric barlike structure which later dissolved back into roughly an axisymmetric disk once t had reached the critical value. What was left was a stable but very hot disk. The stability obviously comes about because the rotational kinetic energy has been transferred into kinetic energy of random motion.

The effect of placing a massive halo in the models is to reduce the initial value of t by increasing the gravitational potential $|W|$. This then stabilizes the disk without the large increase in random motions. Because several lines of evidence at the time were pointing towards massive dark coronae in disk galaxies, Ostriker & Peebles opted for stabilization by massive halos.

A study by Zang (1976) seems to have produced an example which violates the generality of the Ostriker & Peebles criterion. However in another study by Miller (1978), Zang's results could not be confirmed. Berman & Mark (1979) claimed to have found that a small bulge component can prevent bar formation in cool stellar disks. However, their results may be spurious due to the very large amount of gravity softening included in their models (Sellwood 1981).

Efstathiou et al (1982) have studied the effects of varying the mass of the dark halo and varying the turnover radius in the disk. They have concluded that, for a cold disk, the relation:

$$V_m\sqrt{\frac{h}{M_D G}} \geq 1.1 \tag{1.8}$$

is a better delineator of stability to bar modes, where V_m is the maximum rotational velocity, M_D is the mass of the disk, h is the disk's exponential scale-length and G is the gravitational constant. This criterion essentially measures the total halo contribution to the gravitational field relative to the disk's contribution. It is not really applicable to disks which have a significant amount of energy in random motions.

Sellwood & Carlberg (1984) have investigated the effects of transient spiral structure on the growth of random motions in the disk. Over the course of its lifetime, the disk is heated by encounters with the spiral structure. The random motions in the disk soon increased enough to stabilize the disk against bar modes. But they also stabilized the disk to the spiral structure itself! In order to keep the spiral structure, they added a massive halo to the models. The disk accretes matter from the halo, which raises the surface density of the disk and thereby effectively cools it. The halo itself provides the background potential necessary to prevent bar formation.

Recently Athanassoula & Sellwood (1986) have done N-body experiments on Kuz'min/Toomre disks, which were aimed at finding out how much of a contribution random motions could make to stability of bisymmetric modes. They found that the growth rate of these modes was a simple function of the halo mass and random velocities, i.e.

$$\text{growth rate} = 0.169q - 0.092\frac{\sigma_R}{\langle V \rangle} - 0.048 \tag{1.9}$$

in their dimensional units, where q is the fraction of the total mass which lies in the disk, σ_R and $\langle V \rangle$ are the radial components of velocity dispersion and the mean rotational velocity, both evaluated at the turnover point. Hence a stable disk could arise from many combinations of q and σ_R. They also found that σ_R can become large enough to support the disk against these modes even without the presence of a halo. This dispersion corresponds to a value of $Q \approx 2.0 - 2.5$, which would be most important in the regions inside the turnover radius. This is interesting because it shows that halos need not be dense enough near the center to stabilize the disks, but need only be massive enough to produce the observed flat rotation curves in the outer parts of spirals. Recent work by Carignan (1983) and van Albada et al (1985) supports the view that halos do exist, but are only dynamically important in the outer regions. On the other hand, the total amount of observational evidence available to test the hypothesis that the inner regions of galactic disks are hot is still very small (see section 1.5.1).

If disks of galaxies are indeed hot, the question of how the disks acquired so much random motion must be considered. Toomre (1964) presented a scenario whereby an initially unstable disk would undergo several generations of instability. Each generation would increase the random motions of the disk to a point where, after many rotations, the disk would reach a new axisymmetric equilibrium state, in which the velocity dispersions would be just high enough for stability.

Wielen (1977) has calculated the cumulative effects of local fluctuations of the gravitational field in a galaxy, and finds that the irregularities cause stellar diffusion in phase space. His calculations are able to reproduce the ratio of the velocity dispersion components, σ_R:σ_φ:σ_z for old stars in the solar neighborhood. However, his analysis does not attempt to explain the source of these fluctuations.

Lacey (1984) has proposed that stellar encounters with massive clouds could be the cause of the observed velocity dispersion in the solar neighborhood. His analysis is similar to that of Spitzer & Schwarzschild (1951, 1953) who, as previously mentioned, used this mechanism only to describe the age-velocity dispersion relation perpendicular to the plane in the solar neighborhood. The inability of the theory to predict the observed ratio of dispersion components in the solar neighborhood, however, indicates that at least one other mechanism must be present.

As previously mentioned, Sellwood & Carlberg (1984) have been modelling disk heating as the cumulative effect of many stellar encounters with transient spiral structures. The fact that their models form bars in the centers is discouraging. However, they have not investigated the further effects of a strong central bar on the growth of velocity dispersions in the central regions.

It is clear from this section that the question of stability to bi-symmetric modes is still not fully understood. The hot disk solution is attractive because it takes away the need for dark halos to be dense enough to gravitationally stabilize the disk. To test this hypothesis we need to measure the run of radial velocity dispersion in the old disk of a disk galaxy.

1.5 Measurements of Internal Motions in Old Disks

1.5.1 External Systems

Many attempts have been made to obtain the kinematic information, needed to test the theories of stability, from external systems. Kormendy (1984a,b) measured velocity dispersions in two disk galaxies, NGC 1553 and NGC 936. He showed that these two galaxies are indeed quite hot near the center, with implied values of Q between 2 and 3. He concluded that NGC 1553 at least may be globally stable, whereas NGC 936 has a rather strong central bar. He suggests that the bar itself may be the cause of the high velocity dispersion and that in time the bar may evolve away. Van der Kruit and Freeman (1986) estimated the velocity dispersion in the edge-on spiral NGC 7184. Using their measured stellar mean velocities and asymmetric drift they calculated the velocity dispersion and estimated that the central values of Q may rise to between 2.1 and 3.2. These results are all very suggestive, that disks are indeed hot enough to support themselves against bar forming modes.

The use of external systems for the study of disk kinematics does suffer from some major difficulties, however. Firstly, the disk surface brightnesses are faint, and the expected dispersions are quite low. Hence the high signal to noise spectra needed are difficult to obtain, even with large telescopes. The efforts of van der Kruit & Freeman (1986) show that we are clearly near the limit of what is now possible.

Highly inclined galaxies are sometimes observed in an attempt to measure velocity dispersions in the plane. However, this will not give a direct measure of the interesting kinematic components, i.e. the mean velocity $\langle V_\varphi \rangle$, and the radial and azimuthal components of velocity dispersion σ_R and σ_φ. The observed velocity profile through a finite size slit will be a line of sight projection with contributions from σ_R, σ_φ and the rotational velocity, all from various galactocentric distances. The only component which is directly observable in external galaxies in σ_z, in face-on systems. However, this component is dynamically less important than σ_R, when considering questions of global stability.

1.5.2 The Milky Way

We *can* do such a kinematical study in the Milky Way, and this is the subject of this thesis. The idea is to measure radial velocities of a large sample of individual stars in various directions in the galactic windows around the disk. By doing this, we can build up a picture of the kinematic state of the old disk of this spiral galaxy over a wide interval of galactocentric distance (from near the center to about 17 kpc).

The disk contains giants from about class F8 to M8. We wish to restrict ourselves to the older stars in the disk. For reasons which will be discussed in Chapter 2, we chose to use middle to late K giants. These stars are intrinsically very bright and hence can be measured to large distances ($\approx$ 10 kpc from the sun).

We had to do our own photometric survey down to about $V = 16$, and we chose our candidate giants by their broadband colors. Hence some of the stars in our sample are bound to be not distant red giants, but foreground red dwarfs. The question then arises: by choosing stars by color alone, will we be choosing mainly red giants or red dwarfs. We calculated the numbers of giants and dwarfs expected in each of our regions using the Bahcall & Soneira (1980) model, with a realistic run of reddening for our galactic window included. In all cases, for the color and magnitude range we were considering, the number of disk giants well outweighed the number of expected foreground dwarfs. The reason is that the volume element to a given limiting apparent magnitude for the giants is so much larger than that for the dwarfs. For the regions interior to the solar circle, the disk density distribution also favors the more distant stars; regions outside the solar circle will only be affected slightly in favor of the nearer stars, as the gradient of the density function becomes quite flat.

The next problem is that of luminosity classification. If the odd dwarf does come along, how do we know it? This is where interstellar reddening actually becomes helpful! Although the regions we chose had low absorption, they all still had 0.4 to 0.5 magnitudes of reddening in $(B-V)$. For a reddening of 0.4 magnitudes, a K giant of $(B-V)_o = 1.2$ would have an observed color $(B-V) = 1.6$. (The bluest stars we used has $(B-V)_o = 1.2$: see Chapter 2.) If we then survey an area of sky for stars with an observed color $(B-V) = 1.6$, we will find these reddened K giants and *unreddened* foreground M dwarfs. As K giants and M dwarfs have such dissimilar spectra (the latter have very prominent TiO and MgH bands), luminosity discrimination is very easy.

Next we consider the problem of the mixture of stellar ages in the old disk. It is the kinematics of the old stars which will tell us whether the disk is globally stable, and it is their metal abundances which will tell us about the history of chemical enrichment in the galaxy. As was mentioned before, it is a well known fact that the vertical scale-height and vertical velocity dispersion of objects in the disk increase with the age of the objects. Thus to ensure that as many of our stars were of the old population, we chose regions which were slightly out of the plane, with $b \leq 5^o$. At $b = 4^o$ and at a typical distance from the sun of about 5000 pc, this gives a z distance of about 350 pc above the plane, which is well about the scale-height of about 100-200 pc for the younger disk objects.

Kinematically our goal is to measure $\langle V_R \rangle$, $\langle V_\varphi \rangle$, σ_R and σ_φ over a long baseline of radius in the galaxy. As will be seen in Chapter 4, at an arbitrary location along some line of sight, the observed velocity of a star depends on its the true radial and tangential velocities, V_R and V_φ, as well as its galactocentric distance, R. Hence to measure V_R directly, we first chose two regions close to the directions $\ell = 0^o$ and $\ell = 180^o$. These will give a direct measure of the radial variation of $\langle V_R \rangle$ and σ_R because the tangential components simply project out. For the other regions, in order to measure V_φ directly, it is necessary to chose stars which are near the subcentral or tangent point. Here the V_R component is normal to the line of sight and hence projects out. In practice this is difficult as the projection factors are strongly dependent on the value of R. Therefore we decided to use our values of $\langle V_R \rangle$ and σ_R, which we measured in the $\ell = 0, 180^o$ fields, to model out the known contributions of $\langle V_R \rangle$ and σ_R to the observed velocity distribution and solve for $\langle V_\varphi \rangle$ and σ_φ directly.

Our main aim observationally in this thesis was to obtain spectra of as many of these red giants as we could. We took medium resolution spectra of about 600 red giant stars. From the spectra we measured cross-correlation velocities. The spectra also gave equivalent width measurements for abundance estimates and were used to calculate synthetic DDO colors. These spectra were taken between July 1983 and June 1986 on the MSO 1.9 meter, the 3.9 meter Anglo-Australian Telescope, and the 2.1 meter NOAO telescope at Kitt Peak National Observatory.

1.6 Chemical Abundance Gradients

Another property of galactic disks that we should consider is the evolution of chemical abundances and chemical gradients in the galactic disk. Some early work on the subject was done by Aller (1942) who showed that the spectra of H II regions in M 33 depended strongly on their locations in the galaxy. This work was summarized and confirmed by Searle (1971)

Janes (1979) has summarized the work of several authors on chemical gradients in the Milky Way. In that paper, Janes himself measured the chemical abundance of G and K stars in the galaxy using DDO photometry. He combined these with results of previously published UBV photometry of some galactic open clusters to obtain a gradient of -0.05 dex kpc^{-1} in $[Fe/H]$. This is similar to the results found by many authors. However, the studies of galactic chemical gradients have concentrated almost entirely on young and intermediate age objects. It would be very interesting to know the run of abundance in the *old* disk, as this can provide insight into the enrichment of the interstellar medium at the time when the old disk was young.

1.7 Thesis Outline

Since we have now covered our plan of attack for this project, we present here a brief outline of the thesis. Chapter 2 will concentrate on the photometry done for this project, how it was reduced and how distances were derived for the stars. In Chapter 3 we discuss the spectroscopic observations and reductions. We also discuss the cross-correlation method, the abundance calibration and the calibration of the synthetic DDO colors from the spectra. Chapter 4 describes the basic theory of our velocity deprojections in the R and φ directions. It also presents some of the raw results of the kinematic and abundance information. In Chapter 5 we discuss possible interpretations of the results presented in Chapter 4. In Chapter 6 we recapitulate what we have learned in this project and what conclusions we have been able to draw from the information in the previous chapters. We also discuss some plans for future work. Finally, Appendix I shows how we estimated the errors in our stellar photometric parallax distances.

CHAPTER TWO

Photometric Observations and Reductions

2.1 Introduction and Selection Criteria

In order for this project as outlined in the previous chapter to succeed, a large number of candidate giants was needed for spectroscopic observation. We decided on red giant stars because they are the brightest of the old stars and hence their kinematics can be measured to large distances; as we shall show later, most of the giants which we will observe are indeed old.

Stars with $(B-V)_{\circ} > 1.5$ were excluded because the long period variable stars begin to appear at about that color. As we wish to determine our distances from photometric parallaxes, variable magnitudes and colors are clearly undesirable.

A cutoff in the blue is also necessary. Figure 2.1 illustrates the problem, that giants of different ages have different absolute magnitudes at the same intrinsic color. Thus if the old disk includes stars of different ages, we would have significant distance uncertainties for the bluer giants. However, the funnel effect seen in that figure reduces the spread in absolute magnitude for the stars. We therefore imposed a blue cutoff at $(B-V)_{\circ} < 1.2$ in order to take advantage of this funnel effect. Thus with colors in the range $1.2 \leq (B-V)_{\circ} \leq 1.5$, our stars are middle to late K giants.

2.2 Selection of Candidate Stars and Distance Determination

Since the goal of this project was to measure the radial changes of the kinematic properties and chemical abundance, a large sample of stars was needed over a wide range of distances. As it was necessary for some of the stars in the sample to be as faint as $V \approx 16$, no existing survey of K

Figure 2.1– Isochrones for Galactic Clusters from Eggen & Sandage (1969).

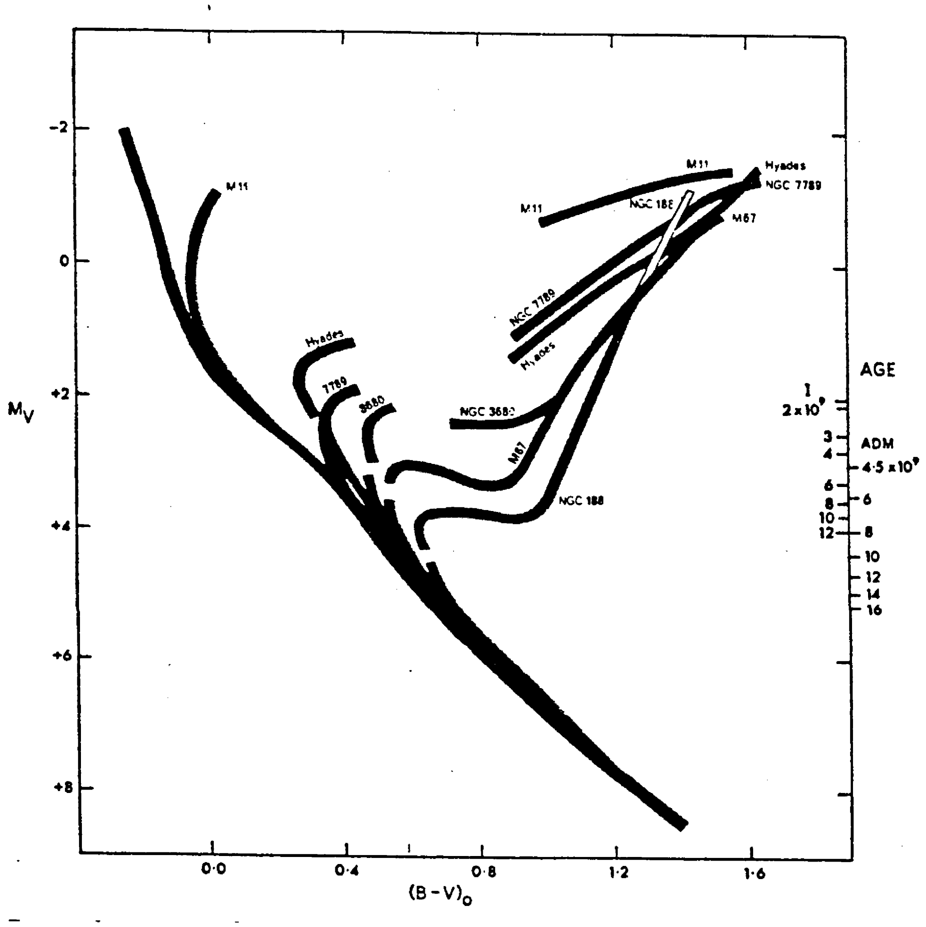

M11
Hyades
7789
3680
NGC 3680
M67
NGC 188
NGC 7789
Hyades
M11
M11
NGC 188
Hyades
NGC 7789
M67
AGE
1
2×10^9
3
4
ADM
4.5×10^9
6
8
10
12
6
8
10
12
14
16
M_V
-2
0
+2
+4
+6
+8
0·0
0·4
0·8
1·2
1·6
$(B-V)_0$

giants was suitable. It was therefore necessary to do our own photometric survey. We decided to identify the candidate red giants from photographic photometry of our regions of interest, using photographic plates taken with the one–meter telescope at Siding Spring Observatory. It will be shown later that the reduction method employed in this project gives an accuracy that is good enough for our purposes.

The next task was to choose which regions to study. The regions had to lie close to the galactic plane and have relatively low absorption, preferably less than 1.5 magnitudes in V so that the more distant stars in the regions were no fainter than about $V \approx 16$. The choice of Baade's Window at $\ell = 0^\circ.9$, $b = -3^\circ.9$ was an obvious one, as it would give a direct measure of the radial variation of the radial component of the velocity dispersion, with negligible contamination from the azimuthal and vertical components. For our other regions, we searched the literature for distant galactic globular and open clusters which lie near the galactic plane and have low measured reddenings. All of the candidate regions were checked visually on the Palomar or Schmidt surveys for evidence of large absorption gradients near the clusters, as shown by obvious changes in the stellar density. We eventually adopted seven regions for study. The fields were chosen by galactic latitude, absorption and also by galactic longitude; it was desirable to have the regions spread around the galactic plane, so that we could also study the radial variation of the azimuthal component of the velocity dispersion and mean motion. The regions chosen and their properties are described in Table 2.1. E_c is a reference reddening, usually the reddening of the cluster in the field and r_c is a reference distance, usually the distance to the cluster. The longitude distribution of the regions shown in Figure 2.2.

Table 2.1 Regions for Observation

Cluster	ℓ^o	b^o	E_c	r_c	Ref
NGC 6522	0.9	-3.9	0.50	6300	van den Berg (1979)
NGC 6712	25.3	-4.3	0.35	7400	Sandage & Smith (1966)
NGC 5927	326.6	4.9	0.55	7200	Menzies (1974)
Circinus	311.3	-3.8	0.40	5000	Freeman et al (1977)
NGC 2660	265.9	-3.0	0.38	2900	Hartwick & Hesser (1973)
NGC 2324	213.5	3.3	0.11	2700	Becker (1960)
NGC 2158	186.7	1.8	0.43	4900	Arp & Cuffey (1962)

Figure 2.2– Longitude distribution of regions observed. The longitude for NGC 6522 has been exaggerated slightly.

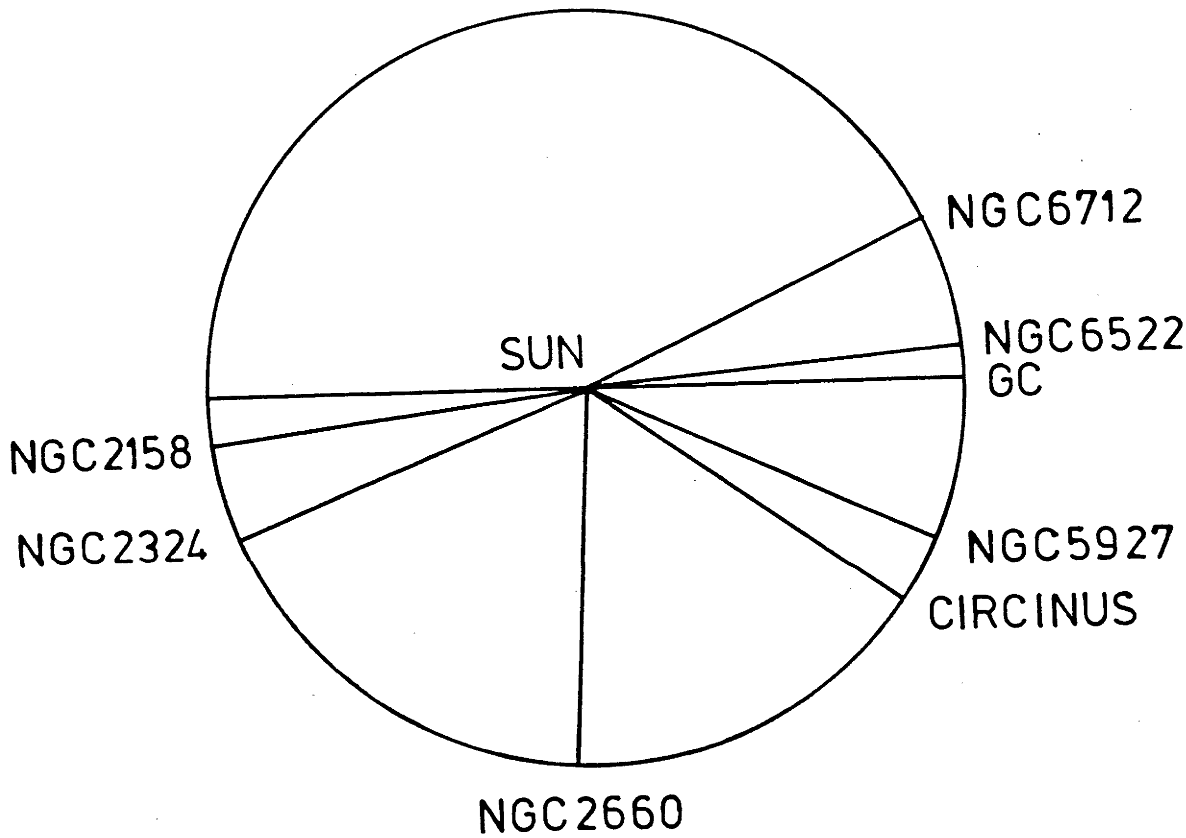
NGC6712
NGC6522
GC
SUN
NGC2158
NGC2324
NGC5927
CIRCINUS
NGC2660

We then selected K giants at particular distances from the galactic center. For example, in Baade's Window, we wish to choose stars uniformly distributed in the distance interval 1 to 8 kpc from the galactic center. The choice of these stars from our photographic photometry would be straight forward, were it not for the problem of interstellar reddening.

Near the galactic plane, the reddening will be a function of distance from the sun. As our goal is to choose stars by their distances, we clearly need to define a run of reddening with distance in each field that is consistent with the observed reddening for the reference cluster in each field.

In one of our regions (the Circinus field at $\ell = 311°, b = 3°$), Freeman et al. (1977) measured the run of reddening using OB stars. They found that the color excess increases linearly with distance modulus. Similar behavior was found by Wallerstein (1962), Sandage and Smith (1966), and Janes (1979) for other regions. Thus as an approximation we adopted a reddening model in which the color excess is a linear function of distance modulus. This model also included the assumption that the absorbing layer was 500 pc thick ($\pm$ 250 pc) and centered on the galactic plane at z = 0. We also assumed that there is no reddening within 100 pc from the sun. The law depended on whether the cluster that was being used for a reference reddening lies within or above the reddening layer. Thus we used the following:

$$E(B-V) = \left\{ \begin{array}{ll} 0 & r < 100 \text{ pc} \\ E_c \left[\frac{\log r - 2}{\log r_c - 2}\right] & r > 100 \text{ pc}, |z| < 250 \text{ pc} \\ E_c & |z| > 250 \text{ pc} \end{array} \right\} z_c > 250 \text{ pc} \quad (2.1)$$

$$E(B-V) = \left\{ \begin{array}{ll} 0 & r < 100 \text{ pc} \\ E_c \left[\frac{\log r - 2}{\log r_c - 2}\right] & r > 100 \text{ pc}, |z| < 250 \text{ pc} \\ E_c \left[\frac{\log \frac{250}{|\sin b|} - 2}{\log r_c - 2}\right] & |z| > 250 \text{ pc} \end{array} \right\} z_c \leq 250 \text{ pc} \quad (2.2)$$

where all distances are expressed in parsecs, E_c is the cluster reddening, r_c is the distance to the cluster from the sun and z_c is the distance of the cluster above the plane. Figure 2.3 shows an example of the run of reddening from this law for the NGC 2660 field.

The next step in calculating stellar distances was to adopt a color-absolute magnitude diagram for the stars. This obviously depends on the metallicity of the individual stars. As we had yet to measure abundances for any of our stars, we assumed that all of the stars in our sample had the metallicity of M 67, i.e. $[Fe/H] = 0.0$. It is important to note that this assumption was only used in the initial selection of stars for observation and not for estimating the stellar distanes in the later analysis of our data. This assumption is clearly not going to be exactly right, as: (1) there will be a certain amount of dispersion in metallicity about a mean for any given distance and (2) recent studies (Janes, 1979 and references therein) have indicated that there is an abundance gradient in the galactic disk. However, these studies have dealt almost exclusively with young and intermediate age objects in the disk, and it is not clear that the old disk has the same abundance gradient or even any gradient at all. We shall return to this point in Chapters 4 and 5. Our assumption of a uniform $[Fe/H]$ will lead to some distance errors, but is good enough for choosing stars for the spectroscopic program. The color-magnitude relation used for M 67 was from Morgan and Eggleton (1978).

The procedure for calculating the stellar distances is then straight forward. First an initial guess was made at the reddening, $E(B-V) = E_1$. Then:

$$(B-V)_o = (B-V) - E_1 \tag{2.3}$$

$$(B-V)_o \rightarrow M_v \tag{2.4}$$

$$r = 10^{0.2(m_v - M_v + 5 - 3E(B-V))} \tag{2.5}$$

Figure 2.3– The modelled run of reddening for the field NGC 2660. The cluster is shown as a filled circle.

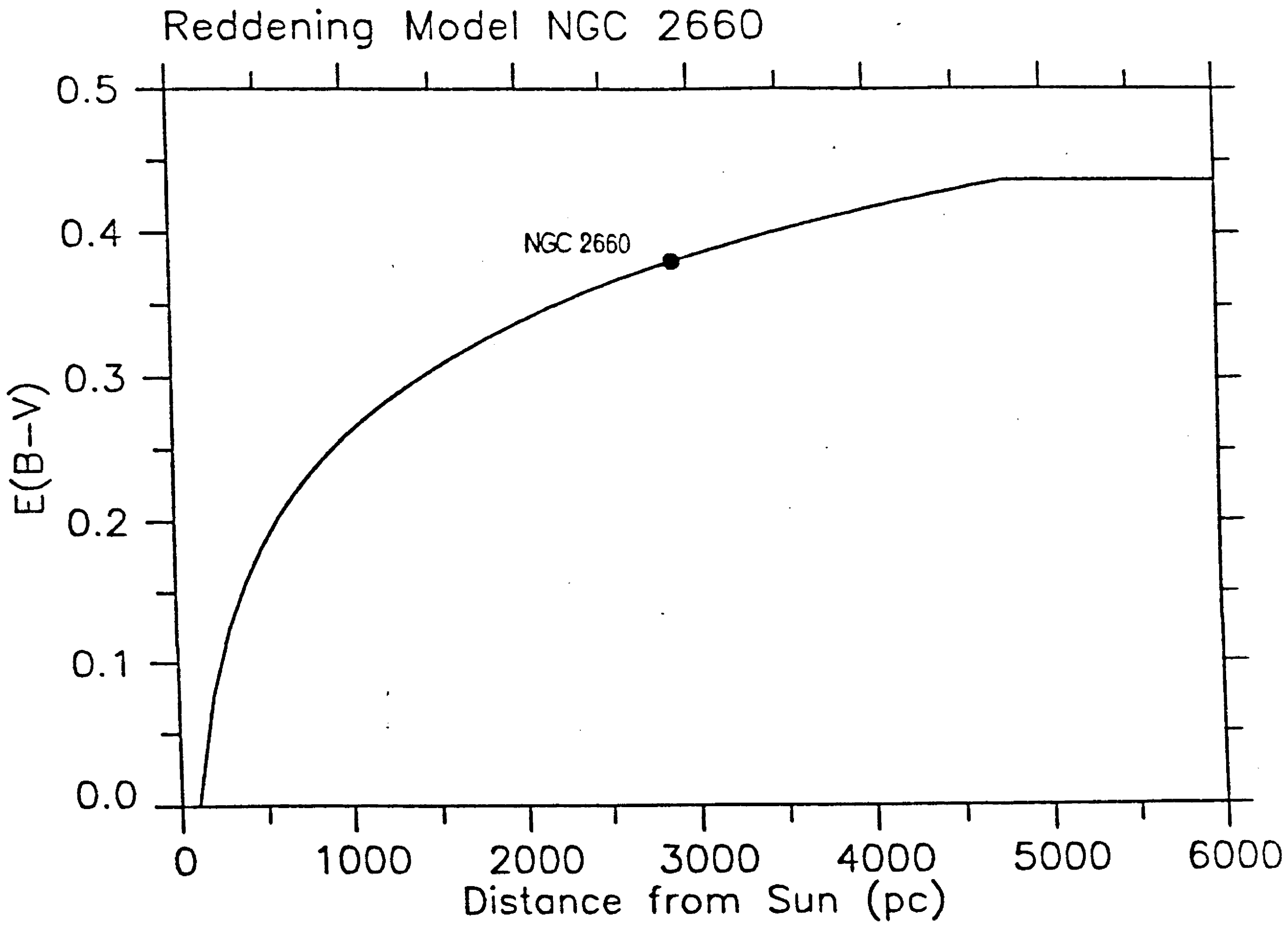
Reddening Model NGC 2660
0.5
0.4
0.3
0.2
0.1
0.0
E(B−V)
NGC 2660
0
1000
2000
3000
4000
5000
6000
Distance from Sun (pc)

This value of r can then be plugged into equations (2.1) and (2.2) to obtain a new value of $E(B-V)$. The procedure was repeated to convergence. The derived values of r, $E(B-V)$, $(B-V)_o$, combined with our color selection criteria, were then used to choose which stars from our photometric sample should be observed spectroscopically. We stress again that the final distances used in this thesis will be based on the *measured* values of $[Fe/H]$ from Chapter 3. Note that errors in photometry, reddening and metallicity will all lead to errors in the calculated distances. A discussion of distance errors is presented in Appendix I.

Our assumption that all of the red stars in a given region are giants causes no problems. As was shown in Chapter 1, a simple calculation shows that the red stars in a given region in the plane interior to the solar circle will be mostly giants. The occasional M dwarf in the sample is easily recognizable from its prominent TiO and MgH bands.

2.3 Photographic Observations and Reductions

The photographic observations were done on the Siding Spring Observatory one-meter telescope. At the f/8 Cassegrain focus, the plate scale is 25 arcsec mm^{-1} which is sufficiently large that there was no appreciable overlapping problem with faint stars, even in the most crowded regions.

The field size is about 0.8 square degrees. Vignetting reduces the useful area of the plate to about 0.7 square degrees. Thus, in some of the less densely populated regions, it was necessary to take several sets of plates offset in various directions to ensure that we had enough red stars for our spectroscopic observations in those regions.

The photography was done in two colors: Johnson B and V. The B plates were taken with Kodak IIa-O emulsion and a Schott GG 385 filter. The V plates were taken with IIa-D emulsion and a GG 495 filter. In most cases the plates were hypersensitized by baking in dry nitrogen at 68°C and then a period of soaking in dry hydrogen. The actual recipe varied from batch to batch: a typical example of a IIa-O recipe is two hours baking time and four hours soaking. This increased the speed of the emulsion by about a factor of two, which was particularly helpful at times of cold weather or precarious cloud cover. The plates were developed using standard techniques and Kodak D19 developer.

The plates were digitized using the MSO PDS 1010 microdensitometer. The PDS is operated using a system which was developed locally by Dr. G.R. Hovey.

The reduction package used for analyzing these scans was designed for use with undersampled stellar images. Thus a fairly large pixel size could be used, which made it possible to cover most of the plate with one scan. The plates were mostly taken in 2 to 3 arcsecond seeing. Therefore, at a plate scale of 25 arcsec mm^{-1} and a scanning aperture of 50 microns, an image would typically cover about 3 square pixels.

The PDS is limited in its sampling rate by the comparatively long time constant of its logarithmic amplifier. Scanning at speeds which do not allow sufficient time for the log amplifier to respond to density changes on the plate results in stellar profiles which will have a sort of zig-zag distortion. While this does not cause serious problems in uncrowded fields, it can be disastrous for some of the more crowded fields in this project, as a large amount of overlapping occurs. The PDS scans at speeds between 1 and 255 units, where 5 speed units equals 1 mm/sec. Our scans were usually done at speeds of 50 units or 200 pixels/sec for 50 micron pixels.

The software used for analyzing the PDS scans was originally developed by Kavan Ratnatunga on the ANU UNIVAC 1182 computer. While the

UNIVAC is better equipped to cope with large numbers of magnetic tapes and had better plotting facilities than the MSO VAX 11-780, several important factors caused me to rewrite the software for the VAX. The original code was written in a subset of FORTRAN IV, was largely uncommented and was completely undocumented. This made it extremely difficult for the user to understand what the software was doing to his data. Secondly, the UNIVAC is a very inconvenient, abusive and frustrating computer to use, owing to its location and extremely unfriendly operating system and editor. The fact that the UNIVAC could handle a larger number of tapes must have been a major contributor to Ratnatunga's decision to base his computational efforts at the UNIVAC, as his project created the need to read a very large number of tapes. However this was unimportant in our case, as the number of tapes generated by our PDS scans was not so large. The code was rewritten in FORTRAN V (1977 standard) and was carefully commented and documented.

The analysis of the scans began with an estimate of the mean and sigma of the sky across the plate. This was achieved by first dividing the scan map into a number of subsquares. The scan maps were generally 2000×2000 pixels, so that they were usually divided into 400 subsquares of 100×100 pixels each. Next the intensity histogram (η function) was calculated for each subsquare. These η functions are highly skewed in the positive direction (i.e. towards higher intensity) by the presence of stellar images and plate defects. Thus, to find a true unbiased mean sky value, it was necessary to employ an iterative non-symmetrical $n\sigma$ clip, where σ is the dispersion of intensity values in each subsquare and n was set to three (Newell 1979). The maximum number of iterations was ten. It was rare, however, that so many iterations were required to obtain a stable mean.

Next, the stellar images on the scan map were located as pixels more than a certain number of sigma above sky, where sigma is now the dispersion of the clipped η function. This threshold was never allowed to go below 4σ, as at such low levels the images are likely to include emulsion defects or individual grains. When a local maximum was found, a weighted mean was performed on the surrounding pixels to find the center of the image, and the image was tested to see if it was above the threshold value. Next the sky was subtracted from the area of the map surrounding the image. The density of each pixel was then translated to transmission via the relation:

$$T = 10^{-D} \tag{2.6}$$

Using transmission has the disadvantage that one loses information for bright stars, i.e. high density, as the gradient of the transmission function in equation (2.6) is quite shallow there. However none of our stars was anywhere near bright enough for this effect to matter. Using transmission has the advantage that the transmission of individual pixels can be added together directly to form an instrumental magnitude. (This is not the case with densities.) Therefore, by using transmission, we can emulate an iris photometer by calculating the effective transmission of a circular aperture from our undersampled scans. Thus we synthesized an aperture which was circular and had a diameter of 4 pixels, which was slightly larger than the image sizes of the stars in which we were interested. Finally all of the transmission in this circular aperture centered on the image was added together and normalized by its area. The total transmission was then converted to an instrumental magnitude with:

$$m_{inst} = C_0 + C_1 \Sigma T \tag{2.7}$$

where ΣT is the normalized sum of transmission for the star. This instrumental magnitude was calibrated to true magnitudes later. The whole map was searched in this way in order to find all of the stellar images on the plate. The scan maps for both colors were treated in the same way.

To match the corresponding images from both plates, we found accurate centers of position standard stars (usually SAO stars) on both scan maps. These centers were found by fitting least squares ellipses to the density contours of these standard stars. We were then able to find the plate constants for both scan maps. This allowed us to take out the effects of rotation and translation and thus enabled us to match the corresponding stellar images on the two scan maps.

Finally the stars were calibrated to true magnitudes with standards which were on the scan maps with the program stars. These standards usually came from previously published photoelectric photometry. The final calibration was done with a spline fit to the curve of true magnitude versus instrumental magnitude. The errors in magnitude were between 0.04 and 0.07 magnitudes and the errors in color were between 0.07 and 0.1 magnitudes. Thus this approach of using undersampled scans and synthetic iris photometry gave accurate results with a significant reduction in PDS and computer time.

CHAPTER THREE

Spectroscopic Observations and Reductions

Introduction

Having defined the sample of stars, we set out to observe as many of them spectroscopically as possible. Spectroscopic observations were done on three telescopes, the Mount Stromlo 1.9 meter, the 4 meter Anglo-Australian Telescope and the 2.1 meter NOAO telescope at Kitt Peak National Observatory in Tucson, Arizona. The observations at each telescope are treated in separate sections of this chapter. In addition, the AAT observations are split into two separate sections—one dealing with slit spectroscopy and the other dealing with multi-object fiber spectroscopy. There were also observations done at high resolution at the MSO 1.9 meter and the newly commissioned ANU 2.3 meter telescope, to establish the radial velocities of our local standard stars. These will also be dealt with in separate sections of this chapter. The reduction methods used for each type of observation will be discussed in the same sections as the observations. Next we will discuss the method for measuring the velocities from the reduced spectra. Finally we will describe the abundance calibrations, the measurement of the synthetic DDO colors, which were used as a check on the zero point of our spectroscopic abundances and the revision of our stellar distances.

3.1 Slit Spectroscopy at the MSO 1.9 Meter

The observations on the MSO 1.9 meter telescope were done starting in July 1983 and continued unabated until October 1985, with the exception of the months of November, December and January when either none of our regions were in the sky or those that were had stars which were too faint to be observed with this particular telescope.

The observations were made at the Cassegrain focus with the Boller and Chivens spectrograph and the Mount Stromlo Observatory Two Dimensional Photon Counting Array (Stapinski et. al. 1981). The 2DPCA was used in two different ways—CCD + 6–stack (six optically coupled electrostatic image tubes) and CCD + two coupled 18mm microchannel plates. The PCA has 745 channels in the wavelength direction and 244 rows in the spatial direction. Each pixel is 15μ (in wavelength) $\times 36\mu$.

The grating used had 600 lines mm^{-1} and was blazed at $17°27'$ to a first order Littrow wavelength of 10,000 Å. When used in second order with the CCD and 6–stack combination, the dispersion was 57.6 Å mm^{-1} or 0.86 Å channel^{-1} at λ = 5200 Å. This gave a coverage of about 640 Å and a velocity scale of about 49.9 km sec^{-1}channel^{-1}. While the 6–stack was adequate for obtaining velocity information (the mean velocity error is about 8 km sec^{-1}), it did suffer from a number of difficulties. (1) The efficiency of the stack depends critically on the efficiency of the leading image tube and we were plagued with leading tube sensitivity problems. (2) The residual magnetic field of the earth deflects the beam slightly as it passes from tube to tube. Therefore, over a period of time the direction of dispersion was rotated out of alignment with the rows of the CCD. This meant not only that the signal to noise ratio was decreased, but also that velocity information would be degraded due to the tilting of the spectral lines. Adjustments to correct this rotation problem had to be done several times per night. These tests were usually done on a nearby bright field star. Fortunately the six-stack was replaced by the 18mm tandem MCP in April-June 1984.

The 18mm tandem MCP has neither of the problems previously mentioned for the six-stack. When used with the grating as described above, a dispersion of 42.0 Å mm^{-1} or 0.63 Å channel^{-1} at $\lambda = 5200$ Å and a wavelength coverage of about 470 Å was obtained. This resulted in a better velocity scale of about 36.5 km sec^{-1}channel^{-1}.

The wavelength system was calibrated with exposures of an Fe–Ar arc. As there was a large amount of 'drift' in the system, it was necessary to take an arc exposure at least every 2000 seconds. This drift became noticeably worse at high zenith distances, and maximum exposure times had to be shortened accordingly. This drift was probably caused by mechanical movement within the spectrograph itself, in particular in the grating holder whose locking mechanism is certainly not all that it should be.

Each region observed had at least two bright local standard stars. We tried to do at least two exposures of each of these stars during the night. However, bad weather and other constraints sometimes prevented our doing so. These stars gave us a measure of the velocity errors from night to night.

Although the PCA has 244 useable rows we recorded only about 20 rows. These provided enough information to get the entire spectrum of the star plus an ample number of rows to be used for sky subtraction. In regions where crowding was a problem it was sometimes necessary to record extra rows to make sure sufficient sky was recorded.

The reduction of the spectra was begun by cross-correlating (see section 3.8) all of the arcs of a given night against the first arc of that night. This was done to determine whether there were any large shifts in pixels of the arcs over the night. This occurred somewhat more frequently at the beginning of our observing on the 1.9 meter, because the old arc system was a sort of plunger arrangement which had to be operated manually. The pushing and pulling of the plunger, no matter how gently, caused vibrations which occasionally produced shifts of 0.2 to 0.3 channels (10 or 15 km sec^{-1}). This was clearly unacceptable, and any star whose arcs had shifts of around 10 km sec^{-1} or greater was automatically rejected. Fortunately, in late 1983 a new arc system was installed on the spectrograph, in which a flip mirror is driven into the light path by a small motor. Once this new arc system was installed, no such sudden large shifts were noticed.

Next, all of the arcs were rebinned to a loglambda scale with the same zero point and increment. Then they were all cross-correlated against the first arc of the night again, to ensure that the rebin coefficients determined for each arc were putting all exposures onto the same scale. Any arc with a shift greater than about 7 km sec^{-1} was automatically rejected. This did not happen very often, and was generally a result of a badly exposed arc.

Next the star exposures were sky subtracted and the rows containing the star's spectrum were added together and rebinned to a loglambda scale. Next a 'supertemplate' was created by adding together all of the exposures of the local standards from the first night to created one very high signal spectrum. All of the program stars including the local standards were then cross-correlated against this 'supertemplate'. With this procedure, all stars including the local standards were treated in the same manner. The cross correlation method used was fairly straight forward and will be discussed in section 3.8. The velocities had a mean error of about 8 km sec^{-1} for the six-stack observations and about 6 km sec^{-1} for the tandem MCP observations.

What remained to be done was to tie these relative velocities back to heliocentric velocities by finding the heliocentric velocities of the local standards in each region. This will be discussed in sections 3.6 and 3.7.

3.2 Slit Spectroscopy at the AAT

These observations were done on several runs between December 1983 and June 1984. The observations were made at Cassegrain f/8 focus using the RGO spectrograph with the 25 cm camera. The 600V grating was used with blaze to collimator; this gave a dispersion of about 66 Å mm^{-1} at $\lambda = 5000$ Å at the detector.

The detector used was the Image Photon Counting System (IPCS). The IPCS has 2000 $\times 15\mu$ pixels in the wavelength direction and can be used in a variety of two dimensional configurations. We used 2000 pixels in the spectral direction and 20 $\times 55\mu$ pixels in the spatial direction, which again provided enough information for proper sky subtraction. This arrangement gave a dispersion of about 1 Å pixel^{-1} and a velocity scale of about 59 km sec^{-1}channel^{-1} at $\lambda = 5000$ Å. The length of the detector provided about 1800 Å of useful spectrum.

Comparison Cu–Ar arcs were used before and after each star in order to measure accurately the drift in the system. The internal drift in the IPCS turned out to be much smaller that with the PCA, less than 1 pixel compared with about 3 to 4 over a typical night.

As with the 1.9 meter observations, we observed two bright local standards in each field. These were each observed twice during every night of observing.

The reduction of the spectra proceeded almost identically with the procedure outlined in the previous section, with only one difference. Each night on the AAT, an exposure of the twilight sky was taken. The pixels in each row were then averaged to give a profile of the vignetting along the slit. Before sky subraction, each row of each program star map was divided by the appropriate average twilight sky value. This correction turned out to be very small. The measured velocities had mean errors of about 5 km sec^{-1}.

3.3 Multi-object Fiber Spectroscopy at the AAT

These observations were started in January 1985 and continued until April 1986; our time was scheduled as several one night runs. The major advantage of fiber observations over slit spectroscopy is the ability to observe many objects simultaneously. The field of the fiber system on the AAT is 40 arcminutes, which was just smaller than the areas we scanned on our plates and was thus ideally suited for our project.

Fiber observations have several problems and overheads. (1) About 50% of the light gets lost in each fiber. Thus exposure times have to be increased accordingly. However this is more than amply compensated for by the ability to observe 40 to 45 objects simultaneously. (2) As will be seen later in this section, reductions are somewhat more difficult as IPCS distortions make extraction of the individual spectra troublesome. However, software has been written for this purpose. (3) Pre-run preparations are more elaborate. The positions of each fiber is set by small holes drilled in a brass plate which is placed at the Cassegrain focus. These positions must be determined to sub-arcsecond accuracy, lest the light of the star misses the fiber. Since these plates must be ordered well in advance, the accurate coordinates of each program object must be known at least 3 to 4 weeks before the night of observations. This involves a significant amount of time at the PDS to do the required astrometry as accurately as possible. (4) Although the same spectral resolution with the fibers as one gets with a 400μ slit, the limitations of the IPCS external memory only allow the use of 1020 pixels in the wavelength direction with the fiber system. This is half the number used for regular slit spectroscopy. Thus with the fibers each wavelength pixel is set to about 30μ. Hence, there is some loss of spectral resolution and the wavelength pixels are doubled: therefore velocity errors are somewhat larger. These problems in no way outweigh the ultimate benefits of multi-object observations.

There were two sizes of fibers from which to choose. The 200μ diameter fibers have a size of 1.3 arcseconds on the sky. The 400μ diameter fibers are thus 2.6 arcseconds on the sky. There were two 400μ fiber bundles, which allowed one to set up one plate while observing another. This was not possible with the 200μ fibers at the time that our observations were being done, as there was only one 200μ bundle; this gain in efficiency dictated our choice to use the 400μ fibers. Each bundle has 50 fibers. However it is not generally possible to observe 50 objects, as there are invariably a few fibers which have been broken and some of the others must be dedicated for sky observations. Generally one can observe between 40–45 objects at a time. There is also a companion guider bundle with four small bundles of seven fibers each. These are in a circular pattern, with six fibers surrounding one, and are used on bright stars in the field for guiding the telescope. This feeds directly in to the TV guiding system and can be monitored constantly.

Apart from the use of the fiber coupler, the setup of the telescope remained the same as with slit observations. The 25 cm camera, IPCS, 600V grating and the RGO spectrograph were all used as before.

As many stars were being observed simultaneously, the original procedure of reobserving local standard stars several times a night would have wasted a lot of time. Hence the following procedure was adopted. (1) The local standard stars were still observed on each plate. They were used to set the zero-point of the velocities to a heliocentric frame. (2) We did several exposures (at least two) of each region. Each exposure had enough signal in it to calculate a reliable velocity for each program star (the greater amount of signal being needed for abundance measurments). The velocity error of the observations of the region was then calculated as the sigma of velocities of the individual stars from exposure to exposure. (3) Arcs were taken at least every 1000 seconds. As the entire IPCS area was being used, it was critical to monitor the stability of the system.

The reduction of these spectra is not as straight forward as it was with the slit spectra. The individual spectra have to be located and extracted from the recorded array. At the IPCS cathode, the spectra are essentially parallel: however, the 'pin-cushion' distortion in the image tube bends the spectra significantly especially near the edges of the IPCS field.

Programs written by Dr. J.R. Lucey of the Anglo-Australian Observatory were used to locate and extract these spectra. The program first locates the center of each spectrum from initial parameters, given by the user, which specify the row of the array on which the middle of the first spectrum lies and the average distance between each spectrum. Then the program finds the central row of each spectrum at many points in the direction of dispersion, by doing a centroid fit over a window which has an adjustable location depending on where the previous center was located. The program then extracts the spectra based on a parameter, specified by the user, which gives the approximate width of each spectrum.

Sky subtraction was the next problem, because the fibers have different transmission efficiencies. Twilight exposures can be used to work out the relative transmissions of each fiber, which can then be used as mulitipliers when subtracting the sky. We can also use the [OI] λ5577 line which is present in the night sky at Siding Spring. The grating angle was set so that this sky line would appear near the end of each of the spectra. Thus the amount of sky subtracted was adjusted so that the peak emission at λ5577 was removed. As both procedures seemed equally valid we decided to use the latter because it was less time-consuming. Sky subtraction was done after rebinning so that all spectra were on the same wavelength scale.

As was previously mentioned, the velocity errors were calculated from the repeatability of each velocity over several exposures. The final velocities were calculated by using the sum of all exposures. Again, they were cross-correlated against a 'supertemplate' consisting of the sum of the local standard star spectra. The velocity errors here were about 8 km sec^{-1}.

3.4 Slit Spectroscopy at the KPNO 2.1 Meter

These observations were done on four nights in January 1985. Owing to the declination of our anti-center field (near NGC 2158: $\delta \approx 24^o$), it would have been very difficult to get adequate spectra of the number of stars needed from Mount Stromlo or Siding Spring.

Four nights of dark time were allocated on the KPNO 2.1 meter telescope. The observations were made at the Cassegrain focus with the Gold spectrograph, the Wynne 'C.J.' Camera and the intensified image disector scanner (IIDS), coupled with the cooled RCA glass three–stage magnetically focussed image tube with S–20 photocathode and P–11 phosphor screen.

The grating used had 600 lines mm^{-1}. and was blazed to a first order Littrow wavelength of 11,000 Å. The grating was used in second order and gave a dispersion of 39.5 Å mm^{-1} or 0.9 Å $channel^{-1}$. This gave a coverage of about 900 Å and a velocity scale of about 54 km $sec^{-1}channel^{-1}$ at $\lambda = 5000$ Å.

The wavelength system was calibrated with exposures of He-Ne-Ar comparison arcs. These exposures were taken before and after each star.

As before, the observations included two bright local standard stars. Two observations of each of these stars were done each night. These again provided a check on the velocity errors. In addition two velocity standard stars were observed. These were used to put the velocities on an heliocentric zero point.

Much of the reduction was done automatically with the DEC 11/44 computer at the telescope. The user specifies which of the files are comparison arcs and which are program objects and then identifies a few of the arc lines to give a rough wavelength calibration. The program then identifies the rest of the arc lines and works out a wavelength solution. The solution is then fitted by a sixth order Legendre polynomial and the coefficients are stored. The wavelength calibration for program objects is done as a linear interpolation in time between arc exposures on either side of the program object. Thus most of the time consuming work is done with no user interaction at all.

What remained to be done was to sky subtract the exposures. As the IIDS is a dual channel spectrometer, it is standard practice to do several exposures (generally 4) of each object in alternating apertures. Thus after sky subtraction the exposures of the program objects needed to be added together.

The velocities again were found by cross–correlation with a 'supertemplate' star. The relative velocities were calculated from the previously mentioned velocity standards. The velocities obtained had errors of about 4 km sec^{-1}.

3.5 Echelle Spectroscopy at the SSO 2.3 Meter

These were done in April 1985 by G.A. Wilson and K.C. Freeman using the echelle spectrograph on the newly commissioned 2.3 meter telescope at Siding Spring Observatory. The MSO 2DPCA with 18mm tandem MCPs was used as the detector. The echelle used gave a dispersion of about 5 Å mm^{-1} or 0.075 Å $channel^{-1}$. This corresponds to a velocity scale of about 4.5 km $sec^{-1}channel^{-1}$ at $\lambda = 5000$ Å.

The stars observed were some of the bright local standard stars in some of the regions of this project. In addition, radial velocity standard star exposures were taken so that the final velocity could be tied back to a heliocentric frame.

The data was reduced by G.A. Wilson. As the echelle orders fell on the PCA in a very similar fashion to spectra from the AAT when using the fiber coupler, the reduction of this data was done using a similar procedure to that outlined in section 3.3. The data from the individual orders were reduced independently and the resulting velocities averaged to give the final results. The velocity errors here were about 1 km sec^{-1}.

3.6 Coudé Spectroscopy at the MSO 1.9 Meter

These were done in December 1985 and May 1986. The MSO 2DPCA was used as the detector. The grating had 600 lines mm^{-1}, was blazed to 16,000 Å and was used in third order. This gave a dispersion of 6.6 Å mm^{-1} or 0.10 Å channel^{-1} which corresponds to a velocity scale of 5.8 km sec^{-1}channel^{-1}. For comparison we used exposures of a thorium arc lamp. These were taken once per hour. The stars observed were the rest of the local standards which had not already been observed at high resolution. Again radial velocity standards were also observed. The reduction method used was essentially identical to the one described is section 3.1. The reductions of the December 1985 run were carried out by C.M. Flynn. The velocity errors here were again about 1 km sec^{-1}.

3.7 Conversion of Relative Velocities to a Heliocentric Frame

A large number of spectra were taken during many different observing runs during the course of this project. The next problem was getting all of the resultant velocities onto a single heliocentric system. Generally bright radial velocity standards were not observed on the same nights as the program stars. However, local standards were observed on every night. As accurate heliocentric velocities of the local standards had been measured at high resolution, the program star velocities could all be converted to heliocentric velocities.

3.8 The Cross-correlation Procedure

We used the method of cross–correlation. This is dealt with in a fairly detailed manner by Simkin (1974) and Tonry & Davis (1979), so this discussion will only highlight the main points. First we give a short discussion on how the spectra were prepared.

As was previously mentioned, the spectra were all rebinned onto a loglambda scale, (i.e. a linear velocity scale). Next, the mean intensity was calculated and subtracted from each spectrum and the spectra were divided by the standard deviation of the intensity. This puts all the spectra on the same correlation coefficent scale and ensures that an auto-correlation will give a correlation coefficient of 1.0.

As our cross correlation technique uses Fourier methods, it was necessary to taper the ends of the spectra with a cosbel function:

$$\tilde{F}_L(x_i) = F(x_i)\left[1 - \cos\frac{\pi x_i}{2\Delta x}\right] \tag{3.1}$$

$$\tilde{F}_R(x_i) = F(x_i)\cos\frac{\pi x_i}{2\Delta x} \tag{3.2}$$

where the subscripts R and L refer to the left and right hand sides of the spectra, Δx is the total length of the region to be tapered and x_i is the pixel number within that region. The region size was usually chosen to be 5 to 10% of the total spectrum size, i.e. for a 2000 pixel spectrum, a 5% cosbel would taper 100 pixels on either side.

The cross correlation function is defined as:

$$C(\Delta) = A\int_{\lambda_1}^{\lambda_2} F(x)G(x-\Delta)dx \tag{3.3}$$

where $F(x)$ is the program star spectrum, $G(x)$ is the template star spectrum, Δ is the shift in λ and A is a normalizing constant. This function can be rapidly evaluated in the Fourier domain. The spectra were therefore Fourier transformed:

$$f(k) = \sum_{i=0}^{N-1} F(x_i)\exp\frac{-2\pi i k x_i}{N} \tag{3.4}$$

$$g(k) = \sum_{i=0}^{N-1} G(x_i)\exp\frac{-2\pi i k x_i}{N} \tag{3.5}$$

Before the cross correlation product was taken, the transformed spectra were filtered by a cosbel at low frequencies and high frequencies. The former had the effect of flattening the spectrum and thus removed any contribution of the gross curvature of the spectrum to the final velocity results. Removal of the high frequencies resulted in the smoothing of PCA two-point noise and photon noise, and thereby smoothed the final cross–correlation function. Typical values of the smoothing channels for a 1024 point transform were (3,150,200). This means that there is a linear filter increasing from zero at channel 1 to 0.5 at channel 4 (3 + 1), then a cosbel from 0.5 at channel 4 to unity at channel 7 ($2 \times 3 + 1$); from channel 7 to 149 the transform was left unaltered; from 150 to 200 the transform was cosbelled down to zero and from 200 to the end the transform was set to zero.

Next the transformed and smoothed spectra were multiplied in the Fourier domain which leads to

$$c(k) = Af(k)g^{*}(k) \tag{3.6}$$

where $g^{*}(k)$ is the complex conjugate of $g(k)$ in equation (3.5). Note that because of the definition in equation (3.6) this operation is not commutative. The constant A in Tonry & Davis (1979) depended on the rms of each of the spectra. However, since we had already divided each spectrum by its standard deviation, the constant A is simply $1/N$. This normalized function was then inverse Fourier transformed to give $C(\Delta)$ in equation (3.3). The maximum of $C(\Delta)$ was found by locating a zero in its first derivative by linear interpolation. This shift then corresponded to the relative velocity (in log channels) of the program star with respect to the template, i.e.

$$\Delta \cdot V = (v_{*} - H_{*}) - (v_{T} - H_{T}) \tag{3.7}$$

where V is the velocity per logchannel and H is the program star and template heliocentric corrections and v is the program star and template true velocities.

3.9 Abundance Calibration

As mentioned in chapter 1, one of the primary goals of this study was to measure the run of metallicity with radius in the old disk. This can provide insight into the history of chemical enrichment of the interstellar medium of the disk. The metallicity of each individual star is also an important factor when estimating its distance from photometric parallaxes. The original approximation when selecting the stars was that all stars had metallicity like that of M 67. Hence the color-magnitude relation for M 67 was used to assign absolute magnitudes from the dereddened colors. With a good estimate of the true abundance of each star, the distance estimate will be significantly more accurate.

To determine the abundances from the K giant spectra, a procedure similar to that of Whitford and Rich (1983) was used. Metallicities were measured only for the stars done at the AAT and at the KPNO 2.1 meter, as the spectral range of the MSO 1.9 meter 2DPCA spectra was too small to allow the measurement of sufficient features. However, the AAT and KPNO stars make up the bulk of the stars which were observed spectroscopically. The procedure basically involves a measure of the strength of metallicity sensitive features. For the AAT spectra the features used were: Fe $\lambda\lambda$4384, 4405 and Mgb $\lambda\lambda$5167, 5173 and 5184. For the KPNO spectra Mgb $\lambda\lambda$5167, 5173 and 5184 and the Fe λ5270 blend were used.

The line strengths were measured by the integral:

$$W_\lambda = \int_{\lambda_1}^{\lambda_2} \left(1 - \frac{I(\lambda)}{I_c(\lambda)}\right) d\lambda \tag{3.8}$$

where $I(\lambda)$ is the intensity of the feature at λ and $I_c(\lambda)$is the intensity of the continuum at λ which was measured by linear interpolation between two nearby continuum bands. Table 3.1 shows the continuum band centers and limits of integration used in the line strength calculations.

For abundance standards a number of globular cluster giants with various known abundances and colors were observed. These are summarized in Table 3.2.

The strength of the spectral features is not only a function of metallicity but also a function of temperature. Thus it is necessary to include the intrinsic

Table 3.1 Sidebands and Limits of Integration

Feature	λ_1	λ_2	Side 1	Side 2
Fe	4380	4415	4333	4506
Mgb	5160	5190	4952	5240
Fe	5260	5280	5225	5296

Table 3.2 AAT Abundance Standards

Cluster	Star	$(B-V)_o$	$[Fe/H]$	Reference
47 Tuc	A22	1.33	-0.71	Chun & Freeman (1978)
47 Tuc	B447	1.27	-0.71	Chun & Freeman (1978)
47 Tuc	M25	1.26	-0.71	Menzies (1973)
47 Tuc	M7	1.22	-0.71	Menzies (1973)
47 Tuc	B524	1.13	-0.71	Chun & Freeman (1978)
NGC 362	1137	1.46	-1.27	Harris (1982)
NGC 362	1157	1.37	-1.27	Harris (1982)
NGC 362	2213	1.20	-1.27	Harris (1982)
NGC 3201	1613	1.07	-1.60	Smith & Norris (1982)
NGC 3201	1626	1.11	-1.60	Smith & Norris (1982)
M 67	105	1.19	0.00	Eggen & Sandage (1964)
M 67	108	1.30	0.00	Eggen & Sandage (1964)
NGC 5927	331	1.03	-0.30	Menzies (1974)
NGC 5927	234	1.27	-0.30	Menzies (1974)
NGC 5927	456	1.35	-0.30	Menzies (1974)
NGC 5927	190	1.50	-0.30	Menzies (1974)

color of the star in the metallicity calibration We used a bivariate regression (Bevington 1969) of the form:

$$\left[\frac{Fe}{H}\right] = C_o + C_1(B-V)_o + C_2 \log \Sigma W_\lambda \tag{3.9}$$

where $(B-V)_o$ is the intrinsic $(B-V)$ color of each star and ΣW_λ is the sum of the strengths of the features measured.

Figure 3.1 shows a plot of $\log \Sigma W_\lambda$ vs. $(B-V)_o$ for all the abundance standards which were observed at the AAT with the slit configuration in December 1983 and June 1984. The two lines show fits from equation (3.9) for NGC 362 and NGC 5927. The standard error of the calculated metallicities was 0.22 dex.

The fit found from equation (3.9) is shown in Figure 3.2 as a plot of line strengths, W_r reduced to a standard color of 1.32 vs. [Fe/H] where ΣW_r is defined as

$$\log \Sigma W_r = \log \Sigma W_\lambda + \frac{C_1}{C_2}[(B-V)_o - 1.32] \tag{3.10}$$

and the line plotted is

$$\left[\frac{Fe}{H}\right] = C_o + 1.32 C_1 + C_2 \log \Sigma W_r \tag{3.11}$$

i.e. ΣW_r is the expected line strength if the star had a $(B-V)_o$ of 1.32. The fit coefficients were $C_o, C_1, C_2 = -4.015, -1.265, 3.981$.

For the AAT slit observations in Dec 1983, two local velocity standard stars were observed twice over the night. Their calculated [Fe/H] values both fortuitously repeated to within 0.01 dex! For the June 1984 AAT slit run, the two local standards were each observed four times (twice in two nights): their calculated metallicities repeated to 0.06 dex. Both of these are well within the errors defined by the fit.

For the May 1985 and April 1986 fiber data, bad observing conditions at the beginning and end of both nights meant that only a few abundance standards

Figure 3.1–A plot of $\log \Sigma W_{\lambda}$ vs $(B-V)_o$ for the AAT abundance standards. The two lines show lines of constant metallicity for $[Fe/H] = -0.3$ and $[Fe/H] = -1.27$. The clusters are: M 67 (stars), NGC 5927 (filled circles), 47 Tuc (crosses), NGC 362 (filled triangles) and NGC 3201 (filled squares).

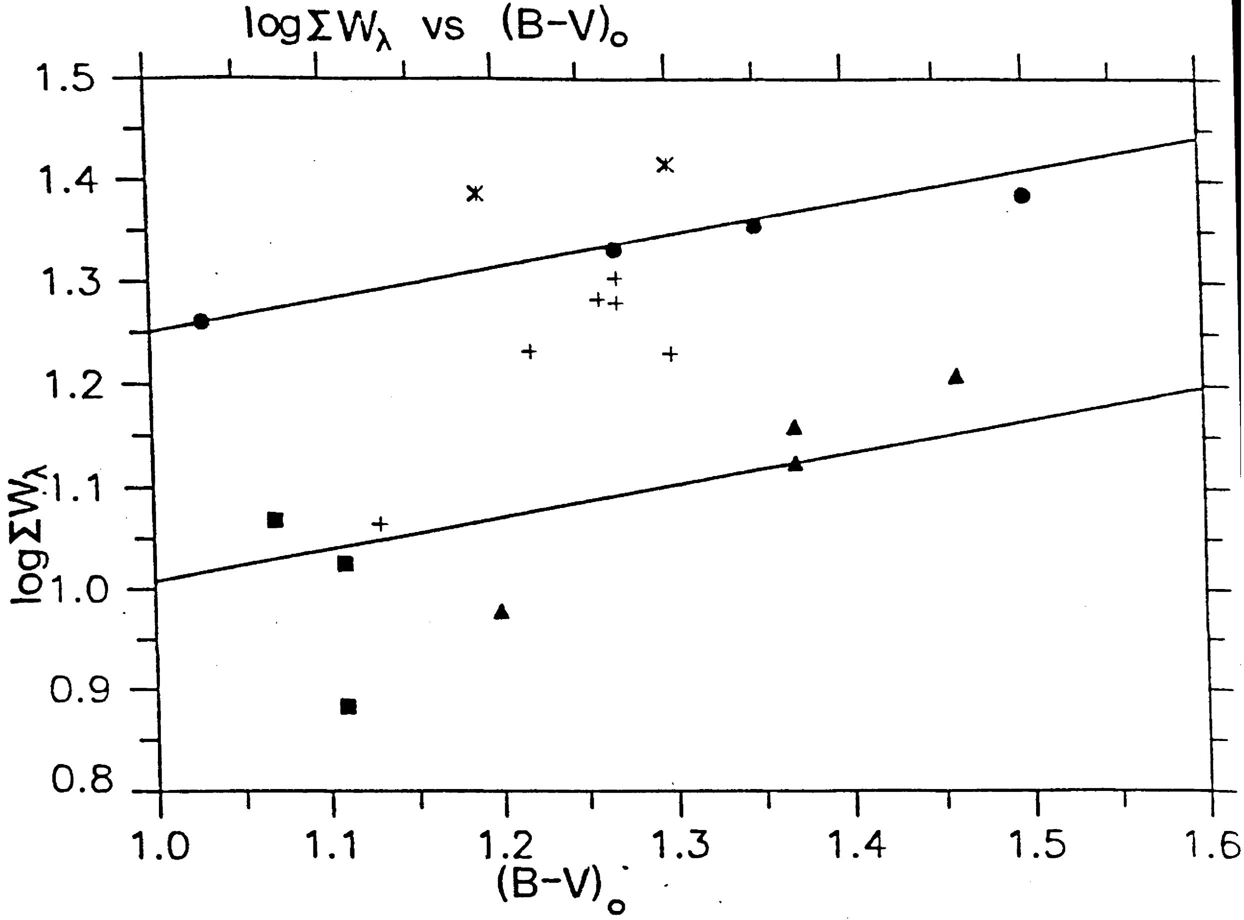
log ΣW$_\lambda$ vs (B-V)$_o$
1.5
1.4
1.3
1.2
1.1
1.0
0.9
0.8
log ΣW$_\lambda$
1.0
1.1
1.2
1.3
1.4
1.5
1.6
(B-V)$_o$

Figure 3.2–A plot of 'reduced' line width, $\log W_r$ vs $[Fe/H]$ for the AAT abundance standards. W_r is defined in equation (3.10).

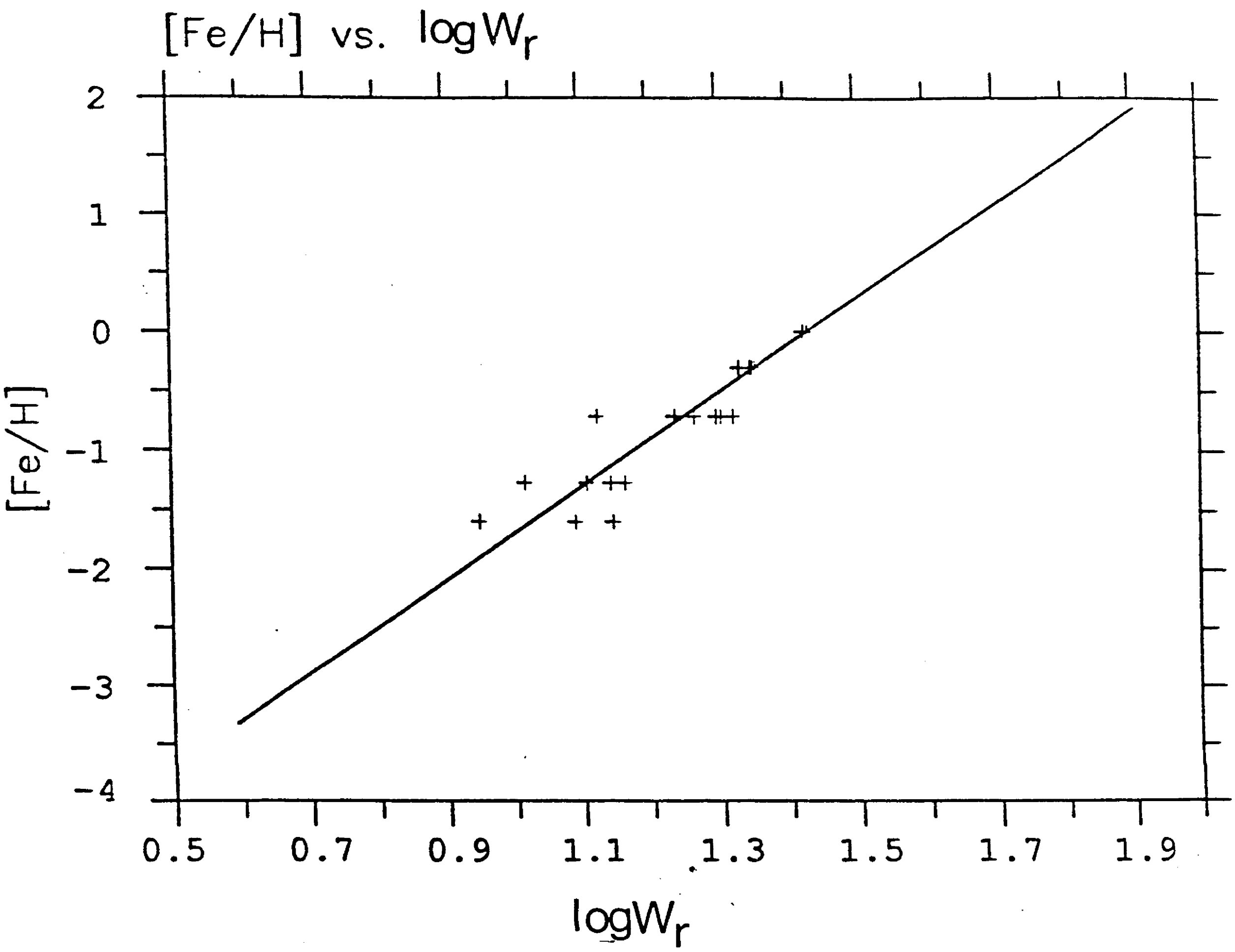

[Fe/H] vs. logW$_r$
2
1
0
-1
-2
-3
-4
[Fe/H]
0.5
0.7
0.9
1.1
1.3
1.5
1.7
1.9
logW$_r$

could be observed. The coefficients C_1 and C_2 of equation (3.9) were not independently derived for these nights: values from previous AAT slit spectroscopy were adopted. The zero point C_0 was derived independently from the local velocity standards which were observed with both slit and fiber spectroscopy. The corrections to C_0 were 0.07 dex and 0.27 dex for the May 1985 and April 1986 observations respectively.

For the January 1985 KPNO 2.1 meter data, other abundance standards had to be used. Table 3.3 has a list of these standards. The fit to these standards was good to 0.25 dex. If the star N1904-89 was removed, then the fit was good to 0.05 dex. Figure 3.3 shows $\log \Sigma W_\lambda$ vs $(B-V)_o$ for the KPNO standards. The reduced line strength fit described in equations (3.10) and (3.11) is shown in Figure 3.4. The coefficients of the fit described in equation (3.9) for these data were : $C_o, C_1, C_2 = -1.124, -1.600, 3.048$

One difference in these KPNO observations from the AAT observations is that the spectral range of the 2.1 meter observations was not sufficient to allow measurements of the $\lambda\lambda$4384,4405 Fe line. Thus the λ5270 Fe blend was substituted in its place. The accuracy of the abundances does not however seem to have been compromised.

3.10 Calibration of Synthetic DDO Colors

In order to back up our results from section 3.9, we decided to calculate DDO color indices for each of our program stars from the spectra. The DDO system has had considerable success in recent years in measuring abundance, surface gravity and interstellar reddening for late type giants. The DDO system was also ideal for use in the wavelength range which we chose to use for our spectra.

Figure 3.5 shows the response curves for the DDO 41, 42, 45 and 48 colors, (so named according to their approximate wavelength centers). These filter

Table 3.3 KPNO Abundance Standards

Cluster	Star	$(B-V)_o$	$[Fe/H]$	Reference
NGC 1904	89	0.99	-1.69	Stetson & Harris (1977)
NGC 1904	153	1.35	-1.69	Stetson & Harris (1977)
NGC 1904	15	1.49	-1.69	Stetson & Harris (1977)
M 67	135	0.99	0.00	Eggen & Sandage (1964)
M 67	164	1.06	0.00	Eggen & Sandage (1964)
M 67	105	1.19	0.00	Eggen & Sandage (1964)
M 67	108	1.30	0.00	Eggen & Sandage (1964)

Figure 3.3–A plot of $\log \Sigma W_\lambda$ vs $(B-V)_o$ for the KPNO abundance standards. Clusters observed were: M 67 (filled squares) and NGC 1904 (filled circles).

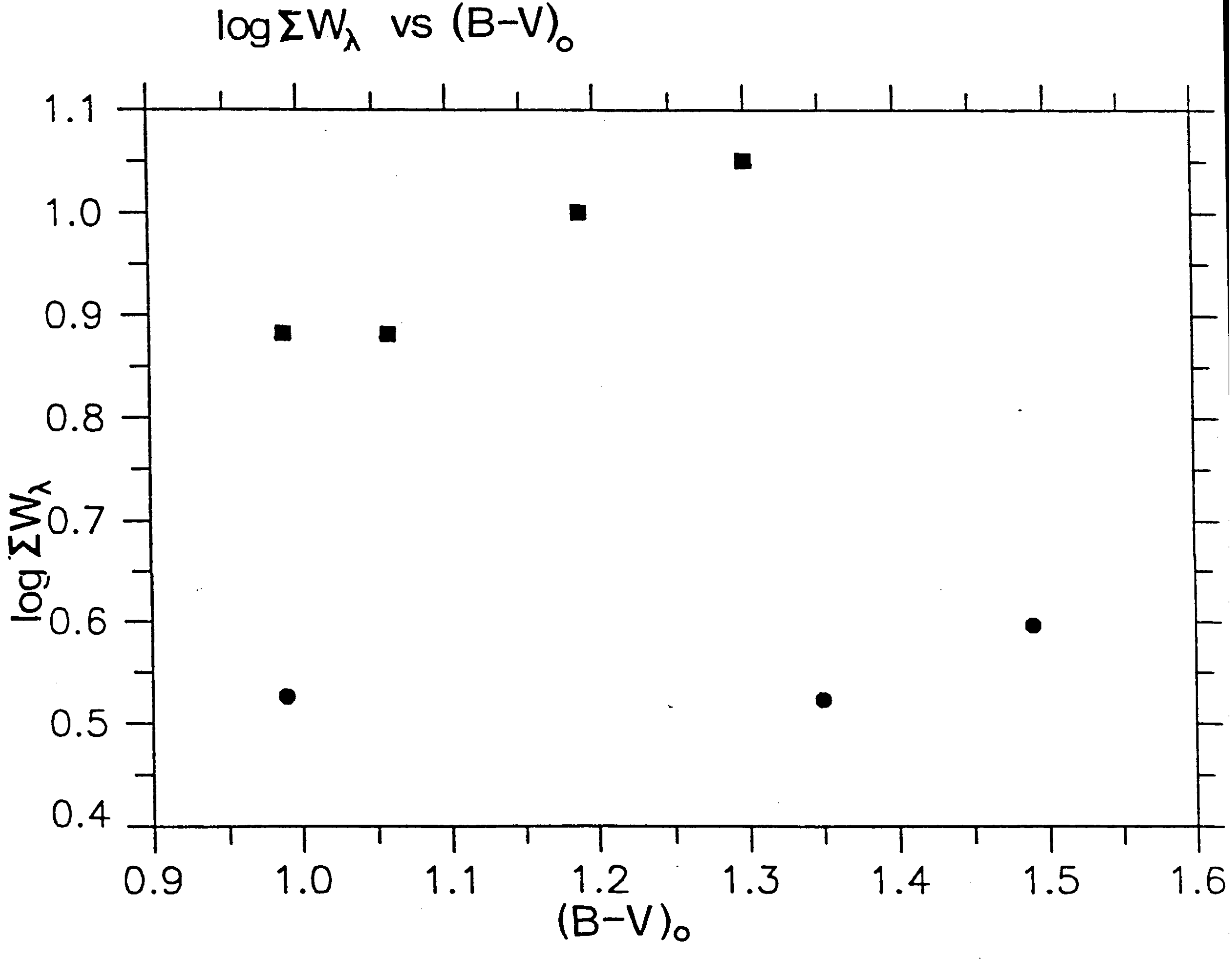

log ΣWλ vs (B-V)o
1.1
1.0
0.9
0.8
0.7
0.6
0.5
0.4
log ΣWλ
0.9
1.0
1.1
1.2
1.3
1.4
1.5
1.6
(B-V)o

Figure 3.4–A plot of 'reduced' line width, $\log W_r$ vs $[Fe/H]$ for the KPNO abundance standards. W_r is defined in equation (3.10).

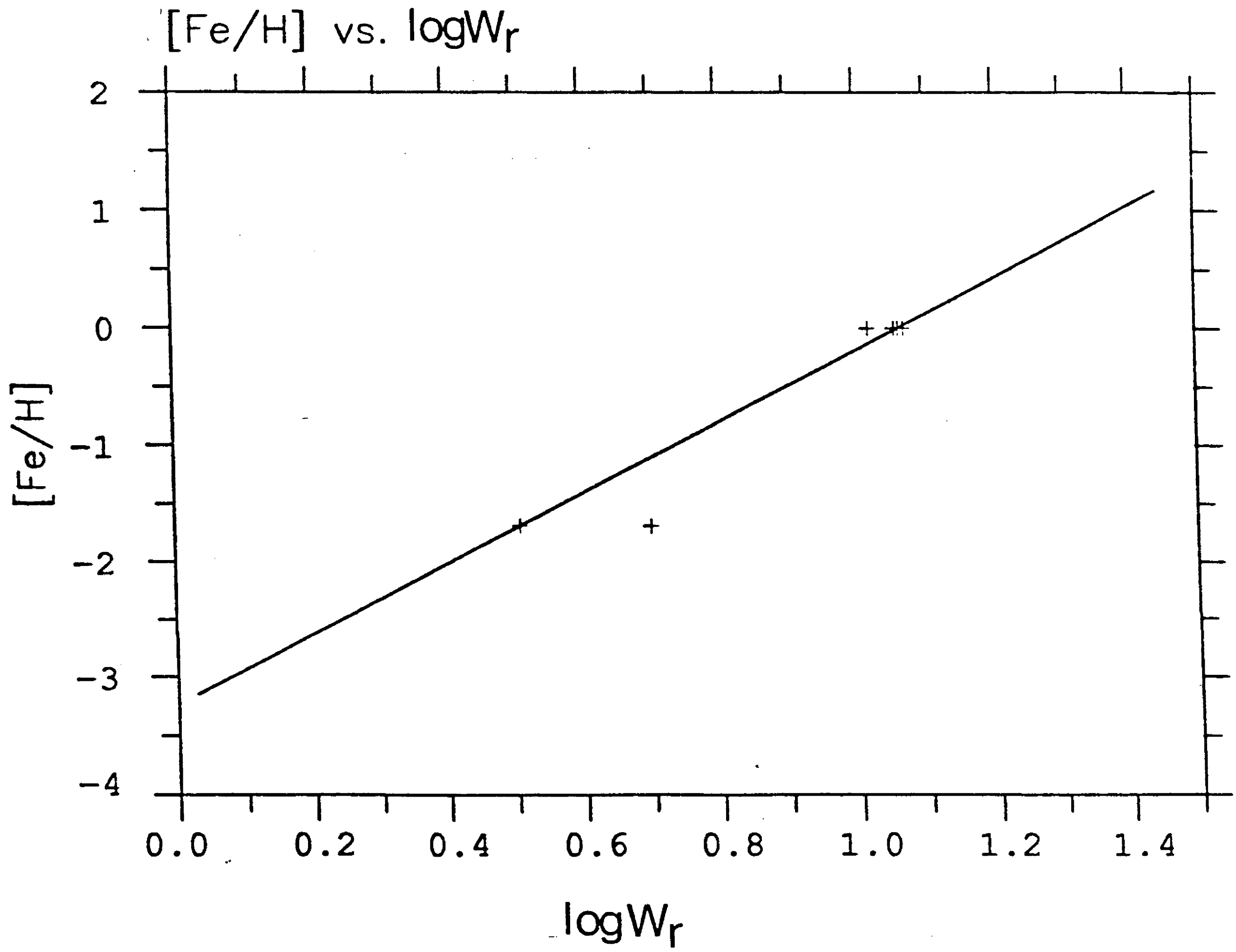
[Fe/H] vs. logW$_r$
2
1
0
-1
-2
-3
-4
[Fe/H]
0.0
0.2
0.4
0.6
0.8
1.0
1.2
1.4
logW$_r$

Figure 3.5–A plot of the transmission curves for the DDO '41', '42', '45' and '48' filters. These were measured by McClure (1976). Transmission is expressed as a percentage.

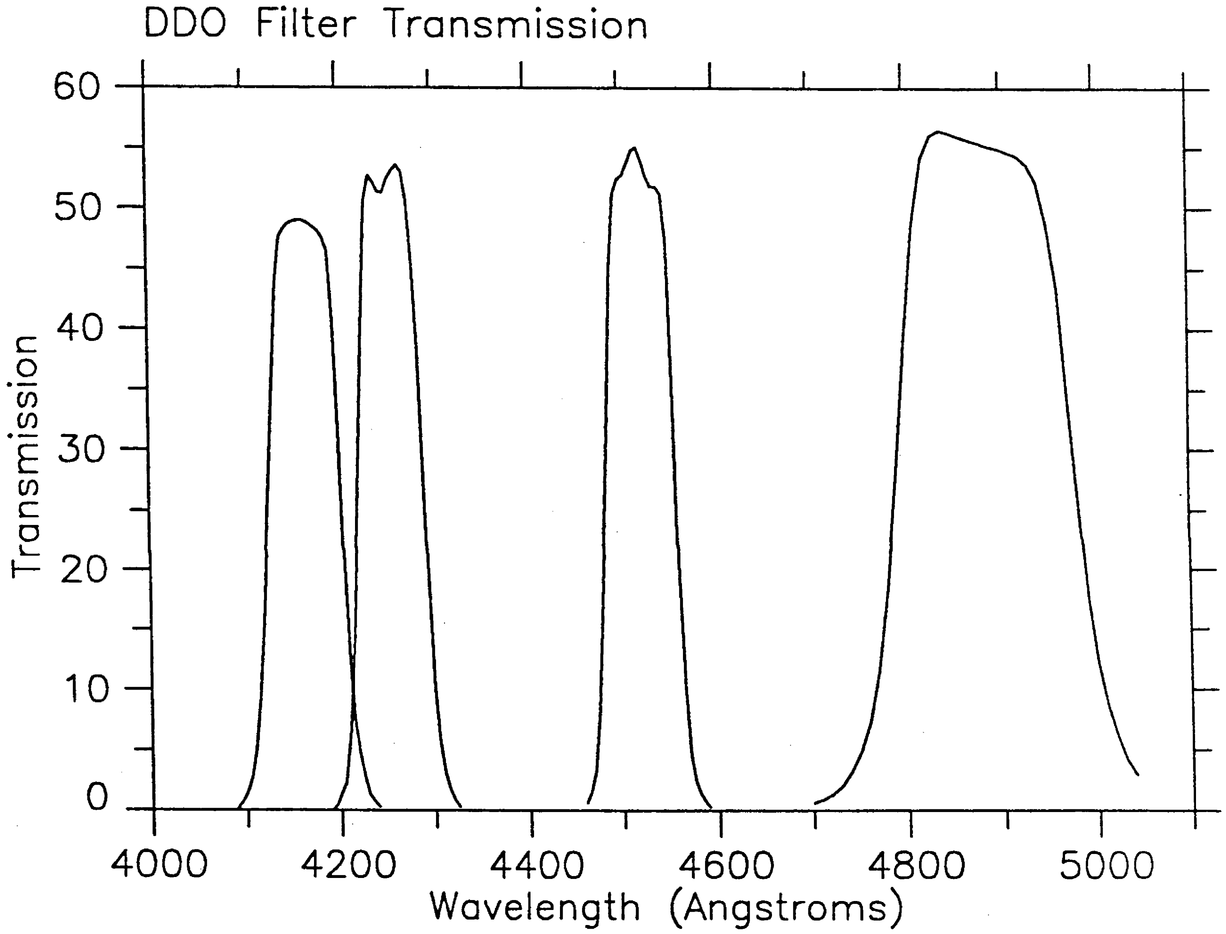
DDO Filter Transmission
Transmission
60
50
40
30
20
10
0
4000
4200
4400
4600
4800
5000
Wavelength (Angstroms)

responses were measured by McClure (1976), where transmission is a percentage. The DDO magnitudes were calculated as:

$$\Sigma_i = \int_{\lambda_1}^{\lambda_2} T_i(\lambda) S(\lambda) d\lambda \tag{3.12}$$

where $T_i(\lambda)$ is the response curve of filter i and $S(\lambda)$ is the spectrum of the star. Next:

$$m_i = -2.5 \log \Sigma_i - \epsilon_i \sec z \tag{3.13}$$

where ϵ_i is the extinction coefficient for filter i and z is the zenith distance of the observation.

The DDO magnitudes by themselves are not much use. It is in the colors where the information lies. As our data were not flux calibrated, the colors we calculate are not on the standard DDO system. In order to transform our synthetic colors to the DDO system, we did some photoelectric observations of the local velocity standards in each field.

We also have to consider the problem of reddening. The calibration of surface gravity and abundance requires dereddened colors. The reddening laws for the colors we used are:

$$\begin{aligned} C_o(41-42) &= C(41-42) - 0.066E(B-V) \\ C_o(42-45) &= C(42-45) - 0.234E(B-V) \\ C_o(45-48) &= C(45-48) - 0.354E(B-V) \end{aligned} \tag{3.14}$$

These were found by McClure and van den Bergh (1968). For our estimates of $E(B-V)$ we used the values derived from the photometric parallaxes in chapter 2. As the coefficients of reddening are fairly small, even an error of 0.05 magnitudes in $E(B-V)$ will have a fairly small effect on the final colors when compared to other errors.

The color errors due to photon statistics are of order 0.05 magnitudes. A larger source of error will be in the calculation of the mean corrections from instrumental to true DDO colors. We estimate this error will be about 0.06 magnitudes. The results of this analysis will be discussed in chapters 4 and 5.

3.11 Revision of Stellar Distances

As was previously mentioned, the original stellar distances were calculated assuming that all of the stars were giants with M 67 metallicity, and were only used to select the candidate giants from the photometry. Now that we have measured $[Fe/H]$ abundances for each of our stars we can redetermine the distances more accurately. We used color-magnitude diagrams of M 67 (Morgan & Eggleton 1978), 47 Tuc, M 3, M 5, M 92 (Sandage 1982), M 13 and M 15 (Sandage 1970) to form a three dimensional grid in $(B-V)_o$, M_v and $[Fe/H]$. The approach we used was the same iterative technique discussed in Chapter 2 with one important difference. The value of M_v was found by linearly interpolating the values calculated from the two cluster diagrams which were just above and just below the metallicity of the star in question. Hence our final distances reflect the metallicity of each individual star.

CHAPTER FOUR

Results

4.1 The Radial Kinematics

4.1.1 Basic Theory

The radial components $\langle V_R \rangle$ and σ_R were measured in two regions. One of them was near NGC 6522 (Baade's Window) at $\ell = 0\overset{\circ}{.}9$ and the other near NGC 2158 at $\ell = 186\overset{\circ}{.}7$. As the longitude of Baade's Window is fairly close to zero, the contamination from the azimuthal component of velocity will be insignificant. We must check that this is also the case for the NGC 2158 field, by estimating the contribution of the azimuthal motion of stars in this field to the observed velocity distribution and also the contribution from the motion of the LSR and the sun's peculiar motions. We define an angle α to be the angle measured in the clockwise sense from the line of sight to the radial component of the star's velocity vector, in the sense shown in Figures 4.1a,b. The observed velocity relative to the sun is then:

$$V_{obs} = V_\varphi \sin\alpha - V_R \cos\alpha - [(V_\odot + V_{\varphi\odot}) \sin\ell - V_{R\odot} \cos\ell] \tag{4.1}$$

where V_φ and V_R are the star's tangential and radial components respectively relative to a nonrotating frame, $V_\odot$ is the circular velocity of the LSR and $V_{\varphi\odot}$ and $V_{R\odot}$ are the sun's peculiar tangential and radial velocities respectively. Using the law of sines:

$$\frac{\sin\ell}{R} = \frac{\sin(\pi - \alpha)}{R_o} = \frac{\sin\alpha}{R_o} \tag{4.2}$$

Therefore:

$$\sin\alpha = \frac{R_o \sin\ell}{R} \tag{4.3}$$

Figures 4.1a,b– The geometric figures used for velocity deprojection. The angle α is defined as the angle measured in the clockwise sense from the line of sight to the radial component of the star's velocity vector.

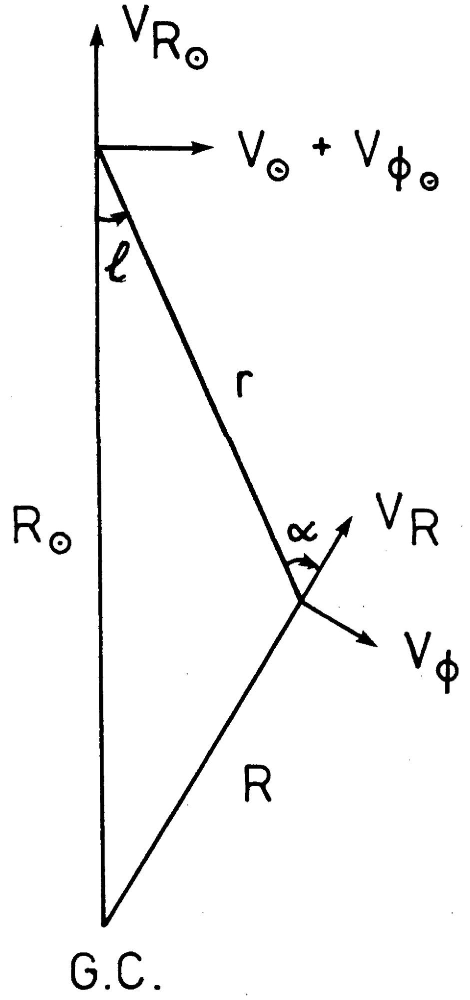

$V_{R_\odot}$
$V_\odot + V_{\phi_\odot}$
ℓ
r
$R_\odot$
α
V_R
V_ϕ
R
G.C.

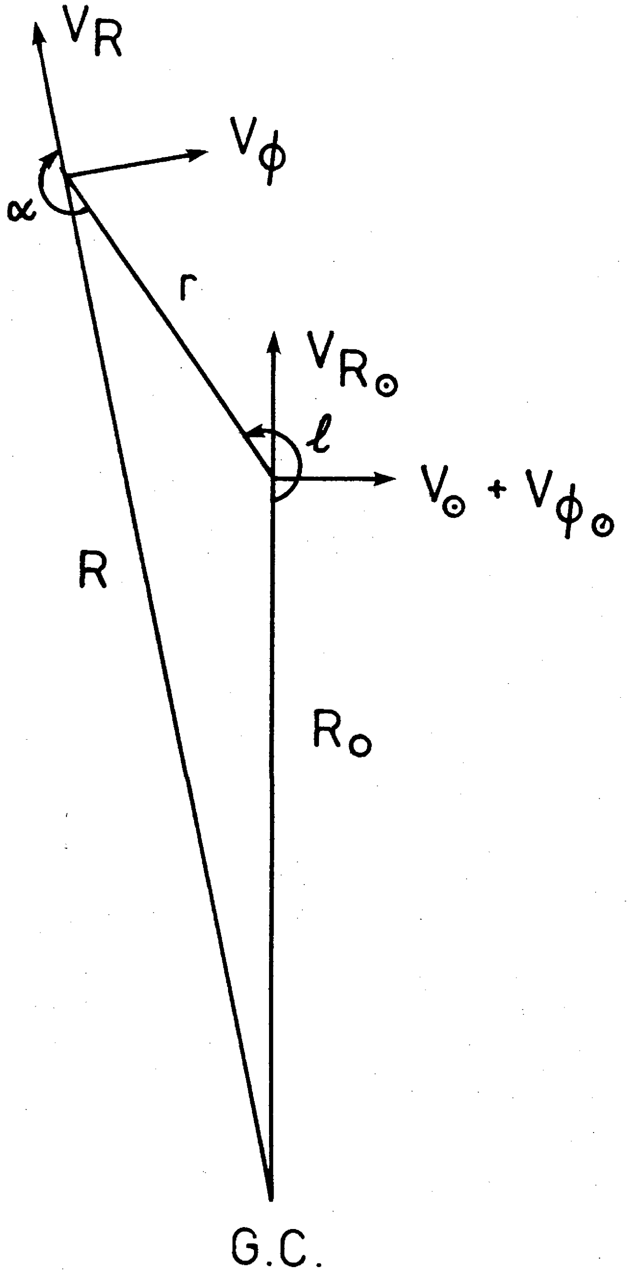

V_R
V_ϕ
α
r
$V_{R_\odot}$
ℓ
$V_\odot + V_{\phi_\odot}$
R
R_o
G.C.

Using the law of cosines:

$$\cos\alpha = \frac{R_o^2 - R^2 - r^2}{2Rr} \tag{4.4}$$

Note that the sign of $\sin\ell$ in equation (4.3) ensures that $\sin\alpha$ has the correct sign and the length of the distances R and r ensures that $\cos\alpha$ has the correct sign. For $S = -(V_\odot + V_{\varphi\odot})\sin\ell + V_{R\odot}\cos\ell$, (the solar contribution) we can solve for V_R:

$$V_R = V_\varphi \tan\alpha - V_{obs}\sec\alpha + S\sec\alpha \tag{4.5}$$

In order to calculate a mean radial velocity $\langle V_R\rangle$ for a sample of stars in some interval of galactocentric distance R, we should take into account the variation of α within this interval. Similarly, a calculation of the dispersion would have to include cross terms involving α. However, Table 4.1 shows that $\sec\alpha$ and $\tan\alpha$ vary very little over a 1 kpc bin in the Baade's Window and NGC 2158 fields. Hence it is safe to take the same value of α for all stars in a give radial bin in these two fields.

$$\langle V_R\rangle = \langle V_\varphi\rangle \tan\alpha - \langle V_{obs}\rangle \sec\alpha + S\sec\alpha \tag{4.6}$$

To calculate the radial component of the velocity dispersion σ_R, we start with equation (4.5). Calculating $\langle V_R^2\rangle - \langle V_R\rangle^2$ directly from this we get:

$$\begin{aligned}\langle V_R^2\rangle - \langle V_R\rangle^2 &= \sigma_{obs}^2\sec^2\alpha + \sigma_\varphi^2\tan^2\alpha \\ &\quad -2\langle V_{obs}V_\varphi\rangle\sec\alpha\tan\alpha + 2\langle V_{obs}\rangle\langle V_\varphi\rangle\sec\alpha\tan\alpha\end{aligned} \tag{4.7}$$

where σ_φ is the azimuthal component of the velocity dispersion and σ_{obs} is the dispersion in the observed radial velocities. If we multiply equation (4.1) by V_φ and average:

$$\langle V_{obs}V_\varphi\rangle = \langle V_\varphi^2\rangle\sin\alpha - \langle V_\varphi V_R\rangle\cos\alpha + \langle V_\varphi\rangle S \tag{4.8}$$

Next, average equation (4.1) and multiplying by $\langle V_\varphi\rangle$ gives:

$$\langle V_{obs}\rangle\langle V_\varphi\rangle = \langle V_\varphi\rangle^2\sin\alpha - \langle V_\varphi\rangle\langle V_R\rangle\cos\alpha + \langle V_\varphi\rangle S \tag{4.9}$$

Table 4.1 Calculation of sec α and tan α

Region	R (pc)	sec α	tan α
NGC 6522	1000	1.01	0.13
	2000	1.00	0.07
	3000	1.00	0.04
	4000	1.00	0.03
	5000	1.00	0.03
	6000	1.00	0.02
	7000	1.00	0.02
NGC 2158	9000	-1.01	0.10
	10000	-1.01	0.09
	11000	-1.00	0.08
	12000	-1.00	0.07
	13000	-1.00	0.07
	14000	-1.00	0.06
	15000	-1.00	0.06
	16000	-1.00	0.06

First we make the assumption that there is no net radial expansion in the galaxy, i.e. $\langle V_R \rangle = 0$. We shall see soon that this is strongly supported by our data. Thus the term $\langle V_\varphi \rangle \langle V_R \rangle \cos\alpha$ in equation (4.9) is zero. Secondly, if we assume that the principal axes of the velocity ellipsoid are in the R, φ directions, the term $\langle V_R V_\varphi \rangle$ also vanishes. This is also a well founded assumption as the vertex deviation for old stars is small (Delhaye 1965). Thus:

$$2\sec\alpha\tan\alpha(\langle V_{obs}\rangle\langle V_\varphi\rangle - \langle V_{obs}V_\varphi\rangle) = -2\sigma_\varphi^2\tan^2\alpha \tag{4.10}$$

and

$$\sigma_R^2 = \sigma_{obs}^2\sec^2\alpha - \sigma_\varphi^2\tan^2\alpha \tag{4.11}$$

From the values of $\sec\alpha$ and $\tan\alpha$ in Table 4.1 we see that the azimuthal contribution to equation (4.11) is negligible. Also, as $|\sec\alpha|$ is almost 1 in both fields, we shall make the approximation:

$$\sigma_R \approx \sigma_{obs} \tag{4.12}$$

from now on for the NGC 2158 and Baade's Window fields.

As was mentioned previously, the distance errors will cause some uncertainty in the calculated velocity. In Appendix I a method is developed for calculating distance errors, taking into account photometric, reddening and metallicity errors. The mean result is an error of about 15% in distance from the sun. If we let

$$\delta r = \kappa r \tag{4.13}$$

where κ is the percentage error and r is the distance from the sun, then

$$R_1 = \sqrt{r^2 + R_o^2 - 2rR_o\cos\ell} \tag{4.14}$$

$$R_2 = \sqrt{[r(1+\kappa)]^2 + R_o^2 - 2r(1+\kappa)R_o\cos\ell} \tag{4.15}$$

$$\delta R = |R_1 - R_2| \tag{4.16}$$

If we then let $\rho = R + \delta R$ and recalculate $\langle V_R \rangle$ from equation (4.6) we have

$$\Delta_{\langle V_R \rangle} = |\langle V_R \rangle_\rho - \langle V_R \rangle_R| \tag{4.17}$$

The true error in the mean will be from a combination of this term and the sampling error defined by the velocity dispersion. As these are not correlated the true error in the mean is:

$$\varepsilon_{\langle V_R \rangle} = \sqrt{\Delta^2_{\langle V_R \rangle} + \frac{\sigma_R^2}{N-1}} \tag{4.18}$$

For σ_R the approximation in equation (4.12) ensures that the calculation of σ_R has no explicit dependence on R. Hence:

$$\varepsilon_{\sigma_R} = \frac{\sigma_R}{\sqrt{2N}} \tag{4.19}$$

4.1.2 Results

This section gives the main radial kinematic results for our program. Figure 4.2 shows a plot of $\langle V_R \rangle$ vs. R for our stars. We did not include stars which had measured abundances of $[Fe/H] < -1.0$ as it is unlikely that they are members of the old disk population. For the most part, the mean motion is very close to zero. The major exception to this is the very first bin which corresponds to a galactocentric distance of about 500 pc. As this is very close to the galactic center and the galactic rotation curve is not well known in that region, it is possible that the contribution from the rotation term in equation (4.6) is too large–hence $\langle V_R \rangle$ comes out too high. In order to get this value to near zero, the rotation term would also have to be near zero. This implies that there may be significant contamination of stars from the galactic bulge in the first bin. Otherwise it seems that the assumption of zero net expansion in the galactic disk is a good one.

Figure 4.3 shows the run of $\log(\sigma_R)$ with galactocentric distance R. The exponential decrease of σ_R with radius is quite interesting when viewed in the

Figure 4.2– The radial variation of $\langle V_R \rangle$ as measured in the NGC 6522 and NGC 2158 fields. The line at $\langle V_R \rangle = 0$ and the point at R_o are drawn for reference.

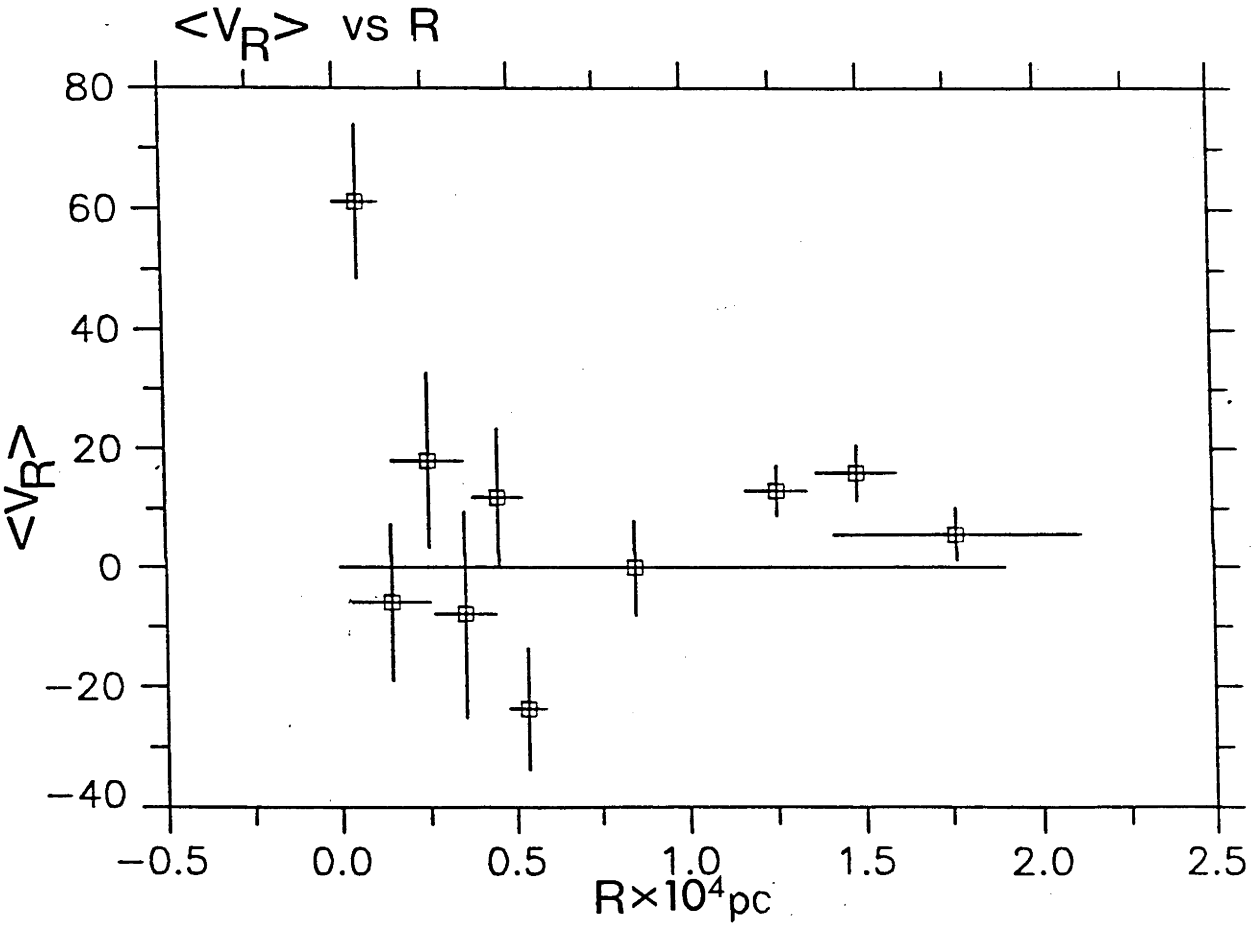

<V_R> vs R
80
60
40
20
0
−20
−40
<V_R>
−0.5
0.0
0.5
1.0
1.5
2.0
2.5
R×10^4pc

Figure 4.3– The radial variation of σ_R as measured in the NGC 6522 and NGC 2158 fields. The fitted line implies a radial scale-length of 4370 pc. The point at R_o is from Woolley (1965).

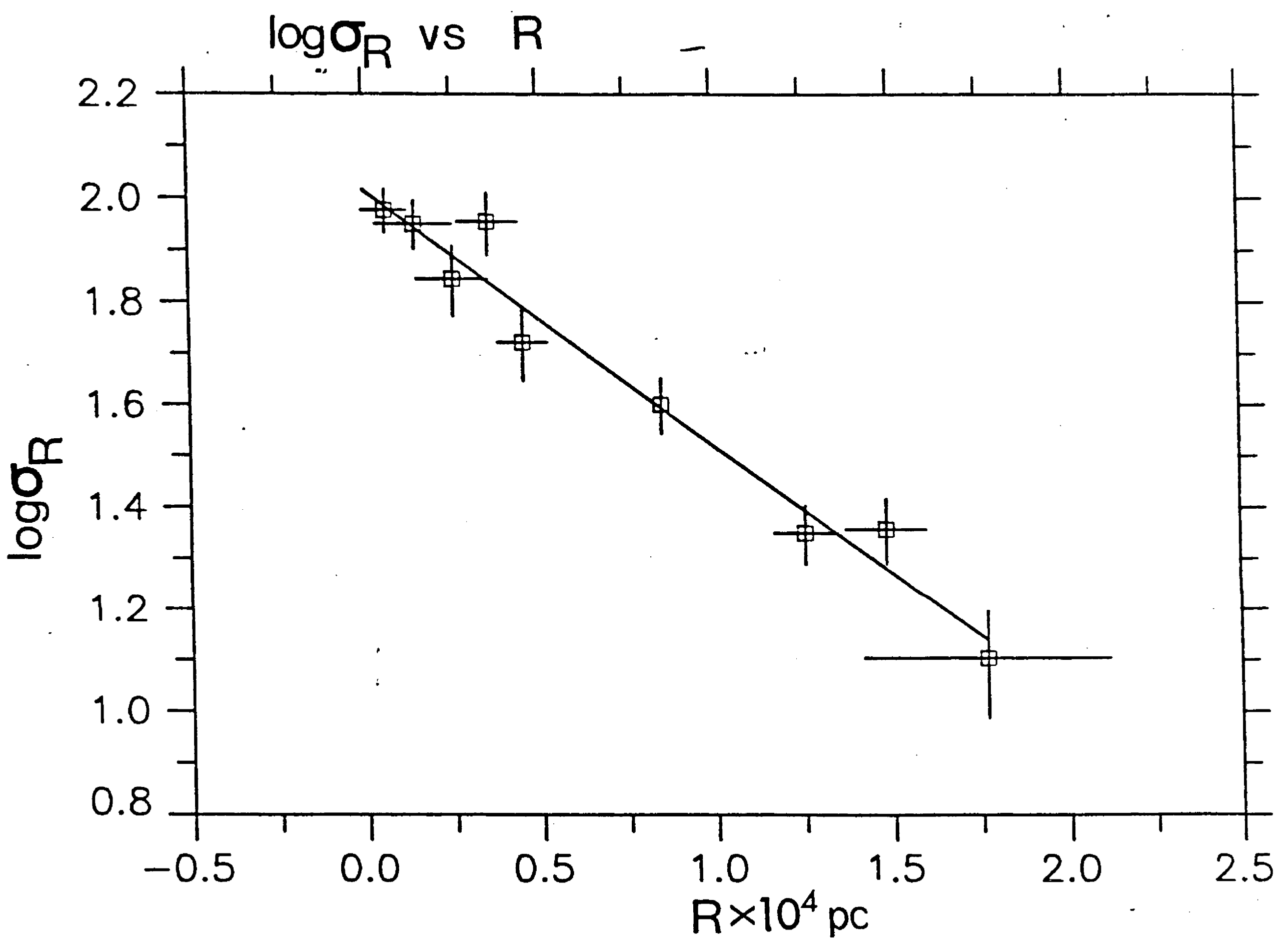

log σR vs R
2.2
2.0
1.8
1.6
1.4
1.2
1.0
0.8
log σR
−0.5
0.0
0.5
1.0
1.5
2.0
2.5
R×10^4 pc

context of the galaxy models of van der Kruit and Searle (1981). These were models of locally isothermal exponential disks of constant vertical scaleheight. In the first paper of the series, van der Kruit and Searle derived an equation for the radial variation of the vertical velocity dispersion:

$$\sigma_z^2 \propto e^{-R/h} \tag{4.20}$$

where h is the disk's radial scale-length. If we make the assumption that

$$\frac{\sigma_R}{\sigma_z} \approx const \tag{4.21}$$

then

$$\sigma_R^2 \propto e^{-R/h} \tag{4.22}$$

This allows a determination of the disk's radial scale-length from the slope of the fitted line in Figure 4.3. The fitted line implies a disk scale-length of $h = 4370$pc. This is close to other determinations, (see Bahcall & Soneira 1980 and references therein, van der Kruit 1986), and suggests that the assumption of uniform anisotropy [equation (4.21)] is approximately correct.

The run of σ_R is also interesting as it relates directly to Toomre's stability parameter Q which measures a disk's ability to stabilize itself against local axisymetric modes:

$$Q = \frac{\kappa\sigma_R}{3.36G\Sigma} \tag{4.23}$$

where Σ is the local surface density, σ_R is the local radial velocity dispersion, G is the gravitational constant and κ is the local epicyclic frequency. Σ can be estimated for an exponential disk from:

$$\Sigma = \Sigma_\odot \exp^{-(R-R_o)/h} \tag{4.24}$$

where we have taken $\Sigma_\odot$ to be 67 $M_\odot/\mathrm{pc}^2$ from Bahcall (1984). The radial velocity dispersion σ_R is given in Figure 4.3. We have calculated $\kappa(R)$ from the

Burton and Gordon (1978) rotation curve, using:

$$\kappa^2 = -4B(A - B) \tag{4.25}$$

where A and B are the local Oort constants. Figure 4.4 shows the resulting run of Q. We see that Q is everywhere greater than unity, so the disk is everywhere stable against local ring modes. According to Figure 4.4 this includes the regions outside the solar circle where the disk is quite cold. Some other interesting effects from this run of Q will be discussed further in Chapter 5.

4.2 The Tangential Kinematics

4.2.1 Basic Theory

The tangential components $\langle V_\varphi \rangle$ and σ_φ were measured in the remaining four regions. A fifth region near NGC 2324 at $\ell = 213$ was eventually excluded as we were unable to get adequate photometry in the region with which to calibrate our plates. The previously published photometry by Becker (1960) proved to have quite a large scatter ($\approx 0.1 - 0.15$ in magnitudes) which was clearly not adequate for our purposes.

As with the radial components, it is necessary to separate the contributions of the radial and tangential components to the observed velocity. Unlike the radial components, however, it is not possible to assume zero variation of α over a particular bin in these fields. Table 4.2 shows calculations of $\csc\alpha$ and $\cot\alpha$ for various galactocentric radii in the NGC 6712 field. The variation of α is therefore quite significant over a 1 kpc bin, and it is necessary to take it into account when calculating the mean rotation and tangential velocity dispersion.

If we solve equation 4.1 for V_φ we get:

$$V_\varphi = V_{obs} \csc\alpha + V_r \cot\alpha - S \csc\alpha \tag{4.26}$$

The average φ velocity is then straight forward:

$$\langle V_\varphi \rangle = \langle V_{obs} \csc\alpha \rangle + \langle V_R \cot\alpha \rangle - S\langle \csc\alpha \rangle \tag{4.27}$$

Figure 4.4– The radial variation of Toomre's stability criterion Q, calculated from equation (4.23).

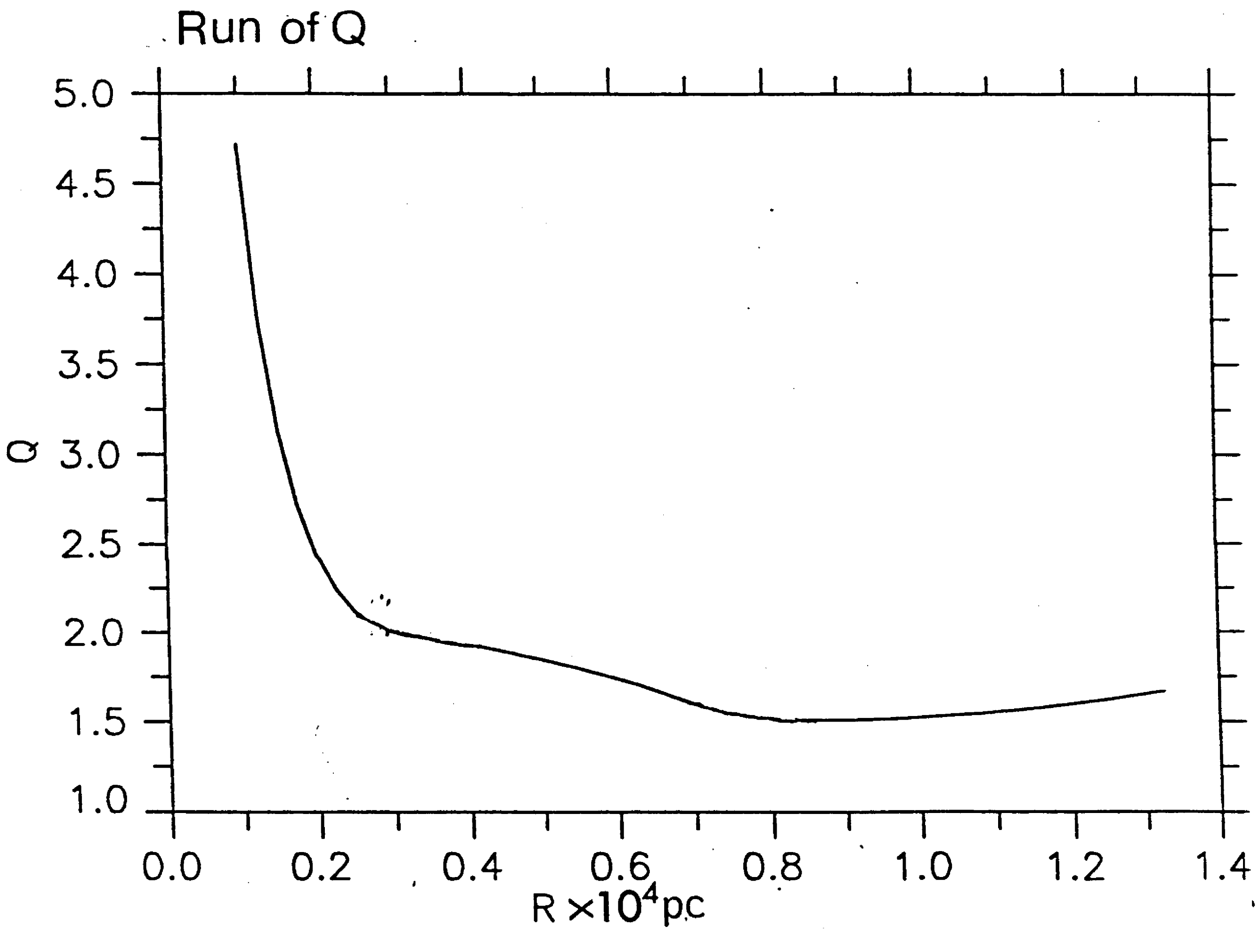

Run of Q
5.0
4.5
4.0
3.5
3.0
2.5
2.0
1.5
1.0
Q
0.0
0.2
0.4
0.6
0.8
1.0
1.2
1.4
R ×10⁴pc

Table 4.2 Calculation of csc α and cot α

Region	R (pc)	csc α	cot α
NGC 6712	3600	1.00	0.00
	4000	1.11	0.49
	5000	1.41	0.99
	6000	1.67	1.33

Now we let $x = V_{obs} \csc\alpha$, $y = V_R \cot\alpha$, and $z = \csc\alpha$, so

$$V_\varphi = x + y - Sz \tag{4.28}$$

Squaring and averaging gives:

$$\langle V_\varphi^2 \rangle = \langle x^2 \rangle + \langle y^2 \rangle + S^2 \langle z^2 \rangle + 2\langle xy \rangle - 2S\langle yz \rangle - 2S\langle xz \rangle; \tag{4.29}$$

averaging equation (4.28) and then squaring gives:

$$\langle V_\varphi \rangle^2 = \langle x \rangle^2 + \langle y \rangle^2 + S^2 \langle z \rangle^2 + 2\langle x \rangle\langle y \rangle - 2S\langle y \rangle\langle z \rangle - 2S\langle x \rangle\langle z \rangle. \tag{4.30}$$

Then, since $\sigma_\varphi = \langle V_\varphi^2 \rangle - \langle V_\varphi \rangle^2$:

$$\begin{aligned} \sigma_\varphi^2 &= \sigma_x^2 + \sigma_y^2 + S^2\sigma_z^2 + 2(\langle xy \rangle - \langle x \rangle\langle y \rangle) \\ &\quad -2S(\langle yz \rangle - \langle y \rangle\langle z \rangle) - 2S(\langle xz \rangle - \langle x \rangle\langle z \rangle) \end{aligned} \tag{4.30}$$

Hence in order to calculate the runs of $\langle V_\varphi \rangle$ and σ_φ it is necessary to include the contribution of the radial component of the velocity as well. Since we only observe the line of sight velocity, we do not know how much of a radial velocity component to subtract off for each star.

However, from the previous section, we know the run of σ_R and that to a very good approximation, $\langle V_R \rangle = 0$ over the whole galaxy. We can therefore make a Monte Carlo calculation. We assign to each star in the sample a random value of V_R from the following probability distribution function:

$$P(V_R) = \frac{1}{\sqrt{2\pi}\sigma_R} e^{-V_R^2/2\sigma_R^2} \tag{4.32}$$

where σ_R is the velocity dispersion calculated from equation (4.22) for the particular value of R of each star, and we take V_R in the range $-2.0\sigma_R \le V_R \le 2.0\sigma_R$ for stability of the calculation.

In order to take the distance errors into account, we assumed the following form for the distance errors δr when calculating $\csc\alpha$ and $\cot\alpha$:

$$\delta r = \kappa r \tag{4.33}$$

where again κ is some percentage error in distance. From Appendix I we adopt a value of 15% for κ. We then assign a random value of Δr from the distribution function:

$$P(\Delta r) = \frac{1}{\sqrt{2\pi}\delta r} e^{-(\Delta r)^2/2(\delta r)^2} \tag{4.34}$$

and then let

$$r' = r + \Delta r \tag{4.35}$$

Thus the galactocentric distance used to calculate $\csc\alpha$ and $\cot\alpha$ was

$$R' = \sqrt{r'^2 + R_o^2 - 2r'R_o \cos\ell} \tag{4.36}$$

For each subsample of observed velocities, 100 Monte Carlo calculations were made; each gave a value of $\langle V_\varphi \rangle$ and σ_φ These values were averaged to give the final result, and the dispersion about these means were taken to be the error which results from both the Monte Carlo method and distance errors. The final errors also take the sample size into account and were:

$$\varepsilon_{\langle V_\varphi \rangle} = \sqrt{\Delta^2_{\langle V_\varphi \rangle} + \frac{\sigma_\varphi^2}{N-1}} \tag{4.37}$$

and

$$\varepsilon_{\sigma_\varphi} = \sqrt{\Delta^2_{\sigma_\varphi} + \frac{\sigma_\varphi^2}{2N}} \tag{4.38}$$

where Δ is the error resulting from the Monte Carlo method and the distance errors.

4.2.2 Results

This section gives the main tangential kinematic results for our program. Figure 4.5 shows a plot of the calculated $\log(\sigma_\varphi)$ vs. R for one bin in Circinus, two bins in the NGC 5927 region, one bin in the NGC 6712 region and three bins in the NGC 2660 region. Stars with $[Fe/H] < -1$ were again deleted from the analysis as they are unlikely to be members of the old disk population. The point at 13 kpc is marked as such because its velocity dispersion is obviously

Figure 4.5– The radial variation of σ_φ. The fitted line implies a scale-length of 3360 pc. The point at R_o is from Woolley (1965). The point with the dashed lines was omitted from the fit.

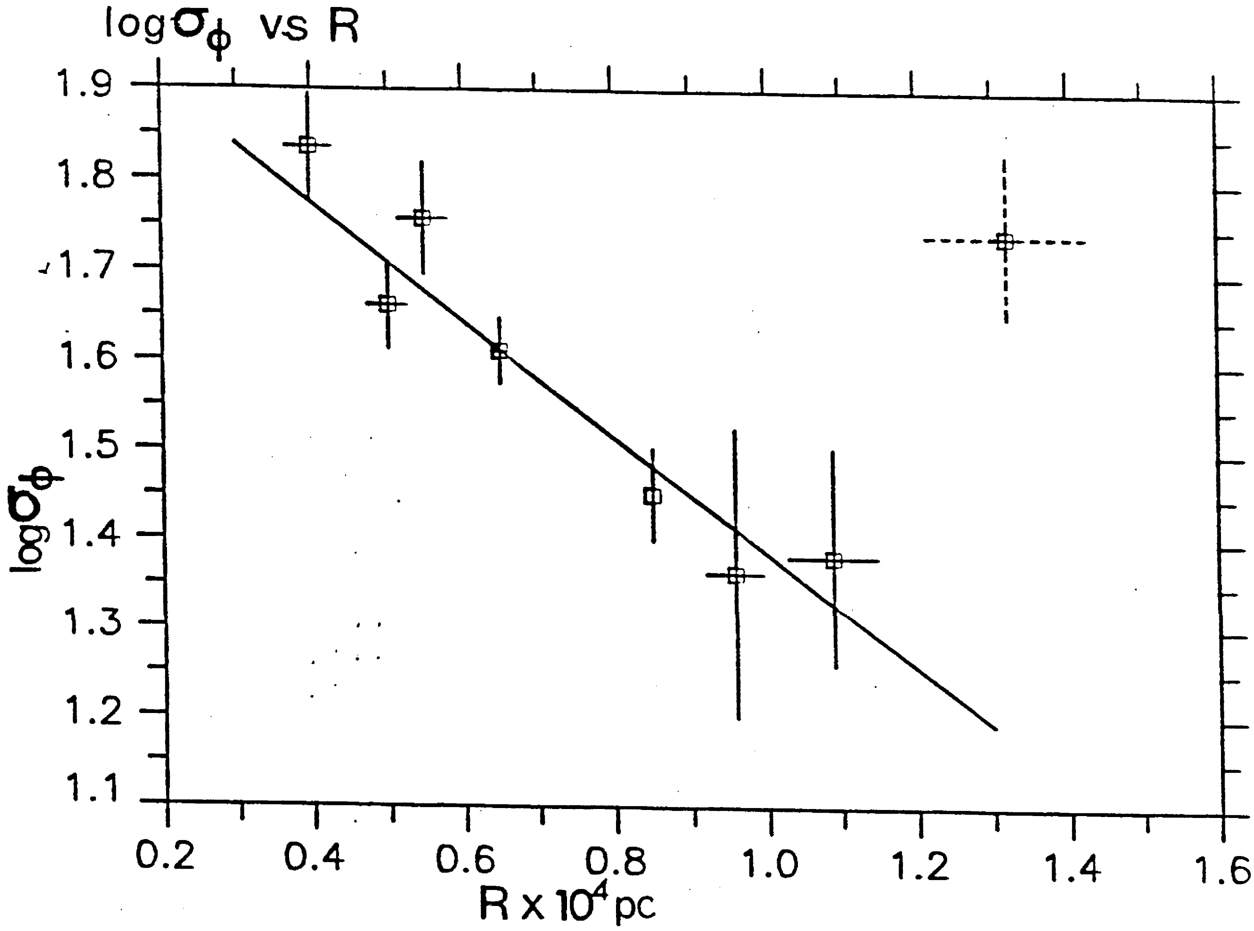

log σ_φ vs R
log σ_φ
1.9
1.8
1.7
1.6
1.5
1.4
1.3
1.2
1.1
0.2
0.4
0.6
0.8
1.0
1.2
1.4
1.6
R x 10^4 pc

discordant with the general trend defined by all of the other bins. As we shall see later, the point in this bin is consistent with the general trend in the mean rotation diagram and we are at a loss to explain why it does not behave in the velocity dispersion diagram. The fit in this diagram is also of the same form for the σ_R diagram, i.e.

$$\sigma_\varphi = \sigma_{o\varphi} \exp^{-R/2h_\varphi} \tag{4.39}$$

The slope of the fit corresponds to a value of $h_\varphi = 3360$ pc. The fact that this scale-length h_φ differs from the scale-length derived from σ_R (4370 pc) probably means that the galactic circular velocity curve is not precisely flat over the region for which we have data.

Finally, to compare our mean rotation values with the circular velocity curve, it was necessary to adjust our data for the expected asymmetric drift. The asymmetric drift is the lag in the mean φ-velocity of a group of stars behind the circular velocity at a particular galactocentric distance. It is a result of the contribution of pressure support to the radial equilibrium of a sample of stars, i.e. if there is more pressure support, then less mean rotation is needed to support the sample.

The asymmetric drift is calculated from the zeroth and first moments of the collisionless Boltzmann equation. The standard result of this calculation is:

$$\frac{1}{R}\frac{\partial}{\partial R}(\rho R \sigma_R^2) + \frac{\rho}{R}(\Theta^2 - \langle V_\varphi \rangle^2 - \sigma_\varphi^2) + \frac{\partial}{\partial z}(\rho \sigma_{Rz}^2) = 0 \tag{4.40}$$

(Oort 1965), where ρ, $\langle V_\varphi \rangle$ and σ are the density, mean velocity, velocity dispersion for the particular sample of stars and Θ is the circular velocity. If we assume that the velocity ellipsoid axes are also aligned parallel to the R, φ, z axes then only the diagonal elements of the velocity dispersion tensor are non-zero. Thus rearranging equation (4.40) we get:

$$\Theta^2 - \langle V_\varphi \rangle^2 = -\sigma_R^2 \left(1 - \frac{\sigma_\varphi^2}{\sigma_R^2} + \frac{\partial \ln(\rho \sigma_R^2)}{\partial \ln R}\right) \tag{4.41}$$

For small $\Theta - \langle V_\varphi \rangle$, $\Theta + \langle V_\varphi \rangle \approx 2\Theta$, so:

$$\Theta - \langle V_\varphi \rangle \approx \frac{-\sigma_R^2}{2\Theta}\left(1 - \frac{\sigma_\varphi^2}{\sigma_R^2} + \frac{\partial \ln(\rho\sigma_R^2)}{\partial \ln R}\right) \tag{4.42}$$

Note that $\Theta - \langle V_\varphi \rangle$ is the definition of asymmetric drift. For $\Theta - \langle V_\varphi \rangle$ not small,

$$\Theta - \langle V_\varphi \rangle = \Theta - \sigma_R \sqrt{1 - \frac{\sigma_\varphi^2}{\sigma_R^2} + \frac{\partial \ln(\rho\sigma_R^2)}{\partial \ln R} + \frac{\Theta^2}{\sigma_R^2}} \tag{4.43}$$

Using this definition, we then substitute for the relations found earlier on in this chapter for the radial and tangential velocity dispersions in equations (4.22) and (4.39). We also assume an exponential disk (Freeman 1970) of the form:

$$\rho = \rho_o \exp^{-R/h} \tag{4.44}$$

This gives:

$$\Theta - \langle V_\varphi \rangle = \Theta - \sqrt{-\sigma_{o\varphi}^2 e^{-R/h_\varphi} + \sigma_{oR}^2 e^{-R/h_R}\left(1 - \frac{R}{h} - \frac{R}{h_R}\right) + \Theta^2} \tag{4.45}$$

Figure 4.6 shows a plot of asymmetric drift versus R. The normalization constants $\sigma_{o\varphi}, \sigma_{oR}$ were those found from our linear fits to the $\sigma - R$ relations in Figures 4.3 and 4.5. The scale–lengths h_R and h_φ were also taken from those figures. The density scale–length, h has been taken to be the same as h_R, which from section 4.1.2 is consistent with the assumption of uniform anisotropy. Figure 4.6 shows that the asymmetric drift is nowhere larger than about 20 km sec^{-1}, even in the inner parts where the velocity dispersion is quite high. The circular velocity, Θ was calculated from the Burton & Gordon (1978) rotation curve.

Figure 4.7 shows a plot of $\langle V_\varphi \rangle$ as calculated from equation (4.27) and corrected for asymmetric drift from equation (4.43). As we mentioned previously, we expect that the sum of the mean rotation and asymmetric drift of the old population will equal the circular velocity as defined by the much younger CO clouds. This figure shows that this is in fact the case for the old disk stars in

Figure 4.6– The expected asymmetric drift vs. R, calculated from equation (4.45).

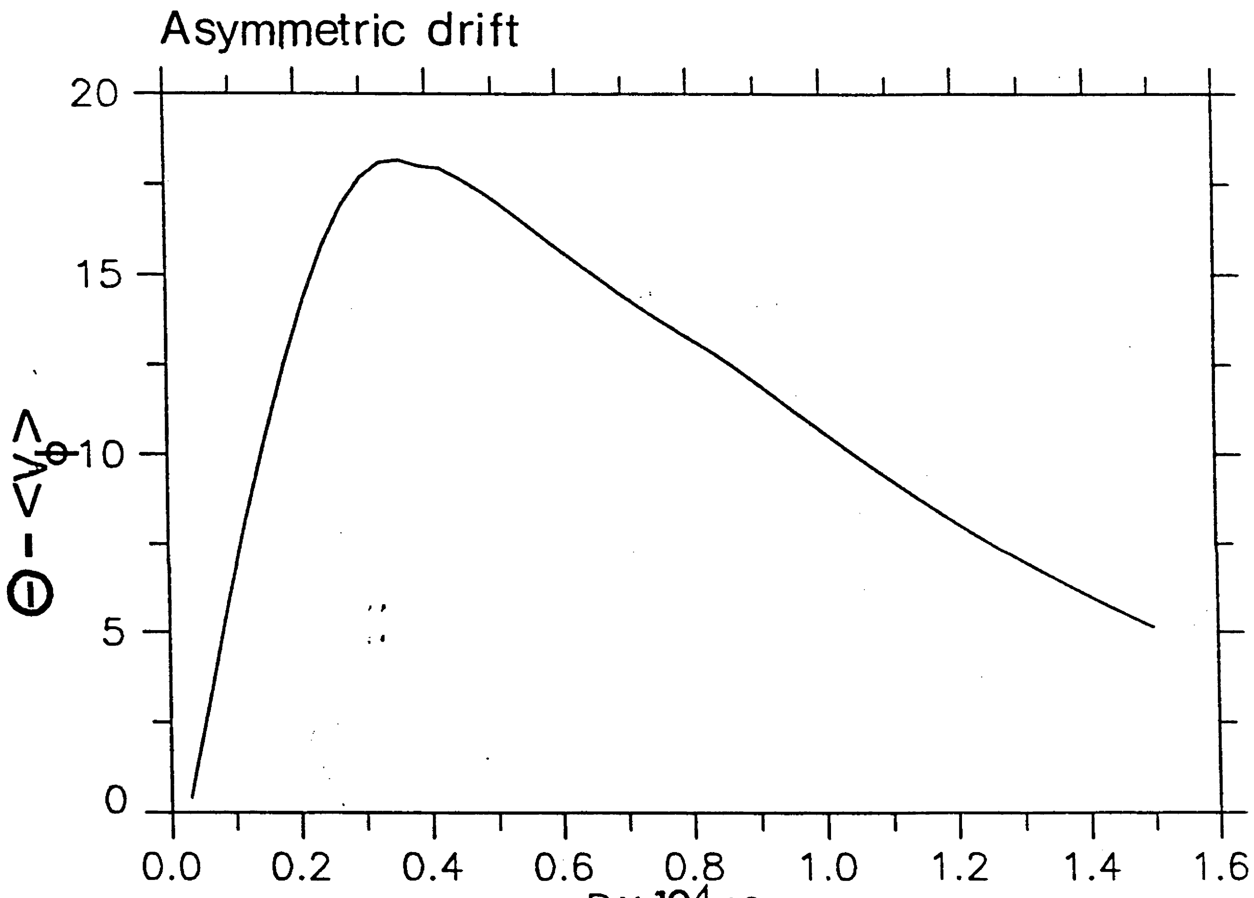

Asymmetric drift
20
15
10
5
0
$\Theta - \langle v_\phi \rangle$
0.0
0.2
0.4
0.6
0.8
1.0
1.2
1.4
1.6
$R \times 10^4$ pc

Figure 4.7– The radial variation of $\langle V_\varphi \rangle$, corrected for asymmetric dirft. The curve is the Burton & Gordon (1978) rotation curve. The point at R_o is included for reference.

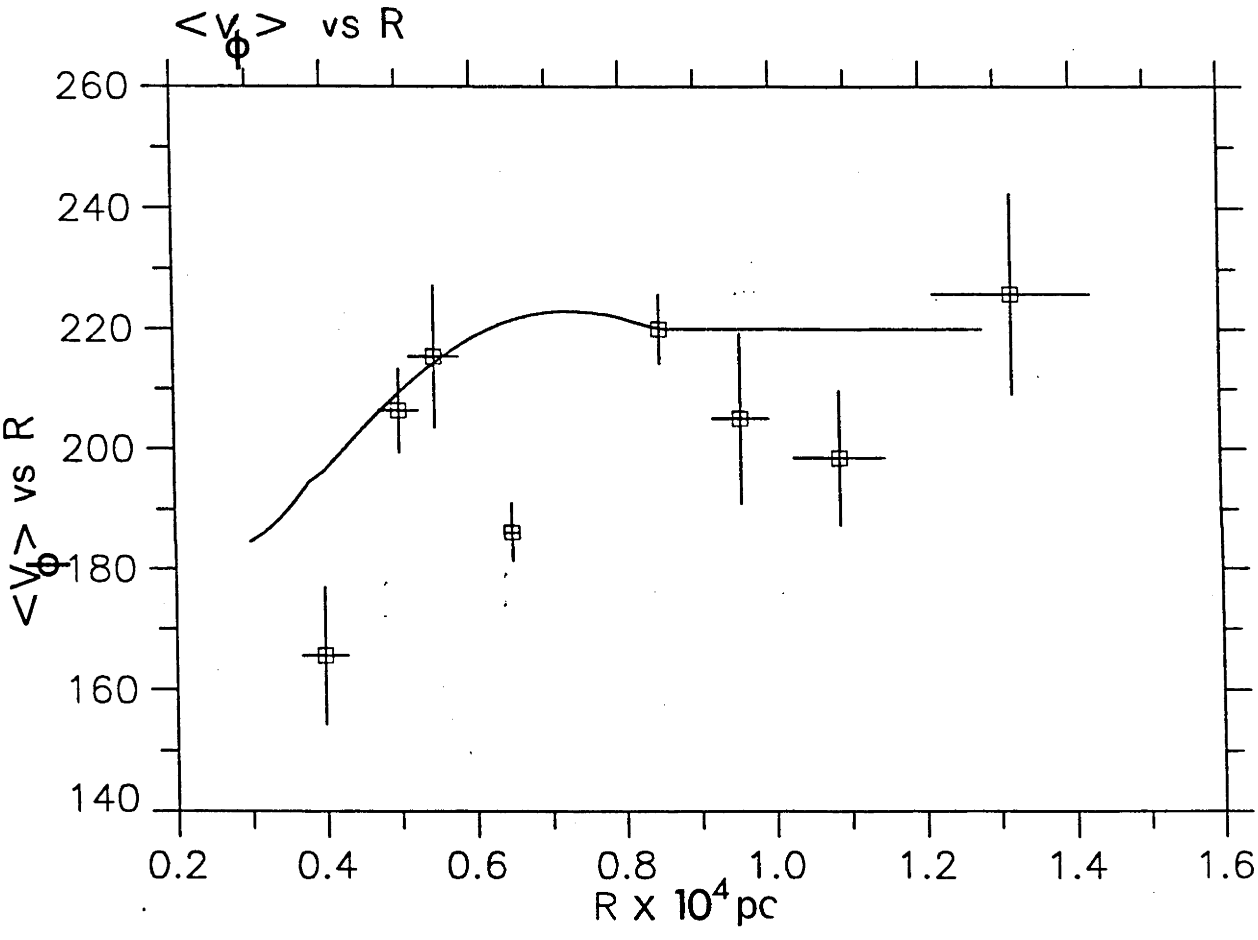

<v_φ> vs R
260
240
220
200
180
160
140
<V_φ> vs R
0.2
0.4
0.6
0.8
1.0
1.2
1.4
1.6
R x 10^4 pc

our sample. A further discussion of these kinematic results will be presented in chapter 5.

4.3 Abundance Results

Figure 4.8 shows a plot of $[Fe/H]$, as derived from the equivalent width measurements, versus galactocentric distance. The distances used were calculated as described in chapter 2 with the true measured metallicity included. A further iteration to estimate a new value of reddening from equations (2.1) and (2.2) and hence derive a revised intrinsic color and metallicity gives a negligible change in reddening.

Figure 4.8 indicates that there is no significant radial gradient of abundance amongst the old disk stars. This conclusion differs from those of many authors (see Janes 1979 for references) who have found a radial gradient of typically -0.05 dex/kpc. These studies, however, were done mostly on young and intermediate age objects and their conclusions may not hold true for the old disk population. In a preliminary report of a study similar to our own, Yoss and Neese (1986) have found a radial abundance gradient of about -0.05 dex/kpc. Their study, however, included the full range of disk giants from G0 to K5, rather than restricting their sample to the older K2–K5 stars as we have. Thus the two sets of data may not be entirely comparable.

As was mentioned in the previous chapter, the calculation of DDO colors was used to backup the results of our metallicity analysis. Metallicities are calculated by comparing the dereddened measured value of the DDO color $C_o(41-42)$ with a standard table compiled by Janes (1975). The value δCN is defined as:

$$\delta CN = C(41-42)_{meas} - C(41-42)_{std} \tag{4.46}$$

As is suggested by the name, δCN is an index which is sensitive to the strength of the CN band. As the strength of the CN band is also a function of stellar age and mass due to the predominance of the CNO cycle in a star's early history,

Figure 4.8– The radial variation of $[Fe/H]$. The fitted lines shows no significant slope.

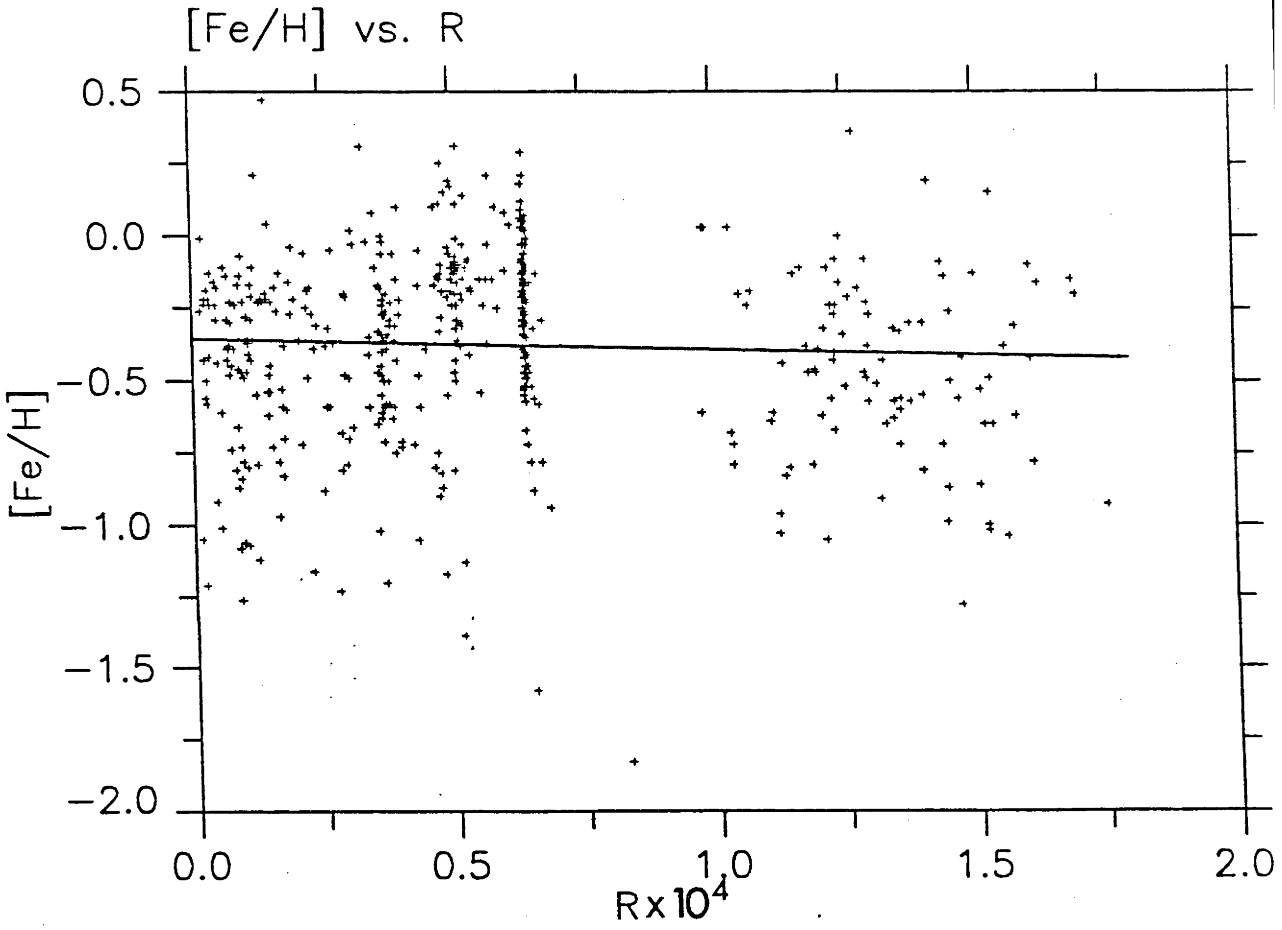
[Fe/H] vs. R
0.5
0.0
−0.5
−1.0
−1.5
−2.0
[Fe/H]
0.0
0.5
1.0
1.5
2.0
R x 10^4

this analysis will not be entirely analogous to that of the equivalent width measurements. However it is known from Janes (1979) and Hartkopf and Yoss (1982) that there is a good correlation between $[Fe/H]$ and δCN, at least for stars with $[Fe/H] \geq -0.7$.

The relationship used to calculate [Fe/H] from δCN was that found by Janes (1979):

$$\left[\frac{Fe}{H}\right] = 4.5\delta CN - 0.2 \tag{4.47}$$

As our stars were all very red, the region of C(41-42) was the location in the spectra where we had the highest photon noise. Typical errors in C(41-42) were 0.05–0.06 magnitudes. There was also an error of typically 0.05 magnitudes in the transformation of the C(41-42) color to a true C(41-42) as described in chapter 3. Assuming that Janes' intrinsic colors are error–free (which they presumably are not) then the error in δCN is 0.078 magnitudes. This corresponds to an error in $[Fe/H]_{DDO}$ of 0.35 dex. Hence in a plot of the DDO metallicities versus the metallicities found from our equivalent width measurements, we would expect an rms deviation of about 0.43 dex from a 45° line.

Figure 4.9 is a plot of $[Fe/H]_{DDO}$ vs. $[Fe/H]_{W_\lambda}$. The measured deviation from a 45° line is approximately 0.47 dex, in good agreement with the expected deviation of 0.43 dex. This plot serves to show that there does not appear to be any significant calibration error in the values of [Fe/H] calculated from our equivalent width measurements. Hence our equivalent width calibration appears to be correct to within the 0.22 dex error quoted in chapter 3. Given this information it seems clear from Figure 4.9 that the metallicity gradient seen in the disk with young and intermediate age objects does not exist in the old disk. The implications of this result will be discussed in chapter 5.

Figure 4.9– $[Fe/H]_{DDO}$ vs $[Fe/H]_{W_\lambda}$. The dispersion about a 45 degree line is about 0.47.

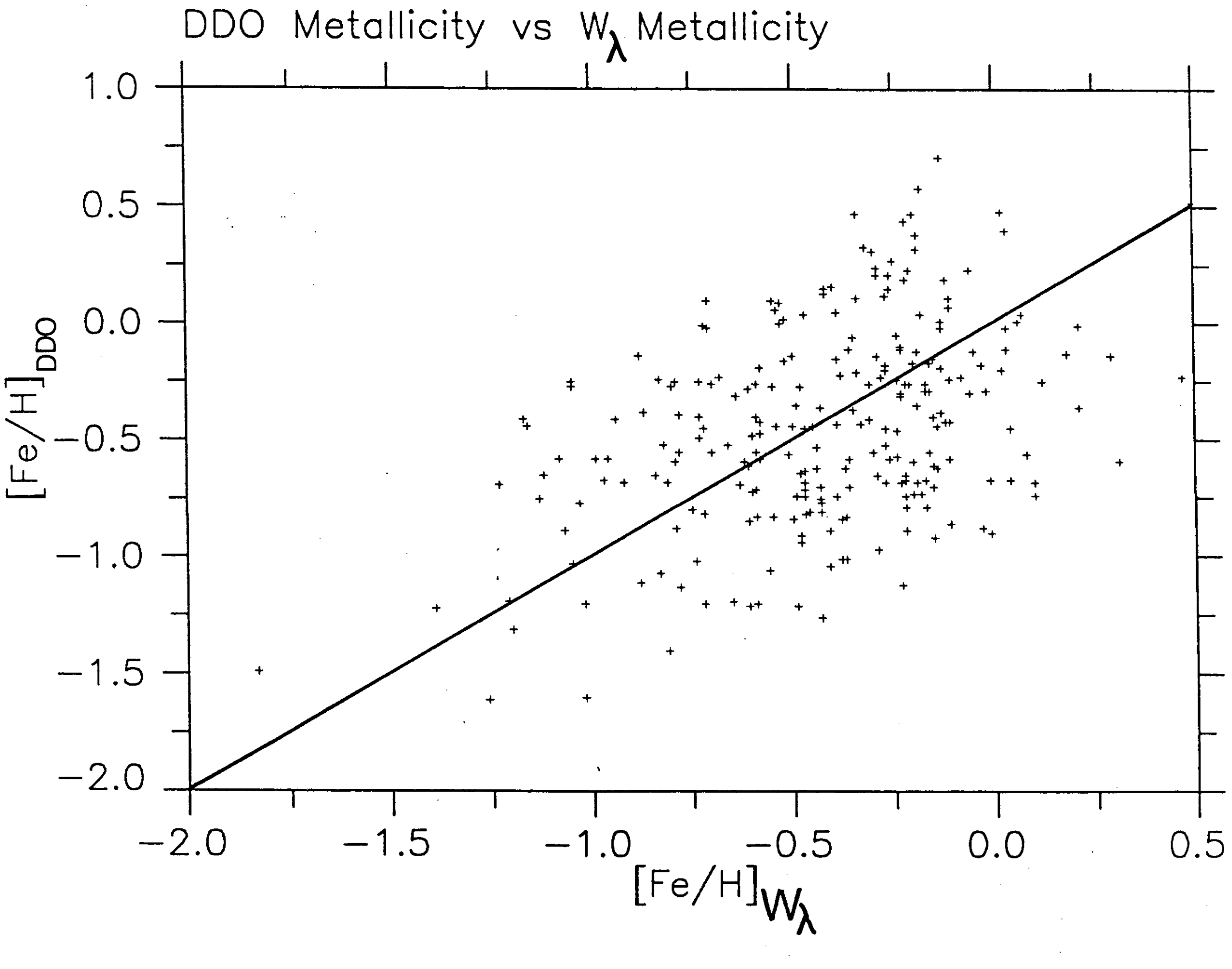
DDO Metallicity vs Wλ Metallicity
1.0
0.5
0.0
−0.5
−1.0
−1.5
−2.0
[Fe/H]DDO
−2.0
−1.5
−1.0
−0.5
0.0
0.5
[Fe/H]Wλ

CHAPTER FIVE

Discussion of Results

Introduction

In this chapter we would like to discuss some of the results of this project and what these results mean in terms of the history of the galactic disk and its present state. First, however we give a brief description of why we believe our sample contains mainly old stars. In the following section we discuss various determinations of the disk's radial scale-length and the differences between them. In the next two sections we discuss the implications of the hot disk which we found from our observations and we address the question of the origin of the disk's random motions. Next we will look at the galactic rotation curve and its relationship to the derived runs of radial and tangential velocity dispersion. Finally we shall look at reasons for why there is no apparent metallicity gradient in the old disk.

5.1 The Ages of the Stars in the Sample

Now that we are about to make some conclusions about the structure and formation of the old disk, we need to know that the stars in our sample are in fact old. There are two direct arguments that indicate that our sample does include primarily stars of the old disk population.

The first argument goes back to the selection criterion for the regions presented in Chapter 1. That is, the regions we chose had a value of galactic latitude $|b| < 5°$. However none of them had $|b| < 2°$. This meant that the stars we looked at were at least 150 pc above the plane. As the scale-height of young objects is typically 90–100 pc and that for older objects is $\approx$ 250–350 pc (see Bahcall and Soneira 1980 and references therein), most of the younger K giants would be excluded from our sample.

Our second argument involves the relationship between kinematic properties and metallicity. Figure 5.1 shows a diagram from Wilson (1986). This diagram is a plot of metallicity versus velocity for a large number of stars within 400 pc from the sun in the latitude range ($\pm 3°$) which Wilson observed and for which he measured abundances and velocities. This figure shows a clearly unmixed kinematical distribution for $[Fe/H] > -0.2$, corresponding to the local young ($\approx 5 \times 10^8 y$) 'moving group' stars which Wilson was studying. At lower metallicities the structure in this diagram drops out and the mean velocity and velocity dispersion correspond to the standard old disk values for $[Fe/H] < -0.2$. Figures 5.2a,b,c show the same plots for all of the stars by regions in our sample for which we have derived abundances. In these plots we see no structure in the velocity–abundance plane. Hence we conclude that our sample contains virtually all old disk stars.

5.2 The Disk's Radial Scale-length

There have been several recent determinations of the radial density scale-length in the old disk of the Milky Way. The first by de Vaucouleurs and Pence (1978) was done by estimating the surface brightness of the disk from star counts. They then assumed the canonical value for central surface brightness of disk galaxies from Freeman (1970): $\mu_o = 21.65$ B mag/$\square$". Their data gave a value of 3770 ± 450 pc. (corrected to $R_o = 8500$ pc).

Van der Kruit and Searle (1982) estimated the local surface brightness from plausible values of the disk's vertical scale-height and the mass to light ratio of the old disk. The value they derived for this surface brightness was in good quantitative agreement with the findings of de Vaucouleurs and Pence (1978). For the central surface brightness, however, van der Kruit and Searle estimated a value from those obtained for old disks of other

Figure 5.1– A plot of $[Fe/H]$ vs radial velocity for disk stars from Wilson (1986). The clump at $[Fe/H] > -0.2$ shows the kinematics of a young unmixed 'moving group'. For $[Fe/H] < -0.2$ the diagram shows no structure. This represents typical old disk properties.

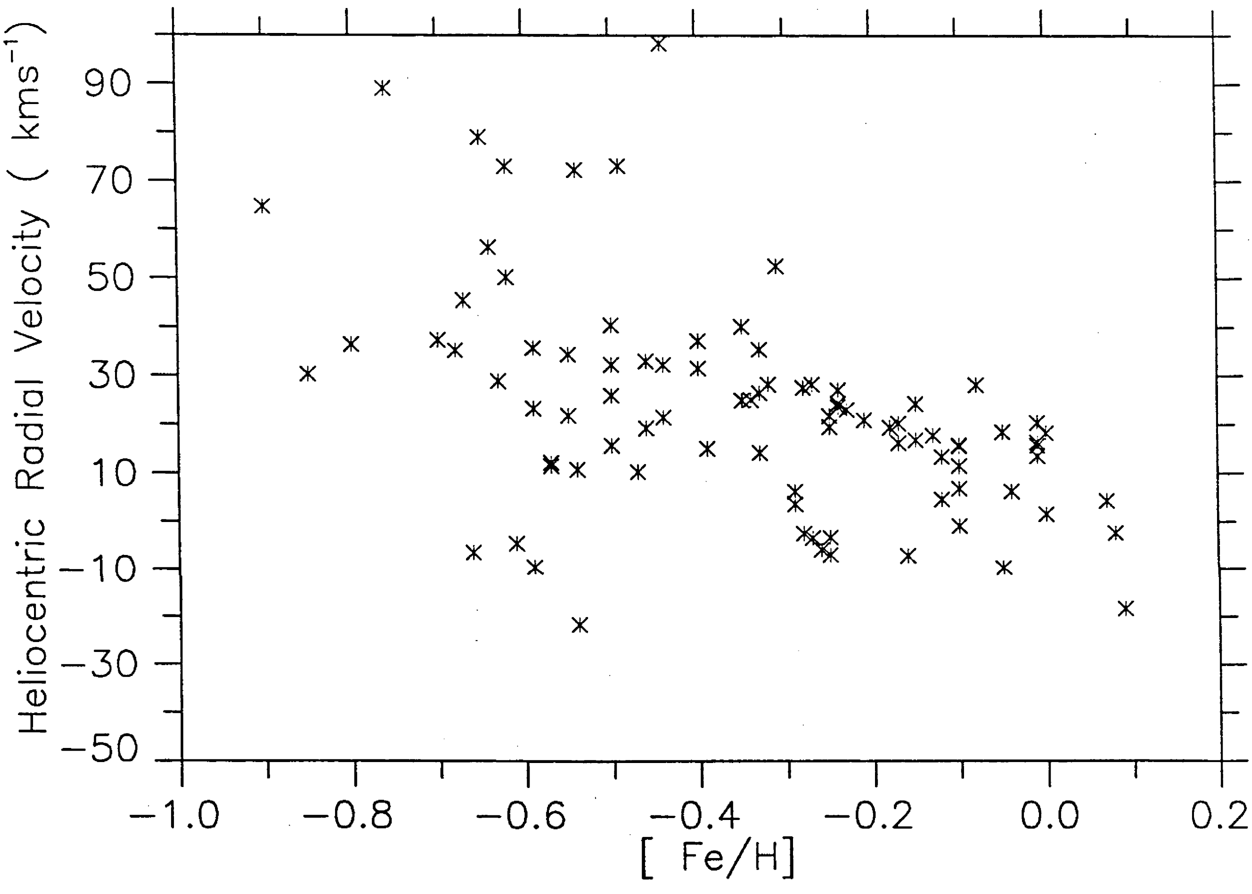
Heliocentric Radial Velocity (kms^{-1})
90
70
50
30
10
−10
−30
−50
−1.0
−0.8
−0.6
−0.4
−0.2
0.0
0.2
[Fe/H]

Figures 5.2– Plots of $[Fe/H]$ vs radial velocity for disk stars from three regions in our sample: (a) NGC 6522, (b) NGC 5927 and (c) NGC 2158. There is no visible structure in any of the diagrams.

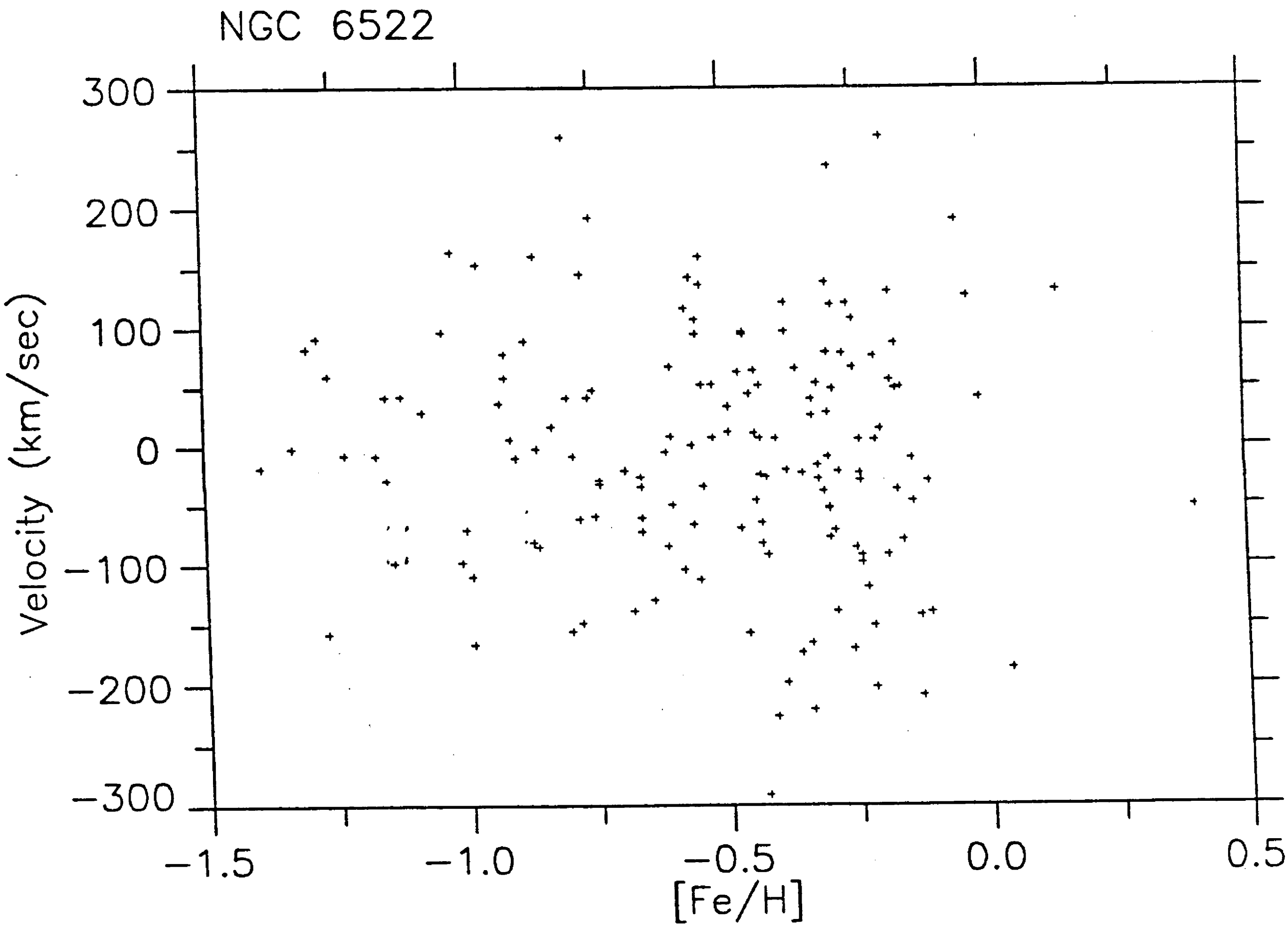
NGC 6522
300
200
100
0
−100
−200
−300
Velocity (km/sec)
−1.5
−1.0
−0.5
0.0
0.5
[Fe/H]

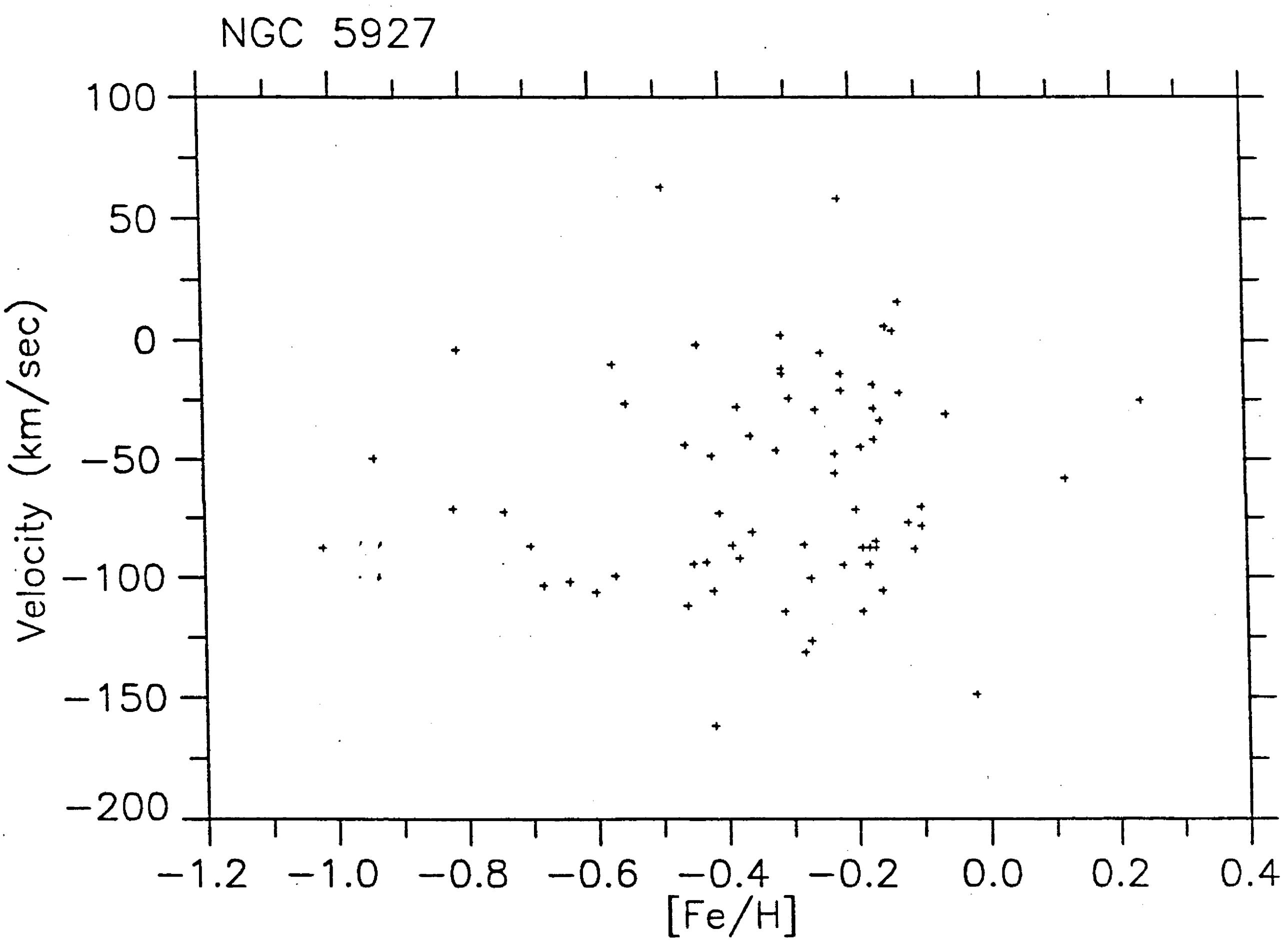
NGC 5927
100
50
0
−50
−100
−150
−200
Velocity (km/sec)
−1.2
−1.0
−0.8
−0.6
−0.4
−0.2
0.0
0.2
0.4
[Fe/H]

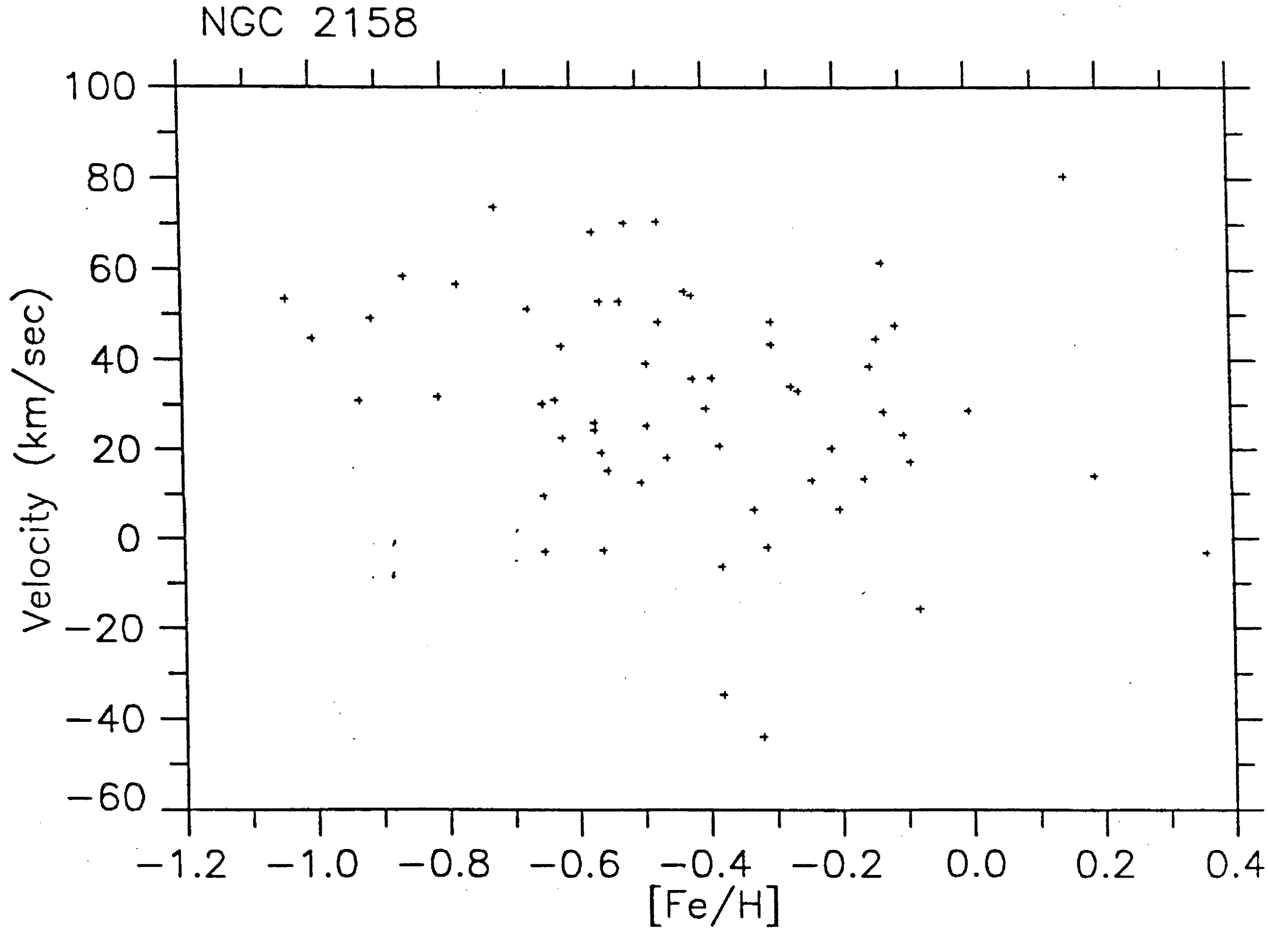
NGC 2158
100
80
60
40
20
0
−20
−40
−60
Velocity (km/sec)
−1.2
−1.0
−0.8
−0.6
−0.4
−0.2
0.0
0.2
0.4
[Fe/H]

Sb galaxies which they had studied: this value was $\mu_o \approx 22.4$ B mag/$\square$". Thus they derived a value of $h \approx 5000$ pc. This lower value of the central surface brightness is intended to exclude the contribution of the younger population I objects.

Recently van der Kruit (1986) has derived the ratio h/h_z using the Pioneer 10 background starlight experiment data, where h_z is the vertical scale-height. Only the ratio of h/h_z could be measured as the analysis had to be restricted to galactic latitudes $\geq 20^o$. He derived a ratio of $h/h_z = 17 \pm 3$ which, for $h_z = 325$ pc, leads to a disk scale-length of about 5500 ± 1000 pc. While this is in good agreement with the result of van der Kruit and Searle (1982) it may be that the assumed value of $h_z = 325$ pc is not the best one. This scale-height was measured for old disk dwarfs (Bahcall & Soneira 1980). However, the old disk giants would dominate the background light in the Pioneer data. The h_z value for disk giants is probably less than for dwarfs. For example, if we take the value of h_z for disk giants originally advocated by Bahcall and Soneira (1980) of 250 pc for disk giants (from Oort 1960), then the ratio of h/h_z leads to a value of 4250 pc. With this value, van der Kruit's measure of the local surface brightness from the Pioneer data ($\mu = 23.8$ B mag/$\square$") extrapolates to a central surface brightness of 21.7 B mag/$\square$"!

The value of $h = 4370$ pc which we found from our radial velocity dispersion information is consistent with the revised van der Kruit value just mentioned. The assumption which went into this determination was that of a uniform anisotropy in the velocity dispersion of the galactic disk, i.e.

$$\frac{\sigma_R}{\sigma_z} = const \qquad (5.1)$$

throughout. Given the values of h which are acceptable within the quoted errors it is safe to say that our kinematically determined value is not really in significant disagreement with any of the abovementioned determinations. The fact that our result is so close to two determinations which were not based on the assumption in equation (5.1) gives us confidence that the assumption of uniform anisotropy is a good one.

5.3 The Run of Q

It is quite obvious from Figure 4.4 that the inner parts of the galactic disk are indeed quite hot. The value of Q is everywhere ≥ 1.3. This is comforting as a situation with $Q < 1$ could not survive and it gives us confidence that our values of Q are indeed realistic, especially given our assumed run of surface density and rotation curve.

It seems that the disk's own velocity dispersion is large enough to prevent bi-symetric modes from forming. Athanassoula and Sellwood (1986) have recently shown that a Kuz'min disk whose value of Q rises to around 2 near the center would be stable against these global bar modes. Our derived run of Q rises from around 1.3 near the sun to about 2.3 at a distance which is roughly half a disk scale-length. Thus the apparent absence of a large bar in the old disk of the Milky Way is consistent with the increase in dispersion towards the central regions. This shows that it is not necessary to invoke a massive halo to provide the support needed to suppress bar modes. This is in agreement with the work of Carignan (1983), for example, which showed that these halos do exist in spiral systems but that their densities are probably too low for them to be dynamically important except in the outer regions.

It is interesting to look at the run of Q produced by N-body models of Sellwood and Carlberg (1984), hereafter SC. In these models they tried to describe the evolution of disk dynamics through heating by repeated encounters with transient spiral structures and cooling by accretion of gas from the galactic halo. They found that their models evolved with a value of Q which was almost constant with radius. This is clearly different from our results, and we should try to understand the difference.

It may be that SC's surface density distribution $\Sigma(R)$ and $V(R)$ are too different from those of the Milky Way to allow a direct comparison. They used:

$$V(R) \sim \frac{R}{a}\left(1+\frac{2R}{a}\right)^{-7/8}\left(1+\frac{R}{5a}\right)^{-5/8} \tag{5.2}$$

$$\Sigma(R) \sim \left(1+\frac{20R}{a}\right)^{-3/4}\left(1+\frac{R}{5a}\right)^{-2} \tag{5.3}$$

where R is galactocentric distance and a is the disk scale-length. If Q is constant, then we can predict a run of σ_R^2. If we only consider the shape of the curve then:

$$\sigma_R^2 \propto \frac{\Sigma^2}{\kappa^2} \tag{5.4}$$

where Σ is again the surface density and κ is the local epicyclic frequency, as defined in equation (4.25). This leads to:

$$\kappa^2 = 2\left(\frac{V}{R}\frac{dV}{dR}+\frac{V^2}{R^2}\right) \tag{5.5}$$

Taking the first derivative of equation (5.2), using equations (5.3) and (5.5) we get:

$$\sigma_R^2 \propto \frac{\left(1+\frac{2R}{a}\right)^{\frac{7}{4}}}{\left(1+\frac{20R}{a}\right)^{\frac{3}{2}}\left(1+\frac{R}{5a}\right)^{\frac{7}{4}}\left\{\left(1+\frac{R}{5a}\right)-R\left(1+\frac{R}{5a}\right)\left(1+\frac{R}{2a}\right)^{-1}-R\right\}} \tag{5.6}$$

whereas from equation (4.20) we expect from our data:

$$\sigma_R^2 \propto \exp^{-R/h_R} \tag{5.7}$$

First let us directly compare the density distribution of equation (5.3) with that of a standard exponential disk. Figure 5.3 shows a semi-log plot of an exponential disk density function and the surface density used by SC: the

Figure 5.3– A semi-log plot of the surface density used in Sellwood & Carlberg's (1984) models from equation 5.3 (circles), as well as the surface density profile for an exponential disk (squares).

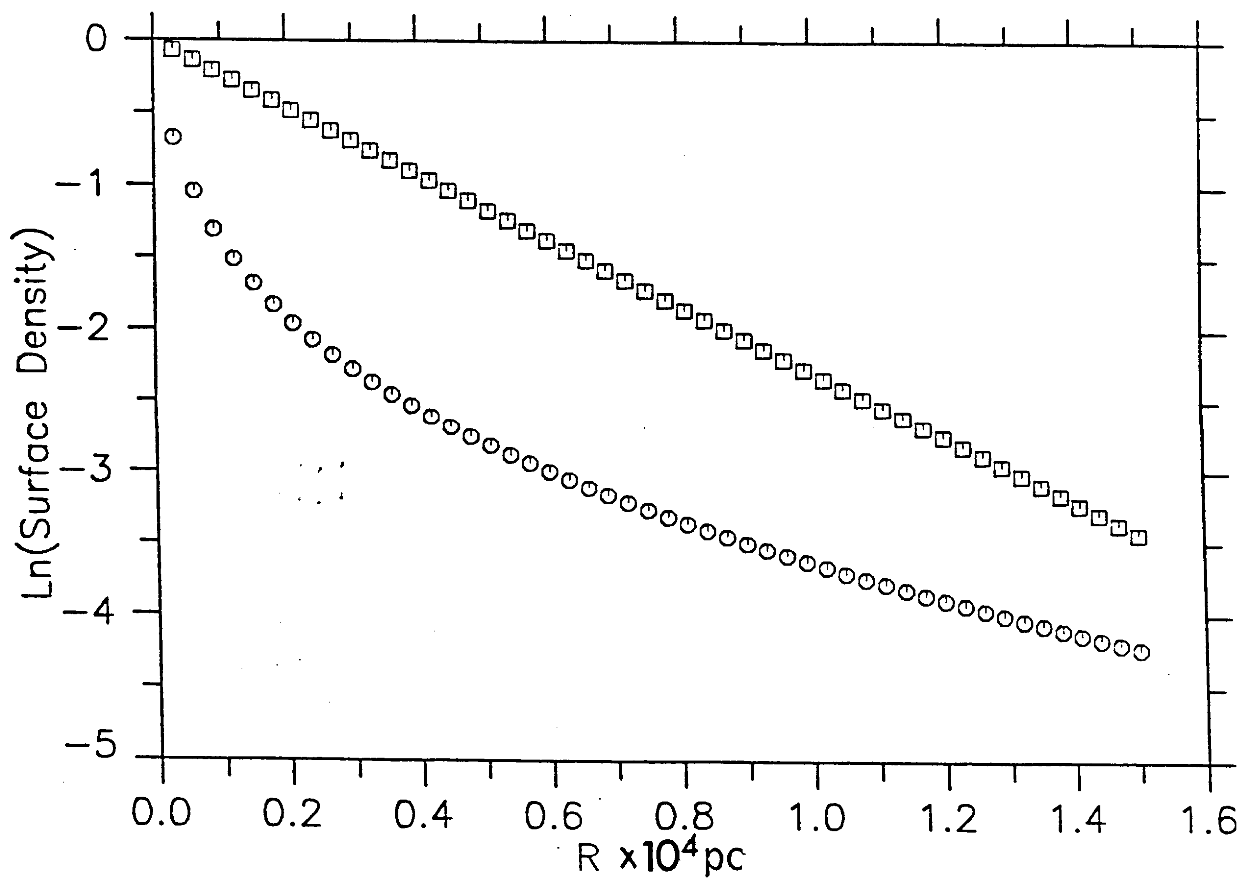

0
−1
−2
−3
−4
−5
Ln(Surface Density)
0.0
0.2
0.4
0.6
0.8
1.0
1.2
1.4
1.6
R x10^4 pc

two distributions are clearly different. The scale-lengths of the curves are approximately equal at about $R = 4000$ pc so we let $a = h_R$ and compare the shapes of the velocity dispersion curves. Figure 5.4 shows a plot of equations (5.6) and (5.7) as a function of the ratio R/h_R. The crosses are the predictions of the exponential van der Kruit & Searle (1981) model and the circles are the predictions of the model by SC. Again these curves are not at all similar. As well as the obvious dissimilarities in the sense of curvature, the SC model also shows a singularity at $R/h_R \approx 0.9$. We suggest that the underlying properties of the SC model are different enough from those of the Milky Way that their conclusion about the evolution of Q may not be applicable to the Milky Way.

Although evolution at constant Q is intuitively attractive, we can show that a constant value of Q for an exponential disk with our observed exponential run of σ_R is inconsistent with a flat rotation curve. Starting with:

$$\Sigma = \Sigma_{\odot} \exp^{-(R-R_o)/h} \tag{5.8}$$

and our observed exponential run of σ_R, we can solve equation (4.23) for κ^2 and hence the rotation curve. Combining equations (5.5), (5.7) and (5.8) we get:

$$\frac{y}{x} + \frac{1}{2}\frac{dy}{dx} = \beta^2 x e^{-x} \tag{5.9}$$

where $x = R/h$, $y = V^2$ and $\beta^2 = 11.29 Q^2 G^2 \Sigma_{\odot}^2 h^2 \exp^{2R_o/h} / \sigma_{oR}^2$. This equation has the solution:

$$V^2 = \frac{4V_{\odot}^2 + 76\beta^2 e^{-2}}{x^2} - \frac{12\beta^2 e^{-x}}{x^2} - \frac{12\beta^2 e^{-x}}{x} - 6\beta^2 e^{-x} - 2\beta^2 x e^{-x} \tag{5.10}$$

Note that this is normalized to $V = V_{\odot}$ at $R = 2h$. Figures 5.5a,b,c show plots of this rotation curve for various values of Q. Apart from a very steep rise in the central regions, the plots show a strongly decreasing rotation

Figure 5.4– The radial variation of the radial component of velocity dispersion predicted from SC's surface density function and rotation curve (circles). Also plotted is the run of σ_R predicted from the isothermal sheet model of van der Kruit & Searle (1981). The units are aribitrary.

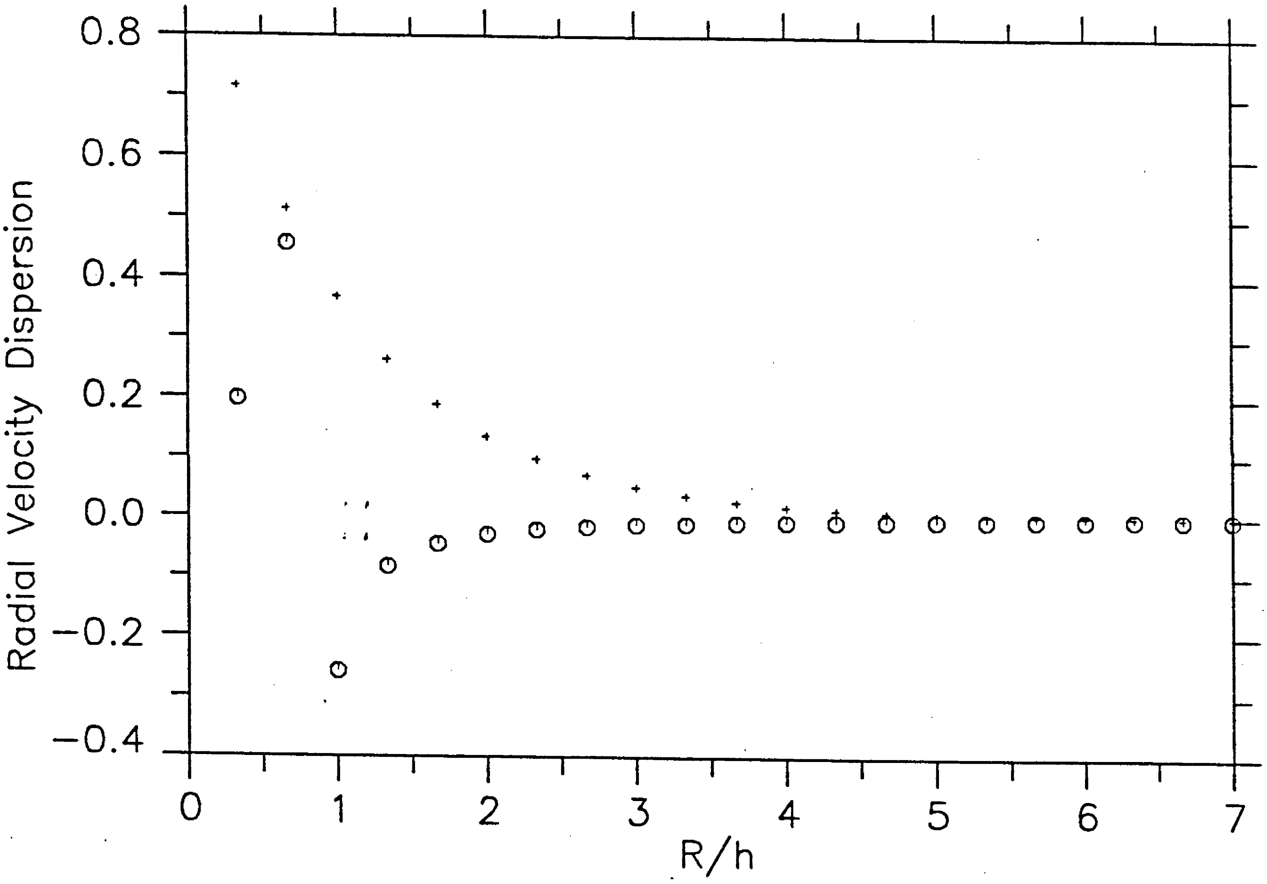
Radial Velocity Dispersion
R/h
0.8
0.6
0.4
0.2
0.0
−0.2
−0.4
0
1
2
3
4
5
6
7

Figures 5.5– Plots of the expected rotation curve for constant Q and our observed exponential run of $\sigma_R(R)$. (a) Q = 1.3, (b) Q = 1.5 and (c) Q = 1.65.

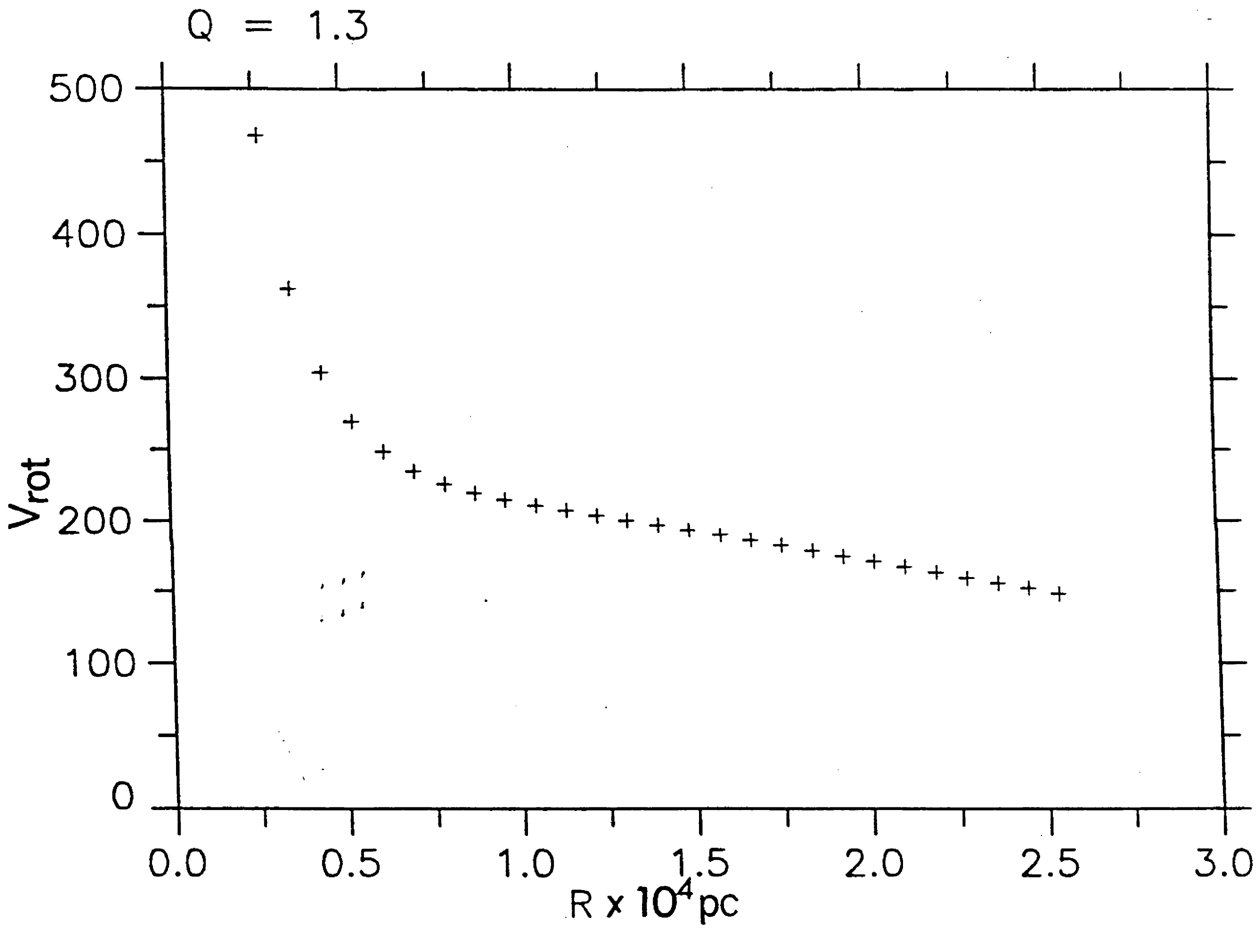
Q = 1.3
500
400
300
200
100
0
V_{rot}
0.0
0.5
1.0
1.5
2.0
2.5
3.0
R x 10^4 pc

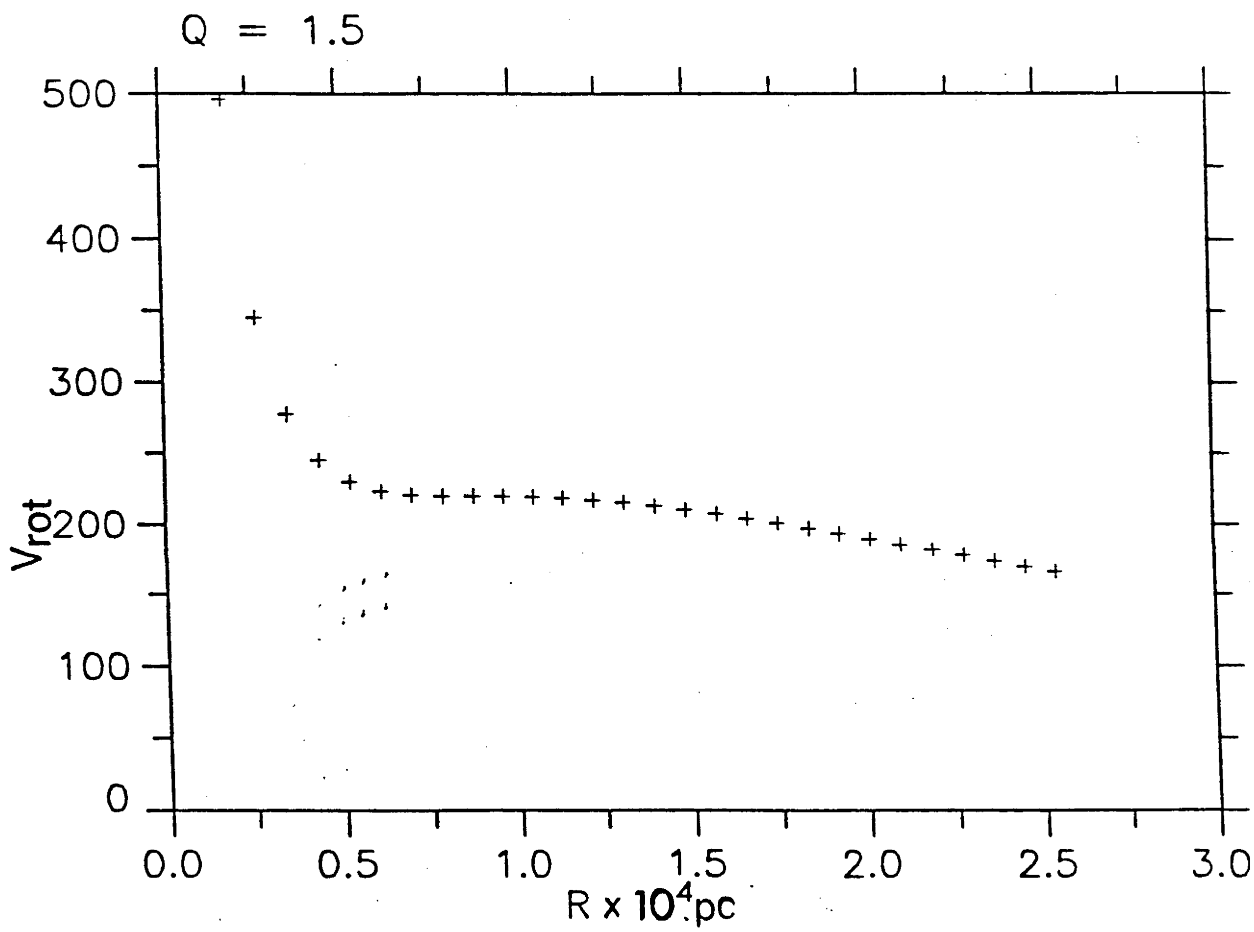

Q = 1.5
500
400
300
200
100
0
Vrot
0.0
0.5
1.0
1.5
2.0
2.5
3.0
R x 10⁴pc

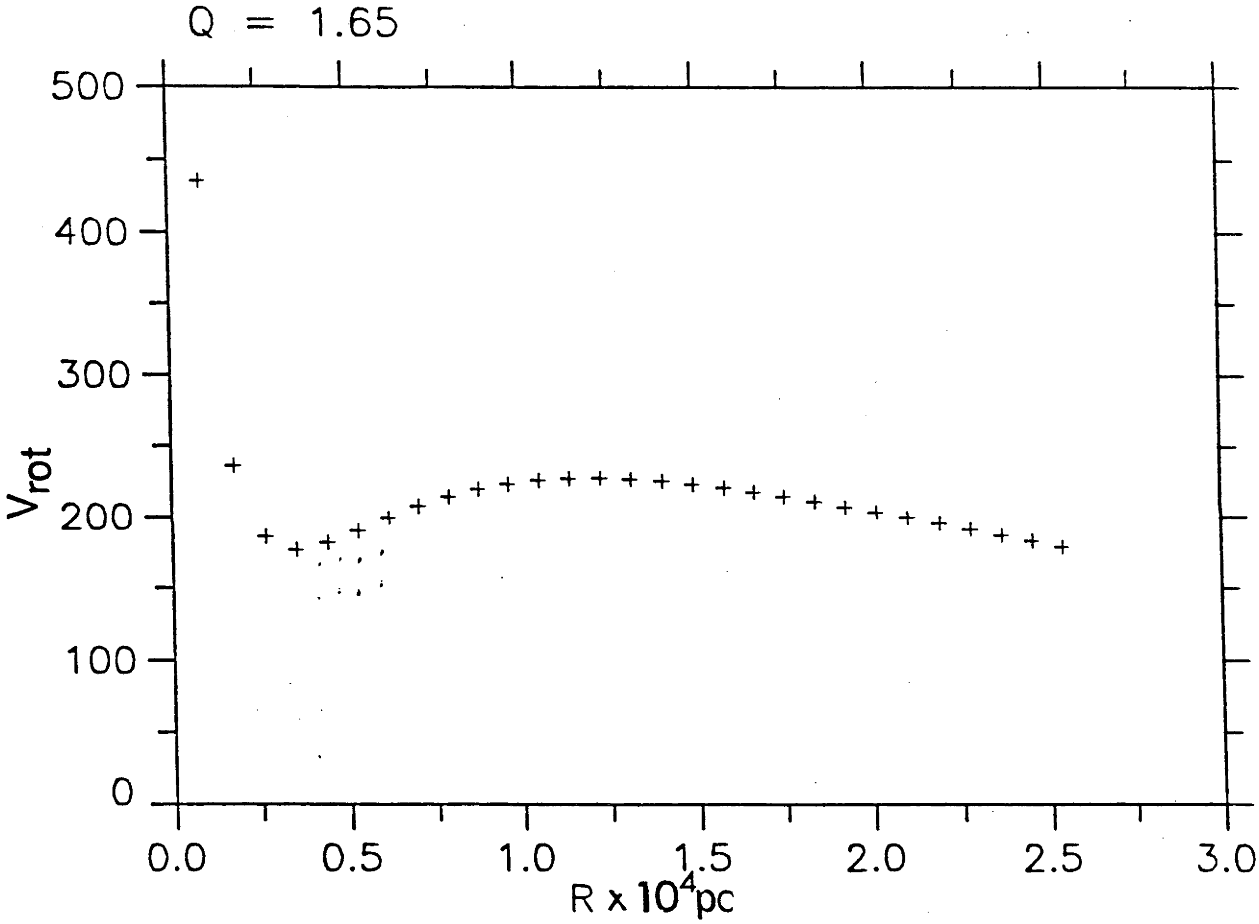
Q = 1.65
500
400
300
200
100
0
V_{rot}
0.0
0.5
1.0
1.5
2.0
2.5
3.0
R x 10^4pc

curve in the outer parts. This is quite contrary to observations which show the galactic rotation curve to be flat out to very large distances, at least 5 scale-lengths (Blitz–discussion at NATO ASI on the Galaxy 1986 in press.)

5.4 The Origin of the Hot Disk

Now that we know that the disk is indeed quite hot near the center, we need to identify the mechanisms that heated the disk. Spitzer and Schwarzschild (1951,1953) suggested that collisions between massive cold clouds and stars could account for the relationship seen between stellar ages and vertical velocity dispersion. Lacey (1984) has extended this concept to all three galactic coordinates. However his calculations were unable to reproduce the ratio $\sigma_R : \sigma_\varphi : \sigma_z$ for the solar neighborhood satisfactorily: too much energy was transferred to the z direction. Thus it seems that massive cloud collisions alone cannot reproduce the kinematics we see in the R, φ components in the galactic disk today.

Although their models did not produce the observed dependence of Q on R, the mechanism proposed by SC seems to account for the age-velocity dispersion relation in the solar neighborhood, and hence its effect in the plane is interesting. SC found that, if there was no cooling of the disk, the random motions due to the encounters with the recurrent transient spiral structure rose so quickly that the models soon became stable to the spirals themselves, and no more heating could take place. The effect of a certain amount of infall from the halo was to increase the surface density, decrease the velocity dispersion of a given sample and hence lower the value of Q. This allowed the spiral structure to continue. They found, however, that as the halo lost more and more mass, it lost its ability to stabilize the disk against global bar modes. They also found that the size and strength of the bar depended critically on the rate of accretion from the halo. They suggest that, by adjusting accretion to just the right amount, the spiral structure could be maintained and the bar mode would still be supressed.

However a transient central bar could also act as an accelerating mechanism. Heating by the bar in the central parts followed by the gradual dissolution of the bar could cause σ_R to rise in the way that we see in our data. It would have been interesting to know whether this mechanism would have worked, had SC been able to run some of their models for longer. Their 'standard' model ran for 13.5 rotations (at $2h$) when a strong bar became apparent, compared with the likely age of the old disk of the Milky Way of about 20-30 rotations at $2h$. Longer runs may give some insight into the heating effect of central bars in the central regions of the galactic disk.

Toomre (1986) has suggested an alternative view: that the strong rise in the velocity dispersion towards the center of the galaxy could be a product of mergers in the early lifetime of the galaxy. The idea is that after cloud fragmentation and collapse, the new proto-disk may have swept up large amounts of excess material. The resulting collisions with the merging material would have caused a rapid increase in the velocity dispersion in the disk. Thus early on, the central parts of the disk would have been a location of quite rapid dynamical evolution. This hypothesis awaits detailed modelling to see if it would work.

5.5 The Ratio of $\sigma_\varphi^2/\sigma_R^2$

From the epicyclic approximation, there is also a relation which connects the ratio of velocity dispersions in the plane of the disk to its rotation curve, i.e.

$$\frac{\sigma_\varphi^2}{\sigma_R^2} = \frac{-B}{A-B} \tag{5.11}$$

If we use the functional form of the runs of velocity dispersion which we described in Chapter 4 then:

$$1 + \frac{R}{V}\frac{dV}{dR} = \frac{2\sigma_{\varphi 0}^2}{\sigma_{R0}^2} e^{-R(\frac{1}{h_\varphi} - \frac{1}{h_R})} \tag{5.12}$$

If the rotation curve is flat, i.e. $dV/dR = 0$ then the left hand side of equation (5.12) is constant. Hence to make the right hand side also constant the two scale-lengths must be equal. This leaves the ratio:

$$\frac{\sigma_\varphi^2}{\sigma_R^2} = 1/2 \tag{5.13}$$

which is close to what is seen in the solar neighborhood. We have observed that $h_\varphi < h_R$. This suggests that the rotation curve is not precisely flat. Equation (5.12) can be integrated to give an independent estimate of the rotation curve from σ_R and σ_φ. If we let $x = R(1/h_\varphi - 1/h_R)$ then:

$$\ln V = \int \left(\beta^2 \frac{e^{-x}}{x} - \frac{1}{x}\right) dx \tag{5.14}$$

where $\beta^2 = 2\sigma_\varphi^2/\sigma_R^2$. This has the solution:

$$\ln V = \sum_{n=1}^{\infty} \frac{(-x)^n}{n \cdot n!} + (\beta^2 - 1)\ln x + K \tag{5.15}$$

where K is a constant of integration which is fixed by letting $\ln V = \ln V_\odot$ at $R = R_o$. Figure 5.6 is a plot of the rotation curve predicted from equation (5.15). We see that the rotation curve derived from this somewhat indirect procedure is remarkably close to the Burton & Gordon (1978) rotation curve, which is also included on this plot. This figure shows that the difference in the radial and tangential scale-lengths is consistent qualitatively with the curvature of the rotation curve in the inner regions.

5.6 Metallicity in the Old Disk

The run of $[Fe/H]$ with distance (Figure 4.8) shows that the radial gradient of metallicity which appears to exist in young and intermediate age objects (see Janes 1979) does not appear in our old disk stars. It may

Figure 5.6– The rotation curve expected from the measured runs of the radial and tangential components of velocity dispersion (crosses). Also plotted is the Burton & Gordon (1978) CO rotation curve (solid line).

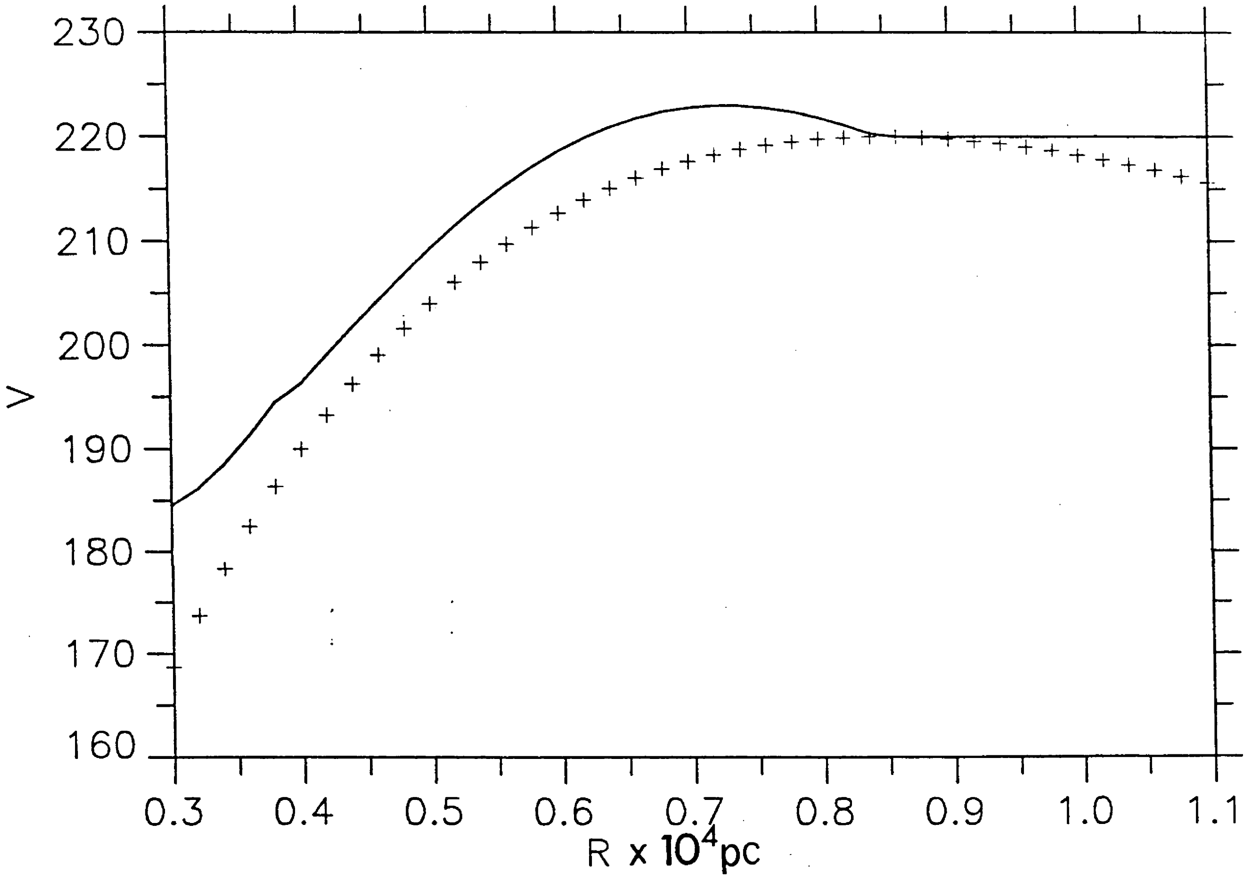

230
220
210
200
190
180
170
160
V
0.3
0.4
0.5
0.6
0.7
0.8
0.9
1.0
1.1
R x 10⁴pc

be that this behavior can be explained in terms of a simple model of star formation rates by Dopita (1985,1986). For this model, he has argued that the metallicity of a star is determined by the gas fraction in the place of its birth. The gas fraction also determines the star formation rate. If one then assumes that star formation proceeds radially from the center of the disk with time (e.g. Larson 1976), then the peak in the star formation rate occurs at at later times in the outer regions than in the inner regions. However, the star formation rate has the same functional dependence on gas fraction throughout the disk. Therefore all the old stars formed in an environment with similar mean gas fraction, and thus they have the same abundance, independent of galactocentric radius. (The old stars near the center are then somewhat older than the old stars in the outer parts). At present the gas fraction is low near the center and high in the outer parts. Therefore the young objects near the center are metal rich while the objects in the outer parts are metal poor. This is, however, only a qualitative argument and it also awaits a detailed model to determine its plausibility.

In a recently completed study, Rich (1986) has measured abundances for approximately 100 stars in Baade's Window. His results indicate that a significant fraction ($\approx 40\%$) of the stars in this region are 'super metal rich', i.e. $[Fe/H] > 0$. In this thesis, we have found very few stars in our sample to be super metal rich. In order to compare these results, we looked at the color-magnitude relation of our innermost bin. In that bin all of our stars were in the ranges $1.7 < (B-V) < 2.0$ and $14.5 < V < 16.0$. Of the 39 stars in Rich's sample with $[Fe/H] > 0.3$ only four of them were in the color and magnitude ranges of our sample. Hence the two samples are not directly comparable. His stars were mostly fainter than ours. This indicates that his stars are somewhat more distant than ours and that he may have selected true central bulge stars, while ours are disk members.

CHAPTER SIX

Conclusions and Suggestions for Future Work

6.1 Conclusions

From the preceding chapters, there are several conclusions we can make about the kinematics and chemical properties of the old disk of the Milky Way.

(1) The radial scale-length of the disk (as defined by the exponential decrease of the surface density with radius) can be determined from the exponential run of the radial component of the velocity dispersion in the old disk, if we assume that the anisotropy σ_R/σ_z is constant throughout the disk. The value of this kinematically determined scale-length is 4370 pc, which is consistent with the scale-length derived from photometry and star counts. This consistency supports the assumption of uniform anisotropy.

(2) From our measured run of σ_R we conclude that Toomre's stability parameter Q rises to about 2.5 at about half a disk scale-length from the galactic center. The value of Q is everywhere ≥ 1.3; Q also rises slowly outside the solar circle. The fact that Q is never less than 1 is reassuring, as a disk cannot be dynamically stable to local axisymmetric modes if the random motions are so low. This gives us confidence that our measured values of Q are indeed realistic.

The fact that Q rises to such high levels in the inner parts is important as this probably provides the disk with the pressure it needs to stabilize itself against global bi-symmetric modes, as suggested by the work of Athanassoula and Sellwood (1986).

(3) The two exponential scale-lengths which were found from the runs of σ_φ and σ_R were not the same, which is what one would expect if the

rotation curve were not flat everywhere. Given the exponential variations of both σ_R and σ_φ, we can solve for the rotation curve analytically, because the radial variation of the ratio σ_R/σ_φ is related to the rotation curve. The resulting curve matches the Burton & Gordon (1978) CO rotation curve curve well over the region 3 kpc to 10 kpc.

(4) The radial gradient of metallicity, which has been observed for both young and intermediate age objects, is not present in the old disk of the Milky Way. This may be indicative of a star formation history in which star formation proceeds radially from the center as a function of time, with the star formation rate and the metallicity depending on the local gas fraction.

6.2 Plans for Future Work

6.2.1 The origin of the Galactic Anisotropy

Now that we know how hot the disk is, we are confronted with the question of how the disk acquired so much random motion. As was previously mentioned, the work of SC has yielded some interesting results on the growth of random motions in the planes of galactic disks. Models based on the Spitzer & Schwarzschild (1951,1953) mechanism are successful in reproducing the age-velocity dispersion relation vertical to the plane in the solar neighborhood. The question we wish to ask is whether these two mechanisms are coupled together to give the amplitude of the random motions and the velocity dispersion anisotropy which we see in the galactic disk today.

For example, the transient spiral structure model of SC could act as a heating mechanism in the plane of the disk. Then scattering by clouds may convert some of the star's plane energy into energy in z. A simple scattering model would show us whether the observed anisotropy could be reproduced in this way.

6.2.2 The Truncation of Galactic Disks

Another interesting question of galactic astronomy concerns the truncation of galactic disks. In their models of the three dimensional distribution of light in spiral galaxies, van der Kruit & Searle (1981) could fit an exponential disk function to the radial variation of light in edge-on galaxies only after a sharp cutoff at some large galactic distance (typically 4 to 5 scale-lengths) was imposed on the models. They suggest that these cutoffs are in fact real aspects of galactic structure rather than an artifact of the data, and they give a number of reasons for why these cutoffs may exist. One such suggestion is that there may be a critical density threshold, below which no star formation can occur. Another suggestion is a scenario where disk formation is slow and the cutoff is simply the distance out to which star formation has progressed at present (cf section 5.6).

It is possible to test this picture in the Milky Way. The idea is to look at a sample of red stars in an anticenter direction. Modelling the distribution of giants and dwarfs in the region for various values of R_{max}, say $4h$, $5h$ and ∞, would give us an idea of what percentage of these stars we would expect to be giants. We then take spectra of these stars. If the cutoff does exist, it will manifest itself as an apparent detriment of the distant red giants relative to foreground red dwarfs in the sample. Our model predictions should then be able to tell us whether a cutoff exists and if so, where it is.

It would be an obvious advantage to use the same luminosity classification strategy here as we did in this thesis. If we restrict our selection criteria so that all the giants will be K stars and all the dwarfs will be M stars, then the sometimes painful process of luminosity classification can be made easier. This obviously depends on the choice of region and the run of reddening.

At the time of this writing, we have been granted a night on the AAT to do this project using the fiber system in December 1986. With the ability to observe about 45 objects at a time, we should be able to answer the question of truncation of galactic disks with just one night of good observations.

APPENDIX I

Distance Errors

An estimate of the errors in the calculated distances is a fairly straight forward procedure. The major contributing factor to distance errors were:

- Color Errors
    1. Photometric errors $\sigma_{(B-V)}$
    2. Reddening estimate errors $\sigma_{E(B-V)}$
- Metallicity
    1. [Fe/H] estimate errors $\sigma_{[Fe/H]}$
- Magnitude errors
    1. Photometric errors σ_V

To estimate the contribution from all of these, it is necessary to go back to the observable quantities, as some of these errors will be correlated, e.g. $\sigma_{[Fe/H]}$ and $\sigma_{(B-V)}$ (see Chapter 3). Our estimate of reddening will be correlated with the distance error itself, as the reddening was calculated as a function of distance. However the random errors in reddening are much larger than the errors in reddening that come from the distance estimate, as most of the stars we looked at were well out of the absorbing layer as shown by equations (2.1) and (2.2). Start with:

$$(B-V)_o = (B-V) - E(B-V) \tag{A1.1}$$

by definition. Next let

$$\left[\frac{Fe}{H}\right] = \alpha(B-V)_o + \beta \log \Sigma W_\lambda + \gamma \tag{A1.2}$$

where $\log \Sigma W_\lambda$ is the metallicity line strength indicator which are defined in Chapter 3. α, β and γ are all defined for the metallicity standards in Chapter 3. Finally let

$$M_v = \delta(B-V)_o + \epsilon\left[\frac{Fe}{H}\right] + \theta \tag{A1.3}$$

over a small region of $(B-V)_o$ and $[Fe/H]$. Then

$$\begin{aligned} M_v &= \delta\left[(B-V) - E(B-V)\right] + \\ &\quad \epsilon\left\{\alpha\left[(B-V) - E(B-V)\right] + \beta\log\Sigma W_\lambda + \gamma\right\} + \theta \end{aligned} \tag{A1.4}$$

or

$$\begin{aligned} M_v - 3E(B-V) &= (\delta+\epsilon\alpha)(B-V) - (\delta+\epsilon\alpha+3)E(B-V) + \\ &\quad \epsilon\beta\log\Sigma W_\lambda + \epsilon\gamma + \theta \end{aligned} \tag{A1.5}$$

If we treat $\alpha, \beta, \delta, \gamma, \epsilon, \theta$ as known constants then:

$$\sigma^2_{M_v+3E(B-V)} = (\delta+\epsilon\alpha)^2\sigma^2_{(B-V)} + (\delta+\epsilon\alpha+3)^2\sigma^2_{E(B-V)} + \epsilon^2\beta^2\sigma^2_{\log\Sigma W_\lambda} \tag{A1.6}$$

where $\sigma_{(B-V)}$ is only a result of photometric errors. The distance errors were calculated from the standard formula

$$\sigma^2_{\log d} = 0.2(\sigma^2_V + \sigma^2_{M_v+3E(B-V)}) \tag{A1.7}$$

From Chapter 3 the error in $[Fe/H]$ is approximately 0.2 dex from the standards. As the colors and reddenings of the standards are fairly well known, this error can be attributed solely to the $\log\Sigma W_\lambda$ term, i.e.

$$0.2 \approx \beta\sigma_{\log\Sigma W_\lambda} \tag{A1.8}$$

where $\beta = 3.98$. Thus $\sigma^2_{\log\Sigma W_\lambda} = 2.5\times10^{-3}$. Table A1.1 shows the percentage error expected for various values of $\sigma_{E(B-V)}$, σ_V and $\sigma_{(B-V)}$. These are all plausible error estimates for our data. A quick glance shows that the errors are not very sensitive to changes in $\sigma_{E(B-V)}$. From this table an estimate of about 15% in distance from the sun seems to be realistic for our data.

The values of α, β and γ were the same, by definition, as the values of C_1, C_2 and C_0 respectively, which were given in section 3.9. The values of δ, ϵ and θ depend on the region of V, $(B-V)_o$ and $[Fe/H]$ begin considered, as the relation in equation (A1.3) will only hold over a small region in V, $(B-V)_o$ and $[Fe/H]$. For $V=15$, $(B-V)_o=1.4$ and $[Fe/H]=-0.3$ the values of δ and γ were -3.19 and 0.28 respectively. The value of θ does not enter into equation (A1.6) and hence can be ignored.

Table A1.1 Calculation of Distance Errors

V	$(B-V)_o$	[Fe/H]	E(B-V)	$\sigma_{(B-V)}$	$\sigma_{E(B-V)}$	σ_V	% error
15.0	1.4	-0.3	0.5	0.07	0.1	0.05	12
15.0	1.4	-0.3	0.5	0.10	0.1	0.07	17
15.0	1.4	-0.3	0.5	0.07	0.2	0.05	13
15.0	1.4	-0.3	0.5	0.10	0.2	0.07	18
15.0	1.4	-0.3	0.4	0.07	0.1	0.05	12
15.0	1.4	-0.3	0.6	0.07	0.1	0.05	12
15.0	1.4	-0.8	0.5	0.07	0.1	0.05	16
15.0	1.5	-0.3	0.5	0.07	0.1	0.05	10
15.0	1.3	-0.3	0.5	0.07	0.1	0.05	14
14.0	1.4	-0.3	0.5	0.07	0.1	0.05	12
16.0	1.4	-0.3	0.5	0.07	0.1	0.05	12

Bibliography

Albada, T.S van, Bahcall, J.N., Begeman, K., and Sanscisi, R., 1985, *Ap. J*, **295**, 305.

Aller, L.H., 1942, *Ap. J.*, **95**, 52.

Arp, H., and Cuffey, J., 1962, *Ap. J.*, **136**, 52.

Athanassoula, E., and Sellwood, J.A., 1986, in press.

Bahcall, J.N., 1984, *Ap. J.* **276**, 169.

Bahcall, J.N., and Soneira, R.M. 1980, *Ap. J. Suppl.*, **44**, 73.

Bahcall, J.N., and Soneira, R.M. 1984, *Ap. J. Suppl.*, **55**, 67.

Becker, W., 1960, *Zeitschrift für Astrophysik*, **51**, 49.

Bergh, S. van den, 1971, *A. J.*, **76**, 1082.

Berman, R.H., and Mark, J.W.-K., 1979, *Astron. & Ap.*, **77**, 31.

Bevington, P.R., 1969, *Data Reduction and Error Analysis for the Physical Sciences*, (New York: McGraw-Hill), p.127.

Blitz, L., 1986, discussion at NATO ASI on *The Galaxy*, in preparation.

Burton, W.B., and Gordon, M.A., 1978, *Astron. & Ap.*, **63**, 7.

Camm, G.L., 1950, *M. N. R. A. S.* , **110**, 305.

Carignan, C., 1983, Thesis, Australian National University.

Carlberg, R.G., and Sellwood, J.A., 1985 *Ap. J.*, **292**, 79.

Carlberg, R.G., Dawson, P.C., Hsu, T., and VandenBerg, D.A., 1985, *Ap. J.*, **294**, 674.

Chun, M.S., and Freeman, K.C., 1978, *Ap. J.*, **83**, 376.

Delhaye, J., 1965, in *Galactic Structure*, ed A. Blaauw and M. Schmidt (Chicago: University of Chicago Press), p. 61.

Dopita, M.A., 1985, *Ap. J. Lett.*, **295**, L5.

Dopita, M.A., 1986, in *Nearly Normal Galaxies* ed. S. Faber (in preparation).

Efstathiou, G., Lake, G., and Negroponte, J., 1982, *M. N. R. A. S.*, **199**, 1069.

Eggen, O.J., and Sandage, A., 1964, *Ap. J.*, **140**, 130.

Eggen, O.J., and Sandage, A., 1969, *Ap. J.*, **158**, 685.

Freeman, K.C., 1970, *Ap. J.*, **160**, 811.

Freeman, K.C., 1978, IAU symp. **77**, *Structure and Properties of Nearby Galaxies*, eds. E.M Berkhuijsen and R. Wielebinski, Reidel, Dordrecht, p. 3.

Freeman, K.C., Karlsson, B., Lyngå, G., Burrell, J.F., Woerden, H. van, Goss, W.M., and Mebold, U., 1977, *Astron. & Ap.*, **55**, 445.

Gilmore, G., and Reid, I.N., 1983, *M. N. R. A. S.*, **202**, 1025.

Harris, W.E., 1982, *Ap. J.*, **50**, 573.

Hartkopf, W.I., and Yoss, K.M., 1982, *A. J.*, **87**, 1679.

Hartwick, F., and Hesser, J., 1973, *Ap. J.*, **183**, 883.

Hohl, F., 1971, *Ap. J.*, **168**, 343.

Janes, K.A., 1975, *Ap. J. Suppl.*, **29**, 161.

Janes, K.A., 1979, *Ap. J. Suppl.*, **39**, 135.

Kalnajs, A.J., 1972, *Ap. J.*, **175**, 63.

Kormendy, J., 1984a, *Ap. J.*, **286**, 116.

Kormendy, J., 1984b, *Ap. J.*, **286**, 132.

Kruit, P.C. van der, 1986, *Astron. & Ap.*, **157**, 230.

Kruit, P.C. van der, and Freeman, K.C., 1984, *Ap. J.*, **278**, 81.

Kruit, P.C. van der, and Freeman, K.C., 1986, *Ap. J.*, **303**, 556.

Kruit, P.C. van der, and Searle, L., 1981, *Astron. & Ap.*, **95**, 105.

Kruit, P.C. van der, and Searle, L., 1982, *Astron. & Ap.*, **110**, 61.

Lacey, C.G., 1984, *M. N. R. A. S.*, **208**, 687.

Lacey, C.G., and Fall, S.M., 1983, *M. N. R. A. S.*, **204**, 791.

Larson, R.B., 1976, *M. N. R. A. S.*, **176**, 31.

Lynden-Bell, D., and Kalnajs, A.J., 1972, *M. N. R. A. S.*, **157**, 1.

McClure, R.D., 1976, *A. J.*, **81**, 182.

McClure, R.D., and Bergh, S. van den, 1968, *A. J.*, **73**, 313.

Menzies, J., 1973, *M. N. R. A. S.*, **163**, 323.

Menzies, J., 1974, *M. N. R. A. S.*, **169**, 79.

Miller, R.H., 1978, *Ap. J.*, **223**, 811.

Miller, R.H., Prendergast, K.H., and Quirk, W.J., 1970, *Ap.J.*, **161**, 903.

Morgan, J.G., and Eggleton, P.P., 1978, *M. N. R. A. S.*, **182**, 219.

Newell, E.B., 1979, in *Image Processing in Astronomy*, ed G. Sedmak, M. Capaccioli, and R.J. Allen, Observitorio Astronomico di Trieste, 100.

Oort, J.H., 1965, in *Galactic Structure*, ed A. Blaauw and M. Schmidt (Chicago: University of Chicago Press), p. 455.

Oort, J.H., 1960, *Bull. Astr. Inst. Neth.*, **15**, 45.

Ostriker, J.P., and Peebles, P.J.E., 1983, *Ap. J.*, **186**, 467.

Pritchet, C., 1983, *A. J.*, **88**, 1476.

Ratnatunga, K., and Freeman, K.C., 1985, *Ap. J.*, **291**, 260.

Rich, R.M., 1986, Thesis, Cal. Inst. Tech.

Sandage, A., 1970, *Ap. J.*, **162**, 863.

Sandage, A., 1982, *Ap. J.*, **252**, 553.

Sandage, A., 1986, preprint.

Sandage, A., and Smith, L.L., 1966, *Ap. J.*, **144**, 886.

Sellwood, J.A., 1981, *Astron. & Ap.*, **362**, 362.

Sellwood, J.A., and Carlberg, R.G. (SC), 1984, *Ap. J.*, **282**, 61.

Searle, L., 1971, *Ap. J.*, **168**, 327.

Simkin, S.J., 1974, *Astron. & Ap.*, **31**, 129.

Smith, G.H., and Norris, J.E., 1982, *Ap. J.*, **254**, 149.

Spitzer, L., 1942, *Ap. J.*, **95**, 329.

Spitzer, L., and Schwarzschild, M., 1951, *Ap. J.*, **114**, 385.

Spitzer, L., and Schwarzschild, M., 1953, *Ap. J.*, **118**, 106.

Stapinski, T.E., Rodgers, A.W., and Ellis, M.J., 1981, *P.A.S.P*, **93**, 242.

Stetson, P.B., and Harris, W.E., (1977), *A. J.*, **82**, 954.

Tonry, J., and Davis, M., (1979), *A. J.*, **84**, 1511.

Toomre, A., 1986, Private Communication.

Toomre, A., 1964, *Ap. J.*, **139**, 1217.

Tsikoudi, V. 1977, Thesis, University of Texas.

Vaucouleurs, G. de, 1959, *Handbuch der Physik*, **53**, 311.

Vaucouleurs, G. de, and Pence, W.D., 1978, *A. J.*, **83**, 1163.

Wainscoat, R.J., 1986, Thesis, Australian National University.

Wallerstein, G., 1962, *A. J.*, **67**, 329.

Whitford, A.E., and Rich, R.M., 1983, *Ap. J*, **274**, 723.

Wielen, R., 1974, *P. A. S. P.* , **86**, 341.

Wielen, R., 1977, *Astron. & Ap.*, **60**, 263.

Wilson, G.A., 1986, Thesis, Australian National University (in preparation).

Woolley, R., 1965, in *Galactic Structure*, ed A. Blaauw and M. Schmidt (Chicago: University of Chicago Press), p. 85.

Yoss, K., and Neese, C., 1986, Private Communication.

Zang, T.A., 1976, Thesis, Mass. Inst. Tech.